

## ABSTRACT

LU, SHIJING. Computational Study of Grain Boundaries and Nano-Reactive Materials.  
(Under the direction of Professor Donald Brenner.)

The thesis summarized my research efforts in two areas:

Chapters 1 to 4 devote to the computational study of grain boundary (GB) structure, energy and mobilities. Despite of the considerable effort that has been placed on those topics, computational study of GB is still a daunting task. Chapter 1 gives a small glimpse into the rich world of GB studies in the past and the difficulties they met. In chapter 2, we propose a new approach to predicting and organizing interface structures in alloys that takes advantage of a disclination structural units model developed previously for grain boundaries in pure systems. This method is demonstrated using symmetric tilt GB in multiple alloy systems. Chapter 3 studies the GB migration using molecular dynamics simulation (MDS) with two methods: (i) direct simulation of GB motion under synthetic driving force. (ii) Transition path sampling (TPS) method. The two methods predict GB mobility differently. But they are consistent with each other because two GB migration mechanisms present in the first approach but only one mechanism is modeled in the TPS method. A simple and clear way to separate two GB migration mechanisms during the direct simulation is also reported in the chapter 3. Of the two GB migration mechanism, the shear coupled mechanisms has been well studied. In chapter 4, the spotlight is focused on the other GB migration mechanism: GB sliding. Two methods are reported, one uses MDS with nudged elastic band techniques and the other is based on macro-scale linear elasticity theory.

Chapters 5 to 8 summarize the computational study of nano energetic materials (NEMs), or more specifically, nano thermites and nano reactive intermetallic compounds. NEMs have raised substantial scientific and technological interest in recent years for their

high reactivity, high energy density, low cost, and non-toxic nature. Chapter 4 provides an overview and information useful for synthesis and characterizations of NEMs. Special concern is given to the thermo analysis (TA) methods of NEMs. Compare to the self-sustaining reaction in NEMs, reactions in TA methods such as differential thermal analysis (DTA) or differential scanning calorimetry (DSC) are much slower. This makes TA a good candidate to unveil the coupled non-equilibrium processes during reactions. However, conventional TA requires a prior knowledge of “model functions” which are empirical approximations (for example, the 1<sup>st</sup> order reaction) of the overall reactions. In chapter 7, we proposed a better analysis method to study DSC traces of NEMs. This analysis is able to: i) reproduce the DSC curves; ii) predict the peak temperature positions as a function of system sizes and DSC heating rates; iii) explore micro-mechanisms during controlled reactions and provide clean way of retrieving diffusivity parameters. Tested with several experimental datasets and numerical simulations, the new analysis method shows significant improvement over the conventional TA methods. Further, the new TA method predicts that nano energetic particles may work better than nano ferro oxide particles do in hyperthermia cancer treatment (HCT) because of NEMs’ capability of releasing heat rapidly. Chapter 8 reviews the past researches of using nano particles in the HCT. In conventional HCT, energy is transferred to cancer cells through alternating magnetic field (AMF). In chapter 8, a nano pillar comprising both ferro oxides and NEMs is proposed. Upon taken the nano pillars will accumulate in cancer cells due to the well-known Enhanced Permeability and Retention (EPR) effect. Ferro oxides can first be heated up through AMF, and then they will initiate the reactions in NEMs which then will kill the cancer cell. Based on our calculation, this design is promising.

© Copyright 2015 Shijing Lu

All Rights Reserved

Computational Study of Grain Boundaries and Nano-Reactive Materials

by  
Shijing Lu

A dissertation submitted to the Graduate Faculty of  
North Carolina State University  
in partial fulfillment of the  
requirements for the degree of  
Doctor of Philosophy

Materials Science and Engineering

Raleigh, North Carolina

2015

APPROVED BY:

---

Prof. Donald W. Brenner  
(Chair of Advisory Committee)

---

Prof. Douglas Irving

---

Prof. Carl C. Koch

---

Prof. Korukonda L. Murty

## **BIOGRAPHY**

Shijing Lu was born in a small town in the eastern part of China in 1986. At his very young age, he was told to choose from two possible futures: be a good student and go to college or be a punk and become homeless. Had been profoundly influenced by Robinson Crusoe, he strongly favored the latter option. Unfortunately, being too puny, he had never had a chance to be accepted by other punks. He was recommended for admission to the Chu Konchen Honors College Zhejiang University in 2003 for winning the first class prize in Chemistry Olympic. From there, he earned B. S. in the General Science Major in 2007. After several years as research assistant in Zhejiang Institute of Modern Physics (2007 – 2009) and in Asia Pacific Center of Theoretical Physics (2009 – 2010), he decided to pursue graduate studies at North Carolina State University where finally decided to solve problems by fingers instead of fists.

## ACKNOWLEDGMENTS

This thesis is the culmination of 5 years of research. I would like to take this opportunity to thank those who made it possible

First and foremost, I would like to express my deepest gratitude to my advisor and committee chair Prof. Brenner for his continuous support and guidance throughout my doctoral program. He is not only a prominent scholar in this field, but also a kind and forbearing mentor. He kindly helped my wife to apply for the admission to N. C. State so that we can live together after being separate for six years.

I would like to thank Prof. Irving, Prof. Maria and Dr. Mily for their contribution to this research. I owe a special note of thanks to Prof. Irving for his many times generous help from time to time. I would also like to express my gratitude to Prof. Koch and Prof. Murty for serving on my thesis committee. Their comments and suggestions were of inestimable value for my research and study.

Thanks are due to my parents and my sister for their understanding and support all these years. I want to thank my wife, Yiying Zhu, for always believing in me and cheering me on.

Finally, I sincerely acknowledge Naval Research Office and Army Research Office for grants that made it possible to complete my PhD study.

## TABLE OF CONTENTS

LIST OF TABLES .....	vi
LIST OF FIGURES .....	vii
PART 1, GRAIN BOUNDARY .....	1
<b>Chapter 1 An Overview of the Computational Study of the Grain Boundary Structure , Energy and Mobility.....</b>	<b>1</b>
1.1 Introduction.....	1
1.2 Molecular Dynamics and Interatomic Potentials.....	3
1.3 Basic Conceptions of Grain Boundaries .....	5
1.4 Coarse Grained Representation of Equilibrium Grain Boundaries .....	11
1.5 Approaches to Compute Grain Boundary Mobilities.....	16
1.6 Overview of Chapters 2 – 4.....	21
<b>Chapter 2 Solute Segregation Energy and Grain Boundary Energy Calculation Based On Disclination Structural Units Model and Perturbation Methods .....</b>	<b>24</b>
2.1 Introduction.....	24
2.2 Theory .....	26
2.3 Experiment .....	32
2.4 Results and Discussion.....	35
2.5 Conclusion .....	39
<b>Chapter 3 Studying Motion of <math>\langle 100 \rangle</math> Tilt Grain Boundaries Using Molecular Dynamics Simulation .....</b>	<b>44</b>
3.1 Introduction.....	44
3.2 Direct MDS with Pure Metal Systems .....	47
3.3 Mobility Calculation with Transition Path Sampling Method.....	49
3.4 Results .....	52
3.4.1 Direct MDS with Driving Force.....	52
3.4.1 Transition Path Sample Calculations .....	58
3.5 Conclusion .....	61
<b>Chapter 4 Micromechanics of Grain Boundary Shearing from Atomic Modeling ....</b>	<b>63</b>
4.1 Introduction.....	63
4.2 Simulation .....	65
4.3 Results and discussion .....	69

<b>Part 2, Nano reactive material</b> .....	73
<b>Chapter 5 An Introduction to Nano Energetic Materials</b> .....	73
5.1 Nano metallic composites .....	73
5.2 Nano thermite composites .....	75
5.3 Characterization and modeling solid reaction for nano reactive materials .....	78
5.3.1 Modeling Self – Propagated Combustion .....	78
5.3.2 Modeling the thermal analysis curves.....	80
<b>Chapter 6 Interpretation of Differential Scanning Calorimetry Data of Energetic Nanostructures based on Diffusion-Controlled Kinetics</b> .....	88
6.1 Introduction and Background .....	88
6.2 Formulation .....	91
6.2.1 Analytical Derivation based on Diffusion Equations.....	93
6.2.2 Derivation based on the Isoconversion Assumption.....	95
6.2.3 Thermal Conduction Modeling .....	97
6.3 Model Applications and Validation.....	98
6.3.1 Nano-Laminate Zr – CuO and Al – CuO Thermite .....	98
6.3.2 Interpretation of Kinetics in a multi-layer Ni/Al Aluminide .....	106
6.3.3 Cylindrical and Spherical Systems.....	108
6.4 Conclusions.....	111
<b>Chapter 7 Simulation of Electric Ignited Self-Propagating Reaction in Nano Thermites based on Diffusion-Controlled Kinetics</b> .....	112
7.1 Introduction.....	112
7.2 Electric Ignition Experiments and Setups of Numerical Simulations.....	114
7.2.1: On interface parallel planes.....	115
7.2.2: Simulation along the Interface Perpendicular Plane .....	118
7.2.3: Parameterization of model-based DSC curves .....	121
7.3 Results and discussion .....	122
<b>Chapter 8 Proposal for using nano-reactive materials for hyperthermia cancer treatment</b> .....	129
8.1 Nano-material and cancer targeting .....	129
8.2 Nano material and magnetic hyperthermia treatment.....	131
8.3 Magnetic hyperthermia treatment & specific loss power .....	134
8.4 Hyperthermia treatment using nano energetic materials .....	135

## LIST OF TABLES

Table 2.1: $\langle 100 \rangle$ Symmetric tilt grain boundaries with impurities segregating at the first lowest energy sites; the term “alloy” means the solute induced system. The dash symbol “-“ in the <i>Structure</i> column is used to denote the site that connects two basic structural units and is substituted by impurity atoms. For instance, an B-C structure is equal to a combination of B+C- structure shown in Figure 2.1 (a).....	33
Table 2.2: Observed disclination dipole strengths of fully relaxed atomistic structures. ....	35
Table 5.1: Experimental measured parameters for typical metallic laminate composites.....	74
Table 5.2: A list of ignition temperature for metallic composite systems.....	75
Table 5.3: Recent advances in synthesizing nano-thermites using various technologies.....	77
Table 5.4: Frequently used model functions for solid state reactions .....	81
Table 6.1: Temperatures of the first DSC peaks measured for a Al/CuO and Zr/CuO nanolaminate..	99
Table 6.2: DSC peak temperatures as a function of heating rate and bilayer thickness for Ni – Al bimetallic multilayer system .....	105

## LIST OF FIGURES

Figure 1.1: Illustration of a pure tilt grain boundary (a) and a pure twist grain boundary (b). .....	7
Figure 1.2: Atomic configurations of symmetric tilt angle grain boundaries from low to high misorientation. The bottom angular lines show the half of the misorientation angle, i.e. $\theta/2$ . From left to right, $\theta/2$ values are $3.02^\circ$ , $6.04^\circ$ , $18.44^\circ$ , $23.20^\circ$ and $26.57^\circ$ respectively. ....	8
Figure 1.3: Dependence of symmetric tilt angle grain boundary energies on the misorientation angles. The dotted circles are computed from molecular dynamics simulation of FCC copper using EAM potential. The solid curve is computed from the Read Shockley formula.....	9
Figure 1.4: Illustration of a simple cubic $\Sigma 5$ CSL structure. ....	10
Figure 1.5: Demonstration of (a) disclination model and (b) dislocation model of a symmetric tilt angle grain boundary. ....	12
Figure 1.6: Illustration of the structural units model for a STGB. The three grain boundaries shown here are the same as the last three grain boundaries shown in Figure 1.2. Atoms that are not near the grain boundaries are hidden. ....	14
Figure 2.1: (a) Structural units model of FCC $\langle 100 \rangle$ - $\Sigma 73$ -830 grain boundary. Impurity atoms, which are represented by bigger yellow spheres, segregate on the first lowest energy sites. The blue and red spheres denote the copper atoms that lie on (002) and (001) planes respectively. Those structures whose head (tail) atom is replaced are marked as positive (negative) structure. (b) Illustration of theoretical (inside green shape) and actual (outside black shape) C structure. Two dislocations pile up at the bottom of C unit. (c) Illustration how disclination dipole strength affects the DSUM results, the red dot line is the grain boundary energy of Copper calculated from atomistic models. The blue rectangle line and the green triangle line are DSUM predictions with and without dipole strength modification respectively. ....	40
Figure 2.2: Dependence of energies of $\langle 100 \rangle$ symmetric tilt grain boundaries on the tilt angle for four systems. Respectively: (a) Pb doped Al; (b) Nb doped Cu; (c) Zr doped Zr and (d) Zr doped Cu systems. The rectangle lines are computed directly from atomistic models with EAM potential, the solid circle lines are obtained from DSUM model. The red and purple lines correspond to pure metal system, the blue and green lines represent grain boundary energy of solute induced systems. ....	41
Figure 2.3: Stabilization effects shown by (a) Energies of different bond types of four alloy systems; (b) energy change of substituting a copper atom for a zirconium atom at different sites in the	

$\Sigma 17-530$ grain boundary. (c/d) Dependence of grain boundary energy on area density of impurities in different alloy systems / with different tilt angles.....	42
Figure 2.4: Comparison between expansion obtained and full calculations of segregation energies for Cu-Zr alloy. Values denoted by triangles are obtained from Eq. (2-9) only, and the circles are computed under the approximation of Eq. (2-10). Data with circle are elevated by 0.1 eV intentionally so that two sets of data are distinguishable. ....	43
Figure 3.1: Demonstration of three stable states (A, B, C) during a simulation of grain boundary migration. State A is the initial state during the TPS calculation and the reaction coordinate is defined as the position of the grain boundary. ....	51
Figure 3.2: Tilt angle dependence of (a): Mobilities at 800K and (b): corresponding activation energies for STGBs of copper as listed in the Table 2.1. The dashed dots are the stationary GB energies as reported in Figure 2.2. ....	54
Figure 3.3: (a), initial and final position of atoms in $\Sigma 17-530$ STGB, (b) y-component of displacement profile of atoms in (a) along z-direction. ....	56
Figure 3.4: Demonstration of activation energies computed by fitting temperature dependent GB mobility to different equations. The symbols are ensemble averaged MDS results, dashed lines are the fits using Eq. (3-1) and solid lines are the fits according to Eq. (3-7) .....	57
Figure 3.5: Correlation function and its linear fit for the $\Sigma 17-530$ STGB at 600K. ....	59
Figure 3.6: Histogram plot of $\Sigma 17-530$ STGB being at different stable states at t=5000fs. ....	60
Figure 4.1: Illustration of atomistic model used in the simulation. ....	66
Figure 4.2: Energy profile along RC for $\Sigma 12-320$ with different systems sizes. ....	67
Figure 4.3: Geometry characteristics of grain boundary sliding. ....	70
Figure 4.4: Comparison between barrier heights from NEB calculations and activation energies from Arrhenius law .....	72
Figure 5.1: Illustration of idea 1-D diffusion model for laminate Al – CuO thermite composite .....	82
Figure 5.2: Demonstration of using a model fitting method to interpret DSC curves. The solid line with cycles is the normalized DSC curve as a function of temperature. The insert are the model fitting curves based on various model functions listed in Table 5.4. ....	84
Figure 5.3: Demonstration of using isoconversion method to analyze DSC curves with various heating rates. The temperatures at which certain degrees of reaction have proceeded were found as the cross points of solid curves and horizontal dashed lines. The insert shows the fitting of the Eq.(5-8). ....	87

Figure 6.1: Illustration of sample geometries considered. Left: Laminate, Center: Cylinder, Right: Sphere.....	92
Figure 6.2: Plots of the Zr/CuO data in Table 6.1. (A) Given as a Kissinger plot, <i>i.e.</i> Eq. (3-9). (B) Plotted via Eq.(6-5). Diamonds, squares, triangles, circles and ×'s correspond to 1-5 bilayers, respectively.....	100
Figure 6.3: Plots of the Al/CuO data in Table 6.1. (A) Given as a Kissinger plot, <i>i.e.</i> Eq.(3-9). (B) Plotted via Eq.(6-5). Diamonds, squares, triangles and circles correspond to 1-4 bilayers, respectively.....	101
Figure 6.4: Natural logarithm of diffusion coefficient as a function of the inverse of the temperatures times Boltzmann's constant. The thick solid line is the diffusion coefficient predicted from the plot in Figure 2B over the temperature range at which the peak temperatures were measured. The thinner solid lines and the open diamonds are experimental data for self-diffusion of oxygen in Zr <sup>[152]-[156]</sup> , dashed and dotted lines correspond to experimental data for oxygen self-diffusion ZrO <sub>2</sub> and in CuO, respectively <sup>[157]-[160]</sup> . The line lengths correspond to the temperature over which the measurements were taken. ....	104
Figure 6.5: DSC curves for a Zr-CuO nano- laminate for different numbers of bi-layers. Dotted lines are experimental data; the solid lines are from Eq.(6-3). The curves are offset along the y axis for clarity. The points are used to determine the diffusion kinetics, while the dotted line represents the fit of Eq.(6-5) to the experimental data. ....	106
Figure 6.6 Peak shape calculated from Eq.(6-19) for different values of thermal conductance. ....	107
Figure 6.7: Plot of data from Table II. (a) Scaled according to Eq. (6-5). (b) Scaled according to Eq. (6-17).....	109
Figure 6.8: Plot of data from numerical DSC curves for laminar, cylindrical and spherical multilayer systems scaled as given by Eq.(6-5).....	110
Figure 7.1: Geometries of Al-CuO multiple layer nano-laminate modeled by continuum dynamics. (a) Alternating laminates of Al and CuO thin foils with Pt conductors on the two sides. Marked lengths are: L1 = 1mm, L2 = 8 mm, L4 = 1cm, L5 = 1cm, L6 = 500nm, L7 = 500nm. The Z direction of each layer is thin and mapped into a two-dimensional model. (b) X-Y cross section where each block represents a mono-layer of either Al or CuO. A thin Pt wire is embedded in a CuO layer on the top. The Y direction is homogeneous and mapped to a two-dimensional model. (c) The same as geometry (b) except for top layer.....	115

Figure 7.2: Temperature profiles that demonstrates the different stages during joule heating and thermite reaction. (a) $t=0.001s$ . (b) $t=0.025s$ . (c) $t=0.027s$ . The small time and large temperature difference between panels (b) and (c) compared to those between panels (a) and (b) is consistent with the delay time and rapid reaction observed experimentally .....	122
Figure 7.3: Logarithm of time before initiation vs. pre-exponential component with $E_a=150kJ/mol$ and applied potential $V_1=0.1 V$ .....	123
Figure 7.4: Dependence of reaction propagation speed on pre-exponential constant of Eq. (7-6).....	125
Figure 7.5: Dependence of reaction propagation speed on activation energy of Eq. (7-6). .....	125
Figure 7.6: The wire heating experiment. (a) The experimental setup, in which a Pt wire is embedded in the top CuO layer, and Joule Heating is applied by applying constant electric potential on the two sides of the Pt wire. (b) The SEM image of the cross section of the final product. (c) The composition mesh of CuO in the final state in the simulation II. (d) The temperature profile before ignition.....	126
Figure 7.7: Comparison of DSC curve obtained from simulation (a) and from experiments (b). Note that the units of x axis are Kelvin for (a) and Celsius for (b) respectively.....	127
Figure 8.1: Sketch of the family tree for hyperthermia treatments in oncology.....	133
Figure 8.2: Demonstration of the relationship between $SHR(t_p)$ , activation energy and diffusion pre-exponent in nano energetic materials. The plot was made from numerical solution of 1-D diffusion equation with $p=0.2$ at the temperature $36.8\text{ }^\circ\text{C}$ and enthalpy of the reaction is $1kJ/g$ . .....	137
Figure 8.3: A design of nano-composite of maghemite coated nano thermite for hyperthermia treatment.....	138

## **PART 1, GRAIN BOUNDARY**

### **Chapter 1 An Overview of the Computational Study of the Grain Boundary Structure , Energy and Mobility**

#### **1.1 Introduction**

With the advent of high performance computers, computation and simulation approaches are changing the way we learn, view, and study in material science. Yet the value of computation and simulation, as the third pillar of research, standing equally alongside theory and experiment, is still underappreciated. A very similar remark was made in the Presidential Information Technology Advisory Committee <sup>[1]</sup> report: “*Universities...have not effectively recognized the strategic significance of computational science in either their organizational structures or their research and educational planning.*” This has been especially true in the computational study of solids in materials science. There appear to be several reasons for this, the most evident one is that, even today, computational resources are limited compared to most of the problems encountered in the practical study of solids. Different from liquids, gases or powder composites, properties of solid materials depend not only on the macroscopic chemical composition but also on the micro-structure, defects and distribution of constituent chemical elements.

Grain boundaries, for example, are two-dimensional nonequilibrium defects in crystalline solids. It has been proven that many crystalline materials can be strengthened (known as Hall–Petch strengthening<sup>[2]</sup>) by introducing grain boundaries because grain boundaries can impede dislocations motion. In this view, materials with ultra-fine grains would have ultra-high strength. However, this is not true microstructures of nano crystalline material are often thermally unstable because grain boundaries are associated with positive free energy which means that their configurational entropies are smaller than their formation energies. Minimization of the free energy will drive grain boundaries to move, which is the dominating mechanism for grain growth during the annealing of metals. However, it has also been found first by molecular dynamics simulation<sup>[3], [4]</sup> and then confirmed by many experimentalists<sup>[5]–[7]</sup> that solute segregates can stabilize grain boundaries and further make ultra-strong materials possible. From this example, we can see how complex the microstructure–property relationships can be even for the simplest case. To provide an overview of grain boundaries in modern material science and to highlight the increasingly important role that computational study is playing in this field, we divided this chapter into three sections. First, we will briefly review the definitions, terminologies and basic properties of various types of grain boundaries. In the second part, past efforts towards macroscopic scale modeling of grain boundary structure, energy and grain boundary solute segregation will be summarized. The third part in this chapter is intended to give an overview of the achievements and challenges for the computational study of grain boundary motion and in the last section, the contents of the first part of this thesis will be outlined.

## 1.2 Molecular Dynamics and Interatomic Potentials

Molecular dynamics is a straight-forward computational simulation in which the motion of atoms is followed and analyzed under different conditions<sup>[8]</sup>. The chief assumption in this technique is that atoms can be treated as classical particles so that their trajectories are calculated by numerically integrating classical Newton equations of motion for each atom. These equations of motion are coupled through the forces on the atoms. The interatomic forces which determine the dynamics of atoms are a key feature of a MDS. They are also typically the most computationally intensive part of the simulation. The forces on the atoms are derived from the negative gradient of the potential energy function (PEF) which is an empirical function for calculating the potential of the system given all atom positions. Conventionally PEF is split into one-body, two-body, three-body ... terms:

$$U(\mathbf{r}^N) = \sum_i V_1(\mathbf{r}_i) + \sum_i \sum_{j>i} V_2(\mathbf{r}_i, \mathbf{r}_j) + \dots \quad (1-1)$$

And the interatomic forces:

$$\mathbf{F}_i = \nabla_{\mathbf{r}_i} U(\mathbf{r}^N) \quad (1-2)$$

where  $\mathbf{r}_i$  refers to the position of the  $i^{th}$  atom;  $N$  is the total number of atoms;  $U(\mathbf{r}^N)$  is the PEF;  $V_1(\mathbf{r}_i)$  is the one body potential which usually represents the interaction between the  $i^{th}$  atom and an externally applied potential field;  $V_2(\mathbf{r}_i, \mathbf{r}_j)$  is the two-body potential. It is used to describe pair interactions such as the electrostatic, van der Waals or bond interactions. Three body potential and higher order many body potentials are mostly seen in the simulation of organic or biomolecule systems in which energy contribution from bond angles, dihedral angles and so on are significant.

Mathematical forms of PEF came in with great varieties, applicable in different situations. Even for the pair potential, a number of functional forms have been developed, such as Lennard-Jones potential, Morse potential and their countless derivatives<sup>[9]</sup>. Since this section is by no means a complete review of interatomic potentials, we refer the reader to other reviews<sup>[10]-[12]</sup> mentioned in the bibliography.

In practical MDS, the criteria being a good PEF is three fold: (i) accuracy: it should accurately reproduce some set of fitting data from experiments or quantum chemistry models such as density-functional theory; (ii) transferability: it should be also capable of producing physically-reasonable (if not accurate) energies for atomic configurations that are not considered in a given fitting database; (iii) efficiency: it should be computationally efficient so that MDS can: generate sufficient number of samples, contain sufficient number of atoms in the system, and perform for sufficient long time to minimize statistic errors and capture the relevant physics of a given problem.

Experience has demonstrated PEFs that find a compromise between accuracy, transferability and efficiency are based on expressions that are derived from quantum mechanical bonding principles. Potential of Embedded Atom Method (EAM) for metallic system is such an example. Different from conventional pair potential which consider interaction between two particles are not affected by the presence of other atoms, EAM add to the PEF a cohesive energy term which describes the energy of embedding an atom into an local electron gas provided by the neighboring atoms. More detailed description of EAM potential can be found in the Chapter 2 and elsewhere<sup>[11], [13]-[15]</sup>. But see from the EAM formula, i.e. Eq. (2-5), we can see EAM outperforms conventional pair potential for at least

two reasons. First, it is many-body potential in which the metallic bond strength between two atoms is coordinate dependent. This makes EAM an effective potential for pure metal systems. Second, EAM is computationally efficient. By using pair terms for inter-atomic repulsion and the electron density contributions to a given site, the evaluation of the EAM scales as a pair potential despite the many-body aspect of the function that is introduced by an embedding function. It is because of these advantages that EAM has found wide application in the computational study of metals. Throughout this thesis, EAM potential or its direct derivative, modified EAM<sup>[14]</sup>, is used unless specified.

### **1.3 Basic Conceptions of Grain Boundaries**

A grain boundary is an interface separating two crystals (grains) of the same crystal but of different orientations. Grain boundaries are planar defects because the discrepancy of crystal orientations across the grain boundaries brings in misfit energy and stresses. Despite grain boundaries being recognized and studied for centuries, they are still among the least understood structures in materials science because of their extremely complex structures.

In general, the geometry of a grain boundary has eight degrees of freedoms (DOFs): Three Euler angles (3 DOFs) and a three component translation vector (3 DOFs) to fully describe the orientation of one grain with respect to one adjacent grain, plus two independent variables (2 DOFs) to define the inclination of the grain boundary plan. Only five of the eight parameters are important, however, because the translation vectors are often constrained by the geometries such that the energy of the system reaches the minimum. For instance, in research by Tschopp and McDowell<sup>[16]</sup>, tilt grain boundaries with fixed tilt angles and fixed

inclination of grain boundary plane but variable translation vector were energy minimized by molecular dynamics simulation using an embedded atom model (EAM) potential so that the minimum energy configuration can be found. Their results showed very good agreement with high-resolution transmission electron microscopy images of experimental grain boundary structures.

To simplify the description of grain boundary crystallography, a number of variables or terminologies are frequently used in the literature. Some of them are summarized below:

### **Tilt and twist grain boundaries**

Grain boundaries can be classified by the relationship between the grain orientation rotation axis and the grain boundary plane. If they are parallel, as illustrated in Figure 1.1a, they are called tilt angle grain boundaries. If they are perpendicular, as shown in Figure 1.1b, (i.e. the rotation axis is parallel to the normal vector of the grain boundary plane) they are termed twist grain boundaries. If they are neither parallel nor perpendicular to each other, they belong to the group of mixed grain boundaries. A mixed grain boundary is often viewed as a linear combination of a tilt and a twist grain boundary by projecting its rotation vector to the vectors parallel and perpendicular to the grain boundary plane. The rotation angle  $\theta$ , as illustrated in Figure 1.1, is also known as the “misorientation” or “disorientation angle”.

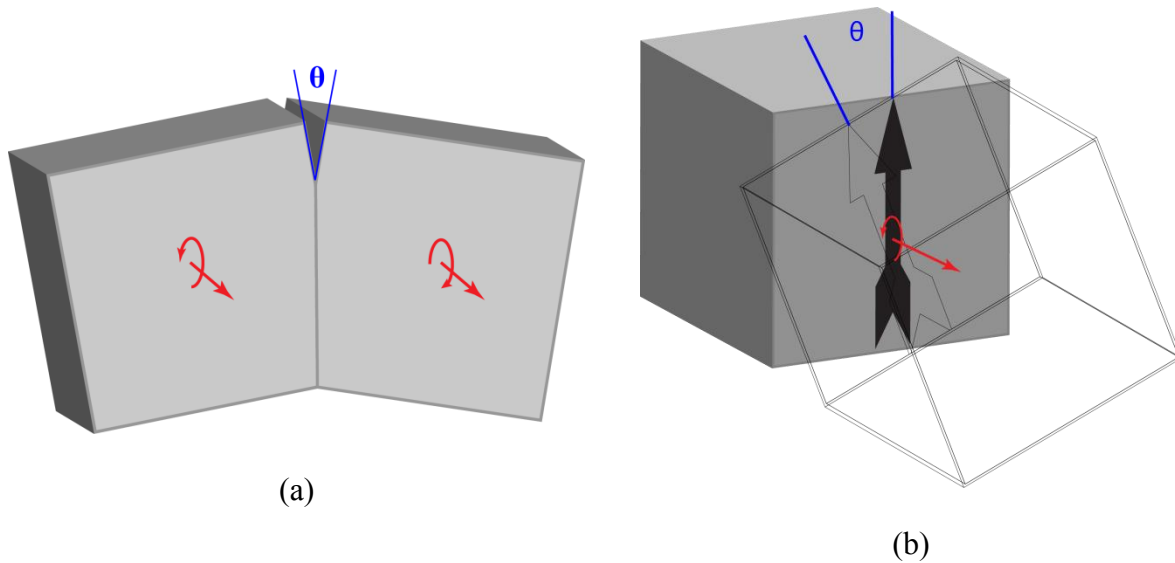


Figure 1.1: Illustration of a pure tilt grain boundary (a) and a pure twist grain boundary (b).

### Low and high angle grain boundaries

Grain boundaries with small (usually  $\theta \leq 15^\circ$ ) misorientation between adjacent grains are called low angle grain boundaries; accordingly, those who have large misorientation are called high angle grain boundaries. This way of classifying grain boundaries is not precise and the dividing line often varies from one research paper to another. However, it is an important concept that is frequently seen in the literature. This is because low angle grain boundaries can often be approximated as an array of dislocations (edge dislocations for tilt, and twist dislocations for twist grain boundaries), but this approximation is invalid in the high angle region.

Illustrated in Figure 1.2 are the structures of symmetric tilt angle grain boundaries. It is easy to see that grain boundaries with low tilt angle can be well represented by an array of

edge dislocations. But in high tilt angle cases, the edge dislocations are so close that the dislocation cores begin to overlap and the definition of the Burger's vector become unclear.

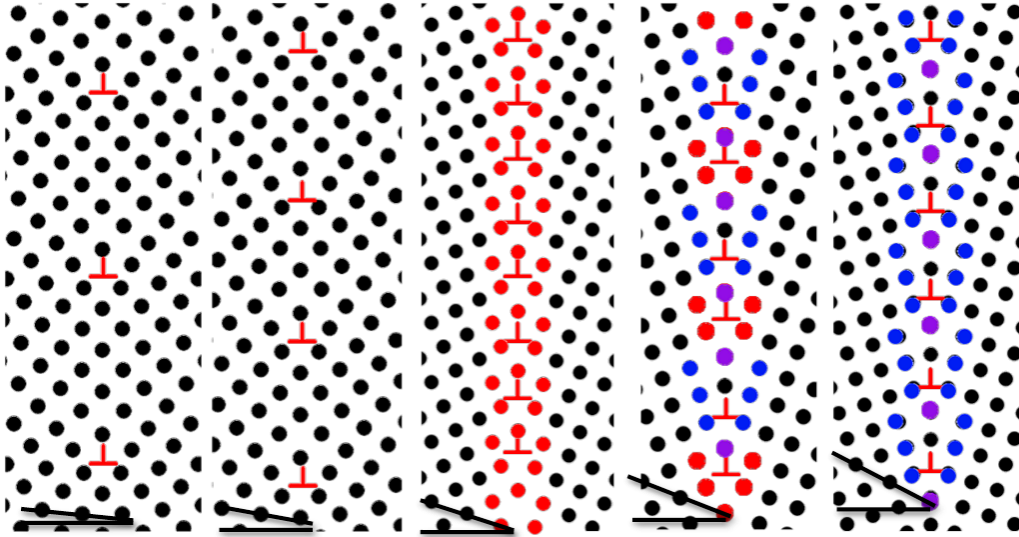


Figure 1.2: Atomic configurations of symmetric tilt angle grain boundaries from low to high misorientation. The bottom angular lines show the half of the misorientation angle, i.e.  $\theta/2$ . From left to right,  $\theta/2$  values are  $3.02^\circ$ ,  $6.04^\circ$ ,  $18.44^\circ$ ,  $23.20^\circ$  and  $26.57^\circ$  respectively.

Based on the idea that low angle grain boundaries can be represented by an array of dislocations, Read and Shockley developed the expression for the energies of low angle grain boundaries

$$E_{gb} = \theta(A - B \ln \theta) \quad (1-3)$$

where A and B are constants that depend on the types of dislocations and the elastic constants of the material.

Figure 1.3 demonstrates the grain boundary energy prediction based on Eq. (1-3) and from molecular dynamics simulation with an EAM potential<sup>[11]</sup>. The results from the Read and Shockley formula and full atomistic calculation are in good agreement in the low angle region. In high angle region, the Read and Shockley formula predicts an energy decrease for high-angle grain boundaries but in the EAM calculation, the energies remain almost constant for the high angle grain boundaries.

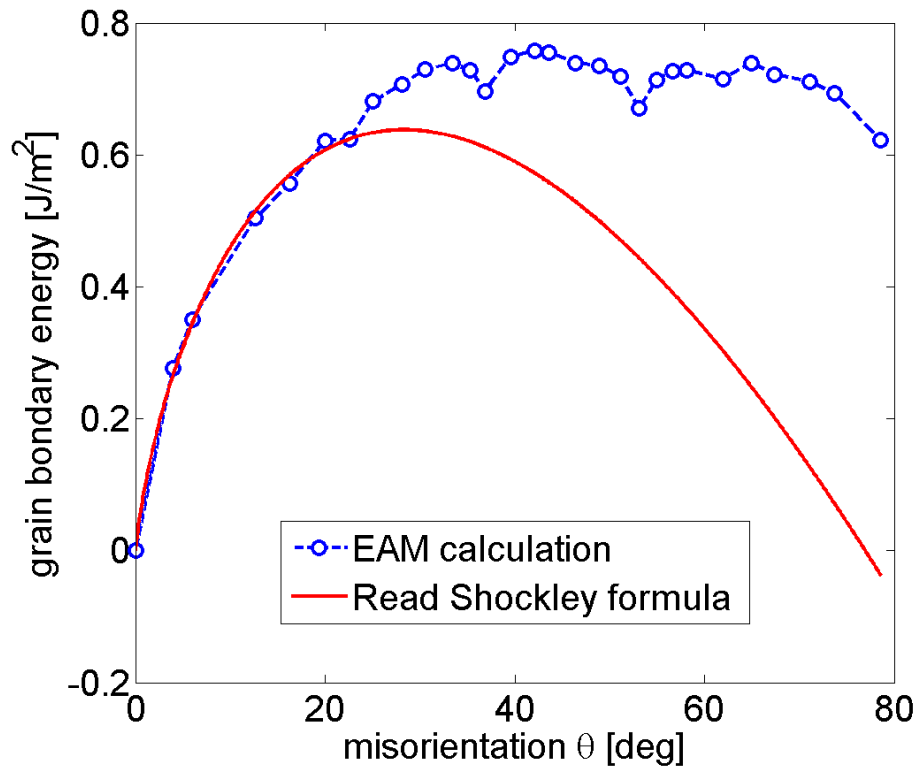


Figure 1.3: Dependence of symmetric tilt angle grain boundary energies on the misorientation angles. The dotted circles are computed from molecular dynamics simulation of FCC copper using EAM potential. The solid curve is computed from the Read Shockley formula.

## Coincidence Site Lattice (CSL) and the Reciprocal Density

Although the expression “CSL theory” is frequently used in the research papers, CSL itself is not a theory but an imaginary lattice formed by the coincide sites of two regular lattices with special misorientation angles. For instance, shown in the Figure 1.4 is a demonstration of a  $\Sigma 5$  structure. The blue and green circles are the crystal structure (simple cubic) of the same structure. The lattice formed by big red circles, i.e. coincide sites is known as the CSL.  $\Sigma$  is called the reciprocal density; it is defined as a half of the number of atoms included in one CSL cell. In this example, four green, four blue and 8 coinciding vertices (shared by 4 CSL cells) are included in one CSL cell. Therefore the  $\Sigma$  value for the structure is  $(4+4+4 \times 1/4)/2=5$ .

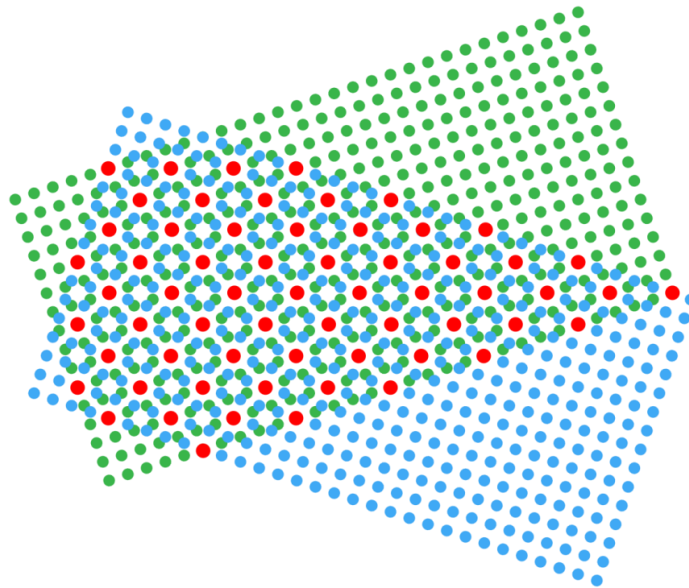


Figure 1.4: Illustration of a simple cubic  $\Sigma 5$  CSL structure.

## 1.4 Coarse Grained Representation of Equilibrium Grain Boundaries

Serves as supplementary for Chapter 2, this section will present an historical review of coarse grained models of grain boundaries. As mentioned in the previous section, grain boundaries are often treated as an array of dislocations. This treatment can be traced back to 1950 when the well-known relationship between grain boundary energy and misorientation angle, *i.e.* Eq. (3-9), was derived<sup>[17]</sup>. A similar express was also derived by Nabarro in 1952<sup>[18]</sup> by integrating the elastic forces on each dislocation from its actual position to infinite distances. In these two cases, grain boundaries were represented by a finite number of equally spaced dislocations. However, in 1953, James<sup>[19]</sup> pointed out that a grain boundary is better represented by infinite number of dislocations. The stress fields of the two resemble one another only at the distance from the wall nearer than the dislocation spacing in the wall. Despite the huge success of the dislocation wall model for grain boundaries in the 1950s, researchers found difficulties fitting this model to high angle grain boundaries. In 1960, James<sup>[20]</sup> examined the dislocation wall model for high angle tilt grain boundaries and declared that if the interactions of cores of the dislocations are taken into consideration, a dislocation wall model can well represent grain boundaries even in the high tilt angle region. Another effort in extending the dislocation wall model to the high angle grain boundaries is from Brandon, who proved that the dislocation wall model is compatible with coincidence lattice model in the high-angle region<sup>[21]</sup>.

Started from the 1960s, researchers started to realize that grain boundaries can be better described by disclinations instead of dislocations. In 1966 Eshelby<sup>[22]</sup> found that elastic fields of dislocations can be computed easier by inserting and removing a narrow wedge

disclination into the material. In 1972, Li<sup>[23]</sup> proposed that grain boundaries should be considered as being made of disclinations instead of dislocations because a grain boundary is a rotational defect and so are disclinations (dislocations are translational defects). Moreover, similar to the conclusion by Eshelby<sup>[22]</sup>, Li discovered that the energy of a symmetric tilt grain boundary (STGB) can be computed easier using the disclination model than the dislocation model. In Li's paper<sup>[23]</sup>, STGBs are made of equally spaced (spacing  $H$ ) disclination dipoles whose strengths are  $\omega$  as shown in the Figure 1.5.

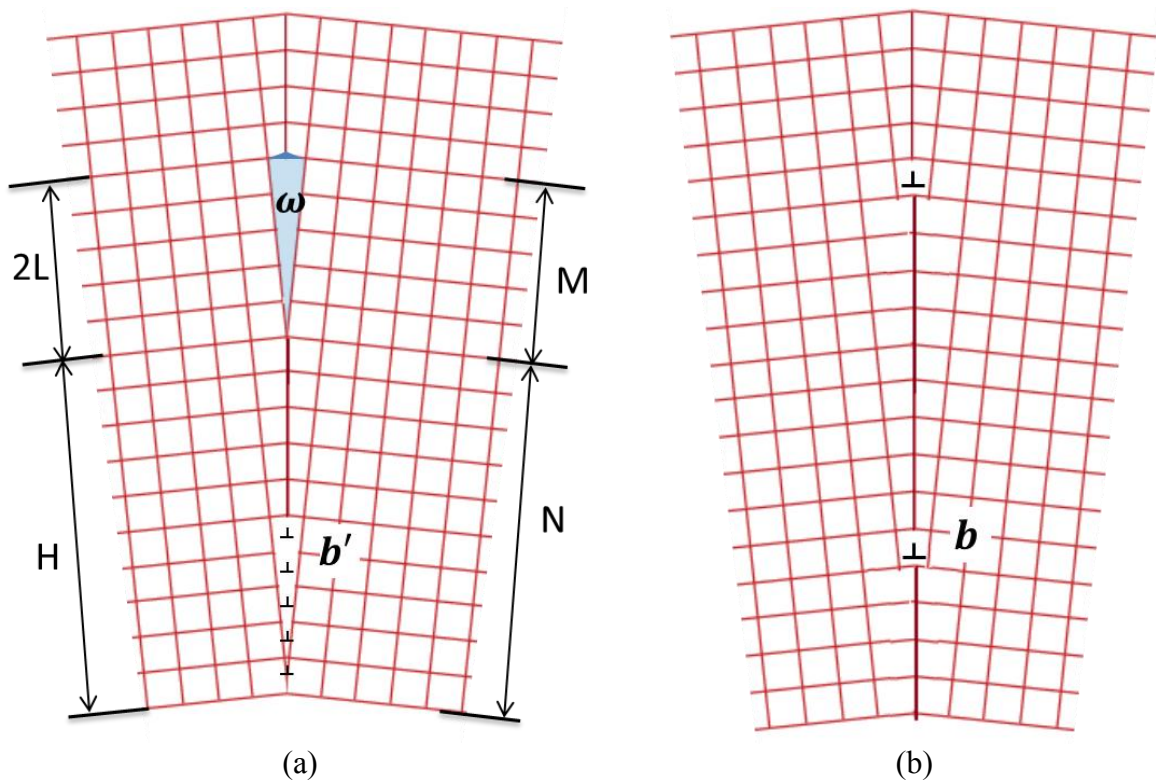


Figure 1.5: Demonstration of (a) disclination model and (b) dislocation model of a symmetric tilt angle grain boundary.

Li further assumed that each disclination can be viewed as one low angle infinite dislocation wall consisting of  $M$  edge dislocations of Burger's vector  $b'$ . Further some imaginary dislocations with Burger's vector of zero were added to this picture so that the geometry and the number of dislocations have a relationship  $M/N = 2L/H$ , where  $2L$  is the height of the disclination dipole as illustrated in Figure 1.5. The energy of this simple STGB can then be expressed as the sum of all disclinations plus the elastic energies between every two disclinations.

$$E_{gb} = \frac{\mu b'}{4\pi(1-\nu)H} \left[ M \ln \frac{2\pi r_0}{eH} + 2 \sum_{I=0}^{M-1} (M-I) \ln \left( 2 \sin \frac{I\pi}{N} \right) \right] \quad (1-4)$$

where  $\mu$  and  $\nu$  are shear modulus and Poisson ratio of the investigated material.

Shortly after Eq. (1-4) was derived, Shih and Li<sup>[24]</sup> extended the idea of disclination models to the grain boundaries that consist of alternate disclination dipoles of  $\omega_1$  with height  $2L_1$  and  $\omega_2$  with height  $2L_2$ . Moreover he rewrote the strain energy part the Eq. (1-4) by replacing the summation with integration to make it more precise and independent of imaginary Burger's vectors of  $b'$ . The elastic strain energy of the STGB now is

$$E_{el} = \frac{\mu \Delta \omega^2}{8\pi(1-\nu)} \frac{H}{4\pi^2} f(\lambda_1) \quad (1-5)$$

where  $\Delta \omega = |\omega_1 - \omega_2|$  and function  $f(\lambda_1)$  is given in Eq. (2-3).

Despite the huge success of Eq. (1-4) and Eq.(1-5), they are still continuum approaches where atomic structure is ignored. The question that whether they are compatible with atomistic approaches was not answered until 1983 by Sutton and Vitek. In their early

work Sutton and Vitek<sup>[25]</sup> found that some atomistic structural patterns show up repeatedly in the grain boundaries. For example, illustrated in Figure 1.6 are the atomic configurations of the last three grain boundaries in Figure 1.2. It can be seen clearly that Figure 1.6a and Figure 1.6c consist of monotonic repeating structures and historically, they are defined as “B” and “C” structural units, respectively. Figure 1.6b, on the other hand, is made of alternating “B” and “C” structural units. Grain boundaries that are composed of contiguous sequences of one type of fundamental structural units are called “favored boundaries” which usually have low reciprocal density, *i.e.*  $\Sigma$  value, of coincidence lattice and low strain energy.

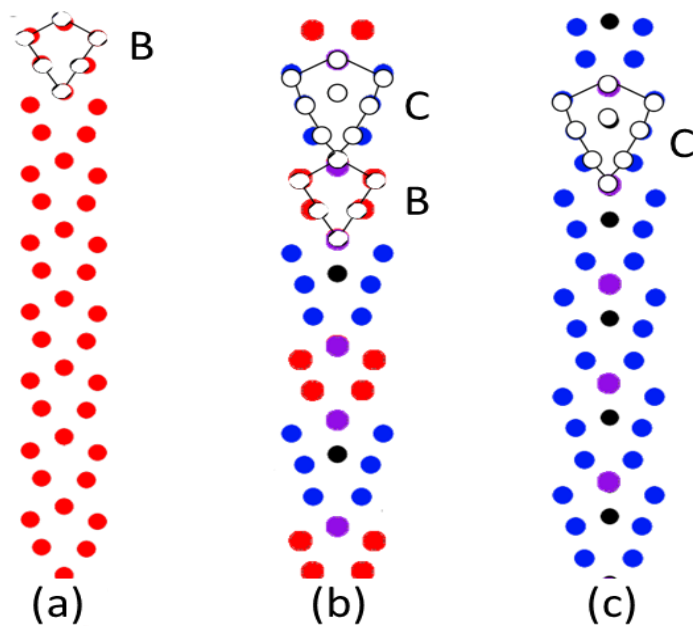


Figure 1.6: Illustration of the structural units model for a STGB. The three grain boundaries shown here are the same as the last three grain boundaries shown in Figure 1.2. Atoms that are not near the grain boundaries are hidden.

In 1986, Wang and Vitek<sup>[26]</sup> developed a way to compute grain boundary energies based on the structural units model and the dislocation model for grain boundaries. In their paper<sup>[26]</sup>, the total energy of a grain boundary consists of the energy of a reference structure, the core energy and the elastic energy:

$$E_{gb} = \gamma_{\alpha} + \frac{1}{d} \left[ E_c + \mu b^2 \ln \frac{eb}{2\pi r_0} \right] \quad (1-6)$$

where  $d$  is the average spacing of the dislocations and  $b$  the magnitude of their Burger's vectors.  $\gamma_{\alpha}$  is the reference energy and were calculated from atomistic models of the favored grain boundaries. For instance,  $\gamma_B$  and  $\gamma_C$  are the energies of the grain boundaries shown in Figure 1.6a and Figure 1.6c respectively.  $E_c \approx \gamma_{\alpha\beta}/2$ , is the core energy and  $\gamma_{\alpha\beta}$  is the energy of the boundary that has an equal number of  $\alpha$  and  $\beta$  units. For instance,  $\gamma_{BC}$  is the energy of the grain boundary (b) in Figure 1.6.

Formula (1-4) was based on the dislocation model and it involves many unnecessary approximations, such as  $E_c \approx \gamma_{\alpha\beta}/2$ . In 1989, Gertsman *et. al.* proposed a disclination structural unit model (DSUM) which treats grain boundary as a disclination dipole wall and each disclination dipole has a unique corresponding structural unit. A detailed formulation can be found in Chapter 2 from Eq. (2-3) to Eq. (2-5). It has been established in the literature that the DSUM is one of the best models for describing both grain boundary structure and energy<sup>[27]-[31], [12]</sup>.

## 1.5 Approaches to Compute Grain Boundary Mobilities

Grain boundary motion is an important aspect to many recovery processes such as grain growth during recrystallization post cold work hardening. Despite many efforts aimed at understanding the details of grain boundary migration, the complexity of the atom dynamics associated with grain boundary motion, and how these dynamics are coupled to internal stresses and external applied strains, makes it one of the major unresolved problems in materials science<sup>[32]</sup>.

During grain growth different grain boundaries can behave quite differently. In most annealing experiments, grain growth represents an average behavior of many types of grain boundaries. This limits the ability to understand grain boundary dynamics of one specific interface type. Even in bi-crystal experiments<sup>[33], [34]</sup> it is still a formidable task to study migration of single grain boundaries throughout a large range of misorientation angles. In contrast, molecular dynamics simulation can provide unique insight and predicted properties of specific grain boundaries that complement experimental capabilities<sup>[35]</sup>.

Characterizing grain boundary properties typically starts with mobility, which is defined as the linear coefficient relating the grain boundary normal velocity  $v_{GB}$  to the driving force (pressure)  $P$ , i.e.  $M \equiv v_{GB}/P$ . For low-angle tilt grain boundaries, which are typically modeled by arrays of dislocations, the mobility can be analytically approximated by the Peach-Koehler force multiplied by the number of dislocations per unit length (as well as by other similar expressions)<sup>[36]–[38]</sup>. This leads to an analytic expression for mobility with Arrhenius temperature dependence and a value that is inversely proportional to tilt angle. While activated mobility is usually observed, the inverse relation between mobility and tilt

angle is not a typical feature of experimental or atomistic simulation results. For higher tilt angles, assuming that grain boundary motion is closely related to atom diffusion leads to the Burke-Turnbull expression for grain boundary velocity of the form

$$v = \frac{\Omega}{a^2} \left[ \eta e^{-\frac{Q}{kT}} - \eta e^{-\frac{Q+p\Omega}{kT}} \right] \quad (1-7)$$

where  $\Omega$  is the volume per atom,  $a$  is the lattice spacing,  $\eta$  is an attempt frequency,  $Q$  is an activation energy,  $k$  is Boltzmann's constant,  $T$  is temperature, and  $p$  is pressure. In the limit that  $p\Omega \gg kT$ , velocity and pressure are proportional to one another with proportionality constant (i.e. mobility):

$$M = \frac{\eta a^4}{kT} e^{-\frac{Q}{kT}} \quad (1-8)$$

In this expression the mobility is an activated process, but is independent of tilt angle.

Based on both experimental studies and molecular dynamics simulation, grain boundary mobilities depend on many factors, but with a dependence that is not well understood. There are, however, several trends that have become apparent. First, high angle grain boundaries tend to be more mobile than low angle structures, a trend that in general appears valid for both twist and tilt structures.<sup>[39]</sup> In addition, in contrast to the analytic theory mentioned above the mobility of low angle grain boundaries tend to increase with increasing misorientation angle in a power law relationship  $M = k\theta^\alpha$ <sup>[39]</sup>. Second, mobility typically shows Arrhenius behavior with respect to temperature, in agreement with the expression above. Third, the mobility of twist structures tend to be higher than tilt grain boundaries while activation energies are similar<sup>[40]</sup>. Forth, mobilities are found to be

different for planar and curved grain boundaries and highly sensitive to impurity and vacancy concentrations. <sup>[41]</sup>.

To help establish relations between structure and mobility for individual grain boundaries, Foiles and co-workers used molecular dynamics with an artificial driving force method mentioned above <sup>[42]</sup> to calculate energies and mobilities for a total of 388 grain boundaries in nickel. These interfaces included  $\langle 111 \rangle$ ,  $\langle 100 \rangle$  twist, and  $\langle 110 \rangle$ ,  $\langle 111 \rangle$ ,  $\langle 100 \rangle$  symmetric tilt and coherent twin grain boundaries<sup>[35]</sup>. They reported that over 25% of the grain boundaries migrate via a mechanism that couples shear stress to motion; this included a majority of the non- $\Sigma 3$  structures that had the highest mobilities. Of the remaining structures, the incoherent  $\Sigma 3$  twins had an anomalously high mobility, while some other boundaries (e.g. all of the  $\langle 111 \rangle$  twist boundaries) remained static on the time scale of the simulations. Thermal activation energies were also found to vary widely, with some migration mechanisms not having any measured activation barriers. They also reported thermal roughening of the grain boundaries, with substantial increases in grain boundary mobility above the roughening temperatures for each boundary. Despite the wide range of different properties for the different structures, no correlations were discovered between mobility and scalar quantities such as misorientation angle, grain boundary energy,  $\Sigma$  value or excess volume.

The definition of grain boundary mobility implies a linear relationship between grain boundary normal velocity and driving force. Both analytic theory (c.f. Eq.(1-7)) and molecular dynamics simulation, however, predict non-linear behavior <sup>[43]</sup>, and different authors have different explanations for this dependence. Godiksen *et. al.* <sup>[40]</sup> found that grain

boundary velocity is proportional to driving force ( $v_{GB} \propto P$ ) for twist grain boundary motion, but is nonlinear ( $v_{GB} \propto P^2$ ) for tilt grain boundaries. This result is ascribed to local interactions between the grain boundary and nearby dislocations. Another tentative explanation has been proposed by Zhang et al <sup>[44]</sup> who attributed the nonlinearity to an increase in effective activation barrier with increasing applied driving force.

A mechanism based on Eq.(3) was proposed by Zhou and Mohles <sup>[43]</sup>, who suggested that the approximation leading to Eq.(4) is invalid for the high forces needed to observe grain boundary motion in MDS. They suggested that the low driving force limit can be achieved by extrapolating data from high driving force simulations. Based on this idea, Zhou and Mohles determined misorientation-angle-dependent grain boundary mobilities and migration activation energies by molecular dynamics simulation using the artificial driving force method <sup>[42]</sup>. In their work, a series of flat twist  $\langle 110 \rangle$  grain boundaries with various  $\Sigma$  values and misorientations were investigated. The resultant mobilities of small ( $\leq 25^\circ$ ) and large misorientation grain boundaries are about  $1 \times 10^{-9} \text{m}^4 \text{J}^{-1} \text{s}^{-1}$  and  $1 \times 10^{-8} \text{m}^4 \text{J}^{-1} \text{s}^{-1}$  respectively.

One way of avoiding the nonlinearity resulting from a high driving force is to perform equilibrium molecular dynamics simulation and obtain the mobility according to the fluctuation dissipation theorem. Trautt *et al.* implemented this idea by taking grain boundary migration as analogous to a one-dimensional random walk, and proposed that mobility is linearly dependent on the fluctuation of the mean interface position <sup>[45]</sup>. They suggested that mobilities of planar grain boundaries at the low driving force limit (i.e. true mobilities) are an order of magnitude higher than the mobilities measured with high driving force methods but

similar to those extracted from molecular dynamics simulation with a curvature driving force.

Similar to grain boundary mobility, there is no simple rule to determine activation energies of grain boundary migration because the energies depend on too many variables such as grain boundary type, impurity concentration, and shape. Activation energies computed from molecular dynamics simulation, for example, are often lower than those determined from experiment, <sup>[43], [46]</sup>. One contributing factor to this observation is likely the presence of impurities in the experimental systems that are not present in the simulations <sup>[35]</sup>.

A distinct transition in activation energy between low angle and high angle grain boundaries, irrespective of planar or curved type, at approximately the same misorientation was detected numerically <sup>[43]</sup> and experimentally <sup>[47]</sup>. The transition angle measured is about 15 ° for both  $\langle 110 \rangle$  twist <sup>[43]</sup> and  $\langle 100 \rangle$  twist boundaries, <sup>[46]</sup>, 14.1 ° for  $\langle 111 \rangle$  symmetric tilt boundaries <sup>[47]</sup>, 8.6 ° for  $\langle 100 \rangle$  symmetric tilt boundaries <sup>[36]</sup> and 13.6 ° for  $\langle 112 \rangle$  symmetric tilt <sup>[48]</sup> grain boundaries. The first two transition angles were determined from molecular dynamics simulation while the latter three were measured experimentally. The agreement suggests that molecular dynamics simulation is able to capture the important aspects of this transition.

In a recent experiment by Ruper et al., it was observed that grain boundary migration in nanocrystalline aluminum thin films is governed by shear stresses that produce distortion work rather than normal stresses assumed in conventional theory. <sup>[49]</sup>. Shear stress as driving force for grain boundary migration has also been reported in other experimental studies <sup>[32], [36], [48]</sup>. Molecular dynamics simulation results are in agreement with these experimental

studies<sup>[50], [51]</sup>. By performing molecular dynamics simulation for symmetric  $\langle 100 \rangle$  tilt grain boundary systems in copper, Cahn *et al.* confirmed that the normal motion of planar grain boundaries can be driven by shear stress and the ratio of normal to tangential translation of a grain boundary is a constant independent of temperature or of the magnitude of the applied shear stress. In a study by Olmsted *et al.*<sup>[35]</sup>, they found that even under a normal driving force significant shear can be built up during normal motion of planar grain boundaries. They further claimed that the normal, diffusion controlled mechanism exists in all grain boundaries, but it is often overshadowed by the fast shear coupled mechanism if the latter is allowed geometrically, for instance if lateral translation is unconstrained.

## **1.6 Overview of Chapters 2 – 4**

In Chapter 2, considerable efforts will be placed on developing multi-scale, coarse grained models of nanostructured materials. Multiscale modeling describes a wide range of computational activities that are aimed at describing phenomenon of materials at a fine scale level by modeling or simulating at a coarser scale. More specifically, in conventional materials science, symmetric tilt angle grain boundaries are considered as planar defects. However, according to coincidence site lattice theory and disclination structural units model, we found that symmetric tilt angle grain boundaries can be simplified and represented by linear models. This approximation is attractive because it can drastically reduce the computational efforts by reducing dimensions of conformation space even compared to the conventional multiscale methods that save computational time by coarse graining groups of atoms.

The third chapter is dedicated to computing mobilities of symmetric tilt grain boundaries for face-centered cubic copper and detecting grain boundary migration mechanisms. A limitation of applying computation and simulation tools in material science is that most available methods have narrow and strict application ranges. Scholars must be very aware of the approximations made and how much the error will be brought in before making use of one method. What is even worse is that limits on the applicability of those computation and simulation methods are undefined for a wide range of methods. This circumstance is even worse when it comes to computer simulation of non-equilibrium processes such as grain boundary migration because many competing mechanisms are in presence simultaneously. Conventional molecular dynamics simulation of grain boundary migration tends to predict an abnormally high mobility and low activation energy for grain boundary motion. In Chapter 3, we first follow the conventional way of computing grain boundary mobilities using molecular dynamics and then demonstrate how the resulting mobilities and activation energies can be better interpreted if various migration mechanism are taken into consideration.

In the annealing process of multi-crystalline materials, dislocation gliding and climbing are generally considered as the two most important atomistic mechanisms. However, occurrences of these two events are not uniformly distributed during the recovery phase of an actual material because climbing is often overshadowed by gliding if the dislocation is straight and of edge type, but on the other hand, the gliding of a dislocation is prohibited if it has a jog with edge character. Unfortunately, until now our understanding regarding the competing micro-scale mechanisms of grain boundary dislocation migration is

very poor despite the fact that computational studies have been being carried on for decades. One objective of Chapter 4 is to present in depth discussions on characterizing and categorizing various atomic mechanisms during the annealing process of multi-crystalline materials. The distinguishing feature of this thesis is that it focuses on not only presenting the results but also developing useful methodologies and computer algorithms for analyzing non-equilibrium processes associated with grain boundaries and dislocations.

## **Chapter 2 Solute Segregation Energy and Grain Boundary Energy Calculation Based On Disclination Structural Units Model and Perturbation Methods**

It has been shown in many experiments that solute atoms segregate to and can stabilize grain boundaries in dilute alloys due to the decrease of grain boundary energies after segregation. In this chapter, we propose a few computational tools for studying the stabilization effects of solute atoms in pure metal grain boundary systems from an energy perspective. Tools are (i) a quick way to locate favorite segregation sites for atomistic models, (ii) a semi-analytical formula to compute the grain boundary energy for low sigma grain boundaries with dilute solute segregate and (iii) a highly-efficient method to calculate the segregation energy of solute atoms at all possible lattice sites using perturbation techniques together with an extended disclination structural units model.

### **2.1 Introduction**

The investigation of grain boundary structure and mechanical properties of dilute alloy systems is of substantial scientific and technological interest due to its application in studying solute segregation<sup>[52]</sup> and grain boundary stabilization<sup>[53][5]</sup>. For instance, grain boundary mobility measured in bicrystal systems has been found to be sensitive to impurity concentrations<sup>[54]</sup>. Even extremely small quantities of tellurium in high purity copper<sup>[55]</sup> and silver in high purity lead<sup>[56]</sup> have pronounced effect on their recrystallization processes. These effects are widely agreed as a result of solute atoms concentrating on the grain boundaries. According to work by Seah *et. al*, the molar content ratio of solute atoms at grain

boundaries and in bulk metals can be as high as 10,000<sup>[52]</sup>. To investigate the effects of solute atoms on the mechanical behavior of grain boundary systems, one must firstly be able to compute the grain boundary energies with solute atoms at various lattice sites and moving the solute atoms from those sites to the grain boundary.

Conventionally, atom structures and molecular dynamics (MD) or first principle calculations are required to compute these energies. However both atom models building and micro scale simulations require lots of efforts to complete. A practical challenge is how to compute these energies without building atom level models or perform exhaustive micro scale simulations. For simple pure metal systems with low  $\Sigma$  boundaries, it is a solved problem. It has been shown that grain boundary energy of pure metal system, can be computed from the disclination structural units model (DSUM) <sup>[23], [26], [29]</sup> which is a macroscopic model based on linear elasticity theory that does not require any information of atom level structures (See Chapter 1 for details). However, when solute atoms are included in the system, the case becomes complicated because the chemical interactions have been changed around the solute atoms but linear elasticity does not taken these changes into consideration. Moreover, the energy change of introducing a solute atom is position dependent and is almost impossible to be computed without the knowledge of the atomic structure of the system. In this chapter, we propose that energy of a grain boundary with solute segregates can be calculated quickly for the following two cases.

1. The minimum possible grain boundary energy with given molar content of solute atoms. Even through the number of configurations for solute atom distributions are

enormous, the configurations that produce the lowest grain boundary energies are relatively fixed.

2. The dilute solute case. In this case, interactions between solute atoms are considered weak compared to the energy of introducing these solute atoms. Then overall potential energy can be treated as a function of segregate positions only.

In the following text, a brief review of the background knowledge for computations of both cases is given first. This section contains three parts. First, the formulation of the DSUM theory is presented. Methods to categorize and compute solute segregation energy levels are then introduced. In the third part, we report a method to quickly compute the energy change of introducing single solute atoms at arbitrary lattice sites with minimum knowledge of atom structures and computational effort. In the following section, 30 symmetrical tilt angle grain boundaries with various misorientation angles were built for four alloy systems. All-atom molecular dynamics simulations were performed firstly to obtain the stabilization energies and grain boundary energies. Then those values were compared to the respective values computed from the formulas proposed in the last section to confirm the validity of our methods.

## 2.2 Theory

First proposed by Sutton and Vitek<sup>[25], [57], [58]</sup>, further developed by Li<sup>[23]</sup> for pure metal systems (see Chapter 1), the DSUM uses a limited number, usually three or four, of low  $\Sigma$  grain boundaries as structural units to calculate the overall grain boundary energy of

high  $\Sigma$  grain boundaries. Here  $\Sigma$  is the reciprocal density of coincidence sites. The DSUM has proven to lead to reasonable energy estimates for several pure metal systems <sup>[25], [27], [59]</sup> and a few covalent materials such as silicon and diamond <sup>[29]</sup>. Recently, Purohit, et. al successfully applied the DSUM to a Pb-Al alloy system<sup>[28]</sup>. However, later calculation suggested that the method in <sup>[28]</sup> is not extensible to other alloy systems. In this work, we extend the power of both atomistic modeling and DSUM method to solute-stabilized systems.

The DSUM describes a grain boundary with misorientation angle  $\theta$  as a linear combination of alternating segments of two specific disclination units whose misorientation angles are  $\theta_1, \theta_2$  respectively. The elastic energy of the grain boundary is therefore an expression of partial disclination dipole strength  $\omega = |\theta_1 - \theta_2|$ , where  $\theta$  is then angle of structural units shown

$$E_{GB}^{pure} = \frac{n_1 d_1 \varepsilon_1 + n_2 d_2 \varepsilon_2}{H} + E_{elastic} + \alpha \frac{G a_0^2 \omega^2 n}{2\pi^3 (1 - \nu) H} \quad (2-1)$$

with

$$E_{elastic} = \frac{nG\omega^2 H}{32\pi^3(1-\nu)} \left\{ f(n\lambda) + \sum_{i=1}^{n-1} \sum_{j=i+1}^n [f(\tilde{y}_j - \tilde{y}_i + \lambda) - 2f(\tilde{y}_j - \tilde{y}_i) + f(\tilde{y}_j - \tilde{y}_i - \lambda)] \right\} \quad (2-2)$$

where  $\lambda = \pi d_2 / H$ ,  $\tilde{y}_i = \pi y_i / H$ ,  $y_i$  are the coordination of disclination dipoles.,  $n_i, d_i, \varepsilon_i$  are, respectively, the number, length, and energies of specific disclination units and  $H = n_1 d_1 + n_2 d_2$  is the period of the grain boundary.

The first term on the right side of Eq. (2-1) is the weighted sum of the energies of individual structure units. The second term describes the elastic energy of a disclination

dipole wall (DDW) which is the sum of the interaction energies composing disclination structural units. Function  $f(t)$  is given by

$$f(t) = -16 \int_0^t (t - v) \ln[2 \sin(v)] dv \quad (2-3)$$

To extend Eq.(2-1) ~ (2-3) to dilute alloy system, we added one term to the right side of Eq. (2-1)

$$\tilde{E}_{GB}^{\text{alloy}} = \tilde{E}_{GB}^{\text{pure}} + \tilde{E}_{\text{sub}} \quad (2-4)$$

where the term  $\tilde{E}_{\text{sub}}$  is called the substitution energy, it measures the energy change of replacing a metal atom with a solute atom in the grain boundary system. The tilde symbol denotes that the energies are obtained from fully relaxed atom structures at 0 K. The substitution energy varies from site to site due to the lattice disordering near the grain boundaries.

Generally speaking solute atoms tend to occupy those lattice sites near or in the grain boundary. This behavior is known as solute segregation. To determine the energetically preferred segregation sites for solute atoms, we need to find a way to estimate the substitution energy with respect to each lattice site in an atomistic model. In our work, this calculation is done by modifying the EAM formula. In the framework of the EAM potential, the energy of atom  $i$  is given by

$$E_i = F_\alpha \left[ \sum_{i \neq j} \rho_\beta(r_{ij}) \right] + \frac{1}{2} \sum_{i \neq j} \phi_{\alpha\beta}(r_{ij}) \quad (2-5)$$

where  $r_{ij}$  is the distance between atom  $i$  and  $j$ ,  $F_\alpha$  is embedding function with respect to electron density,  $\rho_\beta$  is the spherically averaged atomic density function,  $\phi_{\alpha\beta}$  is the pair

potential function, and  $\alpha, \beta$  are the atom types of atom  $i$  and  $j$ . Here we define an *inplace substitutional energy* ( $E^{ise}$ ) as the energy difference when the atom at site  $i$  with type  $\alpha$  is replaced by new atom  $\beta$  without atomic structure relaxation.. The inplace substitutional energy based on Eq. (2-4) can be expressed as

$$E_i^{ise} = \sum_{j \neq i} \frac{dF_\tau}{d\rho} [\rho_\alpha(r_{ij}) - \rho_\beta(r_{ij})] + \sum_{j \neq i} \delta F_{\alpha,\beta} [\rho_\alpha(r_{ij})] + \sum_{j \neq i} \delta \phi_{\alpha,\beta}(r_{ij}) \quad (2-6)$$

where  $\delta F_{\alpha,\beta} \equiv F_\alpha - F_\beta$ , and  $\delta \phi_{\alpha,\beta} = \phi_{\alpha\tau} - \phi_{\beta\tau}$  are the functional differences and  $\tau$  is the atom type of the atom at site  $j$ . We have implemented this functionality as a plugin in the LAMMPS molecular simulation code<sup>[60]</sup>. Eq.(2-6) is also applicable to other analytic potentials, for example, pairwise additive potentials (which are a special case of the EAM).

This energy is different from the substitution energy in Eq. (2-4). From a macroscopic viewpoint, the substitution energy has two contributions. One is from the chemical environment change brought by introducing a segregate atom. In this article we refer to the in-place substitution energy as the chemical contribution. The elastic contribution comes from the structural relaxation. To calculate the true substitution energy, the in-place substitute structure must be fully relaxed to achieve a stable structure. The energy decrease in the structure optimization step is given in Eq. (2-9) and discussed in more detail below.

The in-place substitution energy, one of which is demonstrated in Figure 2.3 (b), shows us that the most favorite substitution sites for  $\langle 001 \rangle$  tilt grain boundaries are always those sites connecting two basic units as drawn in Figure 2. (a). In this circumstance, we can express the substitution energy in Eq. (2-4) as

$$\tilde{E}_{sub} = \frac{\delta\varepsilon}{d_1 + d_2} = \frac{\varepsilon_{1-2} - \varepsilon_1 - \varepsilon_2}{d_1 + d_2} \quad (2-7)$$

The idea behind Eq. (2-7) is taking the all unit 1, unit 2 and the solute atoms in between combined as a new structural unit and taking into account the energy difference between the new unit  $\varepsilon_{1-2}$  and the two basic units, i.e.  $\varepsilon_1$  and  $\varepsilon_2$ . This idea is very straight forward, and can be extended easily to other substitution sites. In the next section, Eq. (2-7) is tested and found to be valid for substitution sites with different energies.

Eq. (2-7) is limited to only a few special substitution sites. To compute substitution energies for arbitrary lattice sites, we propose a threefold expansion method:

1. Compute the grain boundary energy of a pure metal system ( $E_{GB}^{pure}$ ) using the DSUM techniques given in Eq. (2-1).
2. Compute the in-place substitution energy ( $E_i^{ise}$ ) according to Eq. (2-6).
3. Compute the energy change ( $\delta E_i^{el}$ ) during structural relaxation of the in-place substituted lattice using Eq.(2-8).

The energy change measured in step 3 is denoted by  $\delta E_i^{el}$  because it is considered as the elastic contribution to the substitution energy as discussed earlier. In the framework of pair potential, the elastic energy change of the simplest case in which one metal atom at position  $\mathbf{r}_i$  is replaced by a solute atom can be expressed as

$$\begin{aligned} \delta E_i^{el} &\equiv \tilde{E}_{MS}^{tot} - E_{MS}^{tot} \\ &= \sum_{k>j, k\neq i} [\phi(\tilde{\mathbf{r}}_{kj}) - \phi(\mathbf{r}_{kj})] + \sum_{k\neq i} [\psi(\tilde{\mathbf{r}}_{ki}) - \psi(\mathbf{r}_{ki})] \\ &\approx \sum_{k\neq i} [\psi(\tilde{\mathbf{r}}_{ki}) - \psi(\mathbf{r}_{ki})] \\ &\approx - \sum_{k\neq i} \mathbf{F}_{ki} \cdot \delta \mathbf{r}_{ki} \end{aligned} \quad (2-8)$$

where  $\tilde{E}_{MS}^{tot}$  and  $E_{MS}^{tot}$  are the total potential energies of a metal system with one solute atom at position  $\mathbf{r}_i$  before and after structural relaxation, the subscript  $MS$  means that the system contains both metal(M) and solute(S) atoms,  $\phi$  and  $\psi$  are the pairwise potential functions describing metal-metal and metal-solute interactions respectively,  $\mathbf{F}_{ki}$  is the force on atom  $i$  resulting from atom  $k$ , and  $\mathbf{r}_{ki} \equiv \mathbf{r}_k - \mathbf{r}_i$  is the position vector between atoms  $k$  and  $i$ .

The right side of Eq. (2-8) is linked to the virial stress tensor<sup>[61]</sup> in the following fashion:

$$\begin{aligned} \tilde{\sigma}_{MS}^m(\mathbf{r}_i) - \sigma_{MS}^m(\mathbf{r}_i) &= - \sum_{k \neq i} [\tilde{\mathbf{F}}_{ki} \cdot \tilde{\mathbf{r}}_{ki} - \mathbf{F}_{ki} \cdot \mathbf{r}_{ki}] \\ &\approx \delta E_i^{el} + C_{el} \end{aligned} \quad (2-9)$$

In Eq. (2-9),  $\sigma^m \equiv -(\sigma_{xx} + \sigma_{yy} + \sigma_{zz})$  is the mean norm component of the virial stress tensor. In elasticity theory,  $\sigma^m = PV$  where  $P$  is the pressure of a solid body and  $V$  is its volume. Therefore Eq. (2-9) is straightforward from a macroscopic viewpoint:  $\delta E^{el} = \int PdV \approx \delta(PV) - V\delta P$ . In Eq. (2-9), the assumption is made that  $V\delta P$  is less position dependent than is  $\delta E_i^{el}$  and thus can be treated as a constant. This validity of this assumption is confirmed below using fully atomistic simulations.

The reason of relating the elastic energy to the stress field is because in principle energy is not additive but stress field components are. This is an important property for DSUM based methods. It allows us to express the overall stress field of a complex structure as a linear superposition of the stress fields of a few composing units. Mathematically, it is given as

$$\hat{\sigma}_{MS}^m(\mathbf{r}_i) \approx \hat{\sigma}_{MS}^m(\mathbf{r}_i) \equiv \sum_{\mu} \tilde{\sigma}_{\mu,MS}^m(\mathbf{r}_i - \mathbf{r}^{\mu}) \quad (2-10)$$

where  $\mu=1$  or 2 has the same meaning as the subscript used in Eq. (2-1). The hatted symbols differentiate the interpolated values from values determined from molecular simulation.

### 2.3 Experiment

Equations (2-6) and (2-7) yield the most likely substitution sites and give the corresponding grain boundary energies. Eq. (2-9) and (2-10) provide a way to compute substitution energy at arbitrary lattice site. To probe the accuracy of these formulas, thirty  $\langle 001 \rangle$  symmetric tilt angle grain boundary structures have been built and tested; their structural information in terms of basic structural units are listed in Table 2.1.

Simulations of  $\langle 001 \rangle$  tilt grain boundaries in Table 2.1 are carried out using an embedded atom potential for four alloy systems, lead segregated aluminum (Al-Pb), zirconium segregated aluminum (Al-Zr), niobium segregated copper (Cu-Nb) and zirconium segregated copper (Cu-Zr). The EAM calculations are performed LAMMPS, a Sandia-based parallel MD code<sup>[60]</sup>.

In our simulation, three dimensional computational cells of bicrystals with three dimensional periodic boundary conditions consisting of two grains were created utilizing coincident site lattice algorithms. The tilt grain boundary cut each computational cell into two halves, each of which are mirror symmetrical and have a minimum thickness of 15.1 nm.

Table 2.1:  $\langle 100 \rangle$  Symmetric tilt grain boundaries with impurities segregating at the first lowest energy sites; the term “alloy” means the solute induced system. The dash symbol “-” in the *Structure* column is used to denote the site that connects two basic structural units and is substituted by impurity atoms. For instance, an B-C structure is equal to a combination of B+C- structure shown in Figure 2.1 (a).

<b>CSL Notion</b>	<b>Structure</b>	<b>Tilt angle (°)</b>	<b><math>\rho_{impurity}</math> (at%)</b>
$\Sigma 1$ -110	A-A	0.00	0.903
$\Sigma 421$ -15140	AAAAAAAAAAAAA-B	3.95	0.048
$\Sigma 181$ -1090	AAAAAAAAA-B	6.03	0.079
$\Sigma 41$ -540	AAA-B	12.68	0.189
$\Sigma 25$ -430	AA-B	16.26	0.236
$\Sigma 149$ -1070	AA-BA-BA-B	20.02	0.289
$\Sigma 13$ -320	A-B	22.62	0.336
$\Sigma 85$ -1170	A-BA-BA-BB	25.06	0.253
$\Sigma 17$ -530	A-BB	28.07	0.197
$\Sigma 65$ -740	A-BBB	30.51	0.140
$\Sigma 109$ -1370	A-BBBBBB	33.40	0.077
$\Sigma 533$ -29150	A-BBBBBBBBBBBBBB	35.30	0.031
$\Sigma 5$ -210	B-B	36.87	0.272
$\Sigma 353$ -1780	BBBBBBB-C	38.60	0.057
$\Sigma 97$ -940	BBB-C	42.08	0.115
$\Sigma 29$ -730	BB-C	43.60	0.157
$\Sigma 29$ -520	B-C	46.40	0.216
$\Sigma 73$ -830	B-CC	48.89	0.138
$\Sigma 325$ -1760	B-CCCCC	51.11	0.062
$\Sigma 5$ -310	C-C	53.13	0.186
$\Sigma 397$ -1960	CCCCCC-D	54.95	0.051
$\Sigma 109$ -1030	CCC-D	56.60	0.115
$\Sigma 53$ -720	CC-D	58.11	0.158
$\Sigma 17$ -410	C-D	61.93	0.282
$\Sigma 85$ -920	C-DC-DD	64.94	0.264
$\Sigma 13$ -510	C-DD	67.38	0.228
$\Sigma 37$ -610	C-DDD	71.08	0.260
$\Sigma 25$ -710	C-DDDD	73.74	0.168
$\Sigma 101$ -1010	CDDDDDD	78.58	0.111
$\Sigma 1$ -100	D-D	90.00	1.786

The tilt axis is along the  $x$  direction and the normal vector of each grain interface is along the  $z$  axis. Each atomistic model contains a total of between 54648 and 100416 atoms and was fully relaxed using a conjugate gradient energy minimization algorithm. EAM potentials of Al-Zr, Cu-Nb and Cu-Zr systems are taken from the work of Sheng et al<sup>[62][15]</sup>, and that of Al-Pb system is from Landa's work<sup>[63]</sup>. Those are highly optimized EAM potentials designed for simulating alloy structures and mechanical properties at any temperature. It predicts alloy structure in a reasonable agreement with experimental data. At zero temperature, the potentials predict perfect FCC structures whose lattice constants match first principle calculations.

Equilibrium relaxed structures at zero temperature are then found by minimizing the total internal energy with respect to all atomic positions. Further we resize the dimensions of the simulation box to ensure that the total pressure of the block is zero (e.g. no artificial inner stresses are introduced). Grain boundary energies of both pure metal and alloy systems are computed and shown in the Figure 2.2.

Twenty eight  $\langle 001 \rangle$  Cu-Zr grain boundary models with misorientation angles ranging from  $3.95^\circ$  to  $78.58^\circ$ , as listed in Table 2.1, were chosen to evaluate the accuracy of Eq.(2-9) and Eq. (2-10). Overall 500 near grain boundary copper atoms were randomly chosen and replaced by zirconium atoms in these twenty eight models. The substitution energies were then computed as the energy difference between fully relaxed Zr containing models and fully relaxed pure copper systems.

## 2.4 Results and Discussion

Evaluating Eqs.(2-1) -(2-4) requires the energies of basic structural units A, B, C, D and the bonding energies defined in Eq.(2-10). Because the basic units A and D are unit cells of perfect FCC lattice,  $\varepsilon_A = \varepsilon_D = 0 \text{ J} \cdot \text{m}^{-2}$ . The energies of the basic units B and C are determined from EAM results of model  $\Sigma 5 - 210$  and  $\Sigma 5 - 310$  grain boundary structures. We found for the Al-Pb system  $\varepsilon_B^{Al} = 0.443 \text{ J} \cdot \text{m}^{-2}$  and  $\varepsilon_C^{Al} = 0.451 \text{ J} \cdot \text{m}^{-2}$ . Those values are a little different for Al-Zr system,  $\varepsilon_B^{Al} = 0.489 \text{ J} \cdot \text{m}^{-2}$  and  $\varepsilon_C^{Al} = 0.487 \text{ J} \cdot \text{m}^{-2}$ . In principle these values should be equal since they all are computed from pure aluminum systems. However the disparity is understandable because they are calculated based with different EAM potentials. Similarly, in pure copper, the energies of the basic units are  $\varepsilon_B^{Cu} = 0.862 \text{ J} \cdot \text{m}^{-2}$ ,  $\varepsilon_C^{Cu} = 0.830 \text{ J} \cdot \text{m}^{-2}$  for the Cu-Nb system and  $\varepsilon_B^{Cu} = 0.834 \text{ J} \cdot \text{m}^{-2}$ ,  $\varepsilon_C^{Cu} = 0.807 \text{ J} \cdot \text{m}^{-2}$  for the Cu-Zr system, respectively.

According to Eq. (2-4) both grain boundary energies of pure metal systems and impurity induced systems are calculated using EAM potentials; bond energies are then found as the difference of the two according to Eq. (2-10). Because the bond energies are most likely negative, they are the reason why grain boundaries are stabilized after solute atoms been introduced, they are also called the stabilization energy in the following text.

Table 2.2: Observed disclination dipole strengths of fully relaxed atomistic structures.

	Al – Pb	Cu - Nb	Al -Zr	Cu - Zr	Theoretical
$\omega_{AB}$	35.2	35.3	36.8	36.8	36.9
$\omega_{BC}$	15.4	17.2	17.2	18.1	16.3
$\omega_{CD}$	39.4	42.0	39.8	42.3	36.9

In our calculation, the disclination diopole strengths, i.e.  $\omega$  in Eqs (2-1) and (3-9), were measured from fully relaxed atomistic models instead of the ideal values. In particular, it was found that  $\omega_{CD}$  values are constantly greater than what we would expect from the ideal  $C - D$  disclination diopole. For example, the observed value of  $\omega_{CD}$  is  $44.12^\circ$  for the  $\Sigma 13 - 510$  structure instead of  $36.87^\circ$  predicted by CSL theory. We measured disclination angle differences for all those grain boundary structures that have  $C - D$  disclination diopoles and took the average value as the input parameter, i.e.  $\omega_{CD}$ , in Eqs (2-1) and (3-9). Following this procedure we measured the diopole strengths of different structural units for all four alloy systems and list the values in Table 2.2. From Table 2.2, we can see that the actual  $\omega_{AB}$  and  $\omega_{BC}$  values are approximately equal to the ideal values, while  $\omega_{CD}$  values are clearly greater. We believe that the degree to which the grain boundary structure resembles the dislocation wall model plays an essential role here. As illustrated in Figure 2.1- (b), the actual basic unit C structure differs widely from the uniformly distributed dislocation wall model, which is the assumed in Eqs (2-1) and (3-9). Instead, constrained by geometries, the two dislocations inside C are pushed aside by the middle atom and piled up at the bottom of the unit. This pile up gives the  $C - D$  diopole a larger value of  $\omega$ . This modification to diopole strengths has a pronounced effect on DSUM predictions. As shown in Figure 2.1-(c), using unrealistic  $\omega$  values for  $C - D$  diopoles underestimates the grain boundary energy of copper in the high tilt angle region. The difference is the energy needed to pile up the two dislocations.

Figure 2.2 summarizes the misorientation angle dependences of grain boundary energies of both pure metal systems and alloy systems determined from atomistic calculations and the disclination units model. Results from DSUM theory match what we

would expect to see from EAM calculations at almost all tilt angles. Similar results have been obtained for many pure metal systems over the past decades <sup>[25], [27], [28]</sup>.

Stabilization effects are clearly demonstrated in Figure 2.2, in which the doped structures give lower grain boundary energies than that of dilute solutions in pure metal structures. The grain boundary energy of the doped system at tilt angle of  $0^\circ$  and  $90^\circ$  are hypothetical since these two structures are grain-boundary-free lattices. In our calculation we hypothetically chose (110) and (100) as grain boundary planes. To compare results of hypothetical grain boundaries to normal ones, we artificially choose those doped sites that lie on (110) and (100) planes whereas doped sites in defect-free lattice should be distributed homogeneously among the lattice in the dilute solution limit.

A notable result from Figure 2.2 is that grain boundary energies of some doped structures are negative for some structures, for example the  $\Sigma 13 - 320$  and  $\Sigma 17 - 410$  interfaces in Cu-Zr and Al-Pb systems. In the case of dilute solute systems, a negative grain energy means that the grain boundary structure is more stable than the perfect lattice structure. If an alloy of such material is recovered from work hardening, grains enclosed by negative energy grain boundaries are not driven to grow because the energy change of removing those grain boundaries is positive.

Figure 2.3 shows the stabilization effects, it can be seen from (a) that bond energy relations of Cu-Nb, Al-Zr and Cu-Zr systems are almost parallel. This indicates that the stabilization mechanisms of all the three systems are the same. We believe that the stabilization energy arises from the interaction of the grain boundary stress field and the volume misfit stress field due to impurity substitution. If we define an parameter such as

lattice constant difference  $\delta a_{IM} = |a_I - a_M|$ , where  $a_I$  ( $a_M$ ) is the lattice constant of the solute (matrix) material, we can draw the phenomenological conclusion from Figure 2.3 that the stabilization energy is negatively correlated to  $\delta a_{IM}$ . For example, zirconium has a more prominent stabilizing effect to copper than niobium. This is because  $a_{Zr-Cu} \approx 0.38\text{\AA} > \delta a_{Cu-Nb} \approx 0.31\text{\AA}$ . This empirical conclusion is reasonable, because the volume misfit effect grows as the lattice constant difference increases.

Figure 2.3-(c) and (d) demonstrates how grain boundary energy changes with area density of impurities. The lines in (c) are not smooth, and taking Cu – Nb system as an example, there are five linear segments in the blue line. Each stage corresponds to a doping level. As concentration of Nb in Cu is gradually increased, impurities tend to sit on those sites with lowest substitutional energies. In the meantime, it is apparent from Figure 2.3-(b) that there are many sites with similar energies in a grain boundary model. We therefore call this stage 1<sup>st</sup> doping level region in which substitution happens only at energy favorites sites.

We call the grain boundary energy values at the minimum points in Figure 2.3 as the “optimized grain boundary energy”, and the concentration at these points as the “optimized impurity concentration”. We can conclude that optimized grain boundary energy decreases and corresponding impurity concentration grows with increasing tilt angle. This conclusion is not always true, but it is general for those grain boundaries that are made of A-B units. The latter is easy to understand, because the energy change of introducing one impurity into the grain boundary is bounded, and that optimized energy of high angle grain boundaries is lower, more substituting impurities are therefore needed to achieve that optimum grain boundary energy. The reason why the high angle grain boundary has a

smaller optimized grain boundary energy is not straightforward. Considering that the unit A does not bring any defect into the structure, but B does. As the tile angle increases, the proportion of B units also increases, and thus more defects are introduced, and the interaction between defects and grain boundary are then increased accordingly because the total stress field is also increasing.

## 2.5 Conclusion

In this chapter, several efficient computational methods were presented to study the stability of alloy systems. First, a formula based on the perturbation of EAM potentials was derived and implemented in LAMMPS to compute the in-place substitution energy for all lattice sites for all atom models. This algorithm is  $O(N^2)$  in time compared to  $O(M \times N^2)$  of conventional methods if  $N$  lattice sites are present and  $M$  substitution sites are considered. Second, for grain boundaries with solute segregated at favorite segregation sites or the second to most likely segregate lattice sites, a formula based on DSUM techniques was proposed to compute the corresponding grain boundary energies. Because the DSUM is a macroscopic model and has analytical expression for grain boundary energies, its complexity in time can be considered as  $O(1)$ . In contrast, computing corresponding grain boundary energies with molecular dynamics requires at least  $O(N \log N)$  computation time, not to mention the formidable tasks of building full atomistic models for every grain boundary investigated. Third, we constructed a three-fold method to compute substitution energy for every lattice site with expansion techniques. Compared to the conventional way of computing substitution energies which is  $O(M \times N^2 \times T)$  in time with  $T$  the average number

of molecular dynamics steps for potential energy minimization, this method is  $O(N^2)$  in time and therefore can save enormous computation effort since it allows us to compute the segregation energy at arbitrary lattice sites without performing structural relaxation or doing solute substitution one at a time. All three proposed methods have been tested with satisfactory accuracy for various alloy systems.

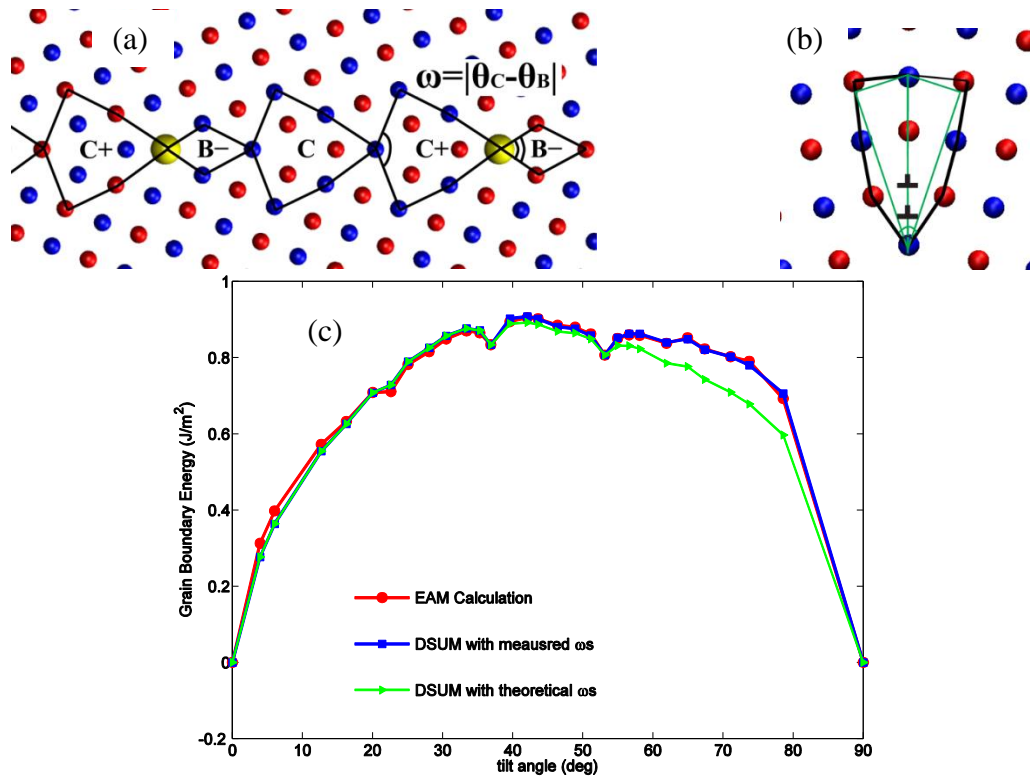


Figure 2.1: (a) Structural units model of FCC  $\langle 100 \rangle\text{-}\Sigma 73\text{-}830$  grain boundary. Impurity atoms, which are represented by bigger yellow spheres, segregate on the first lowest energy sites. The blue and red spheres denote the copper atoms that lie on (002) and (001) planes respectively. Those structures whose head (tail) atom is replaced are marked as positive (negative) structure. (b) Illustration of theoretical (inside green shape) and actual (outside black shape) C structure. Two dislocations pile up at the bottom of C unit. (c) Illustration how disclination dipole strength affects the DSUM results, the red dot line is the grain boundary energy of Copper calculated from atomistic models. The blue rectangle line and the green triangle line are DSUM predictions with and without dipole strength modification respectively.

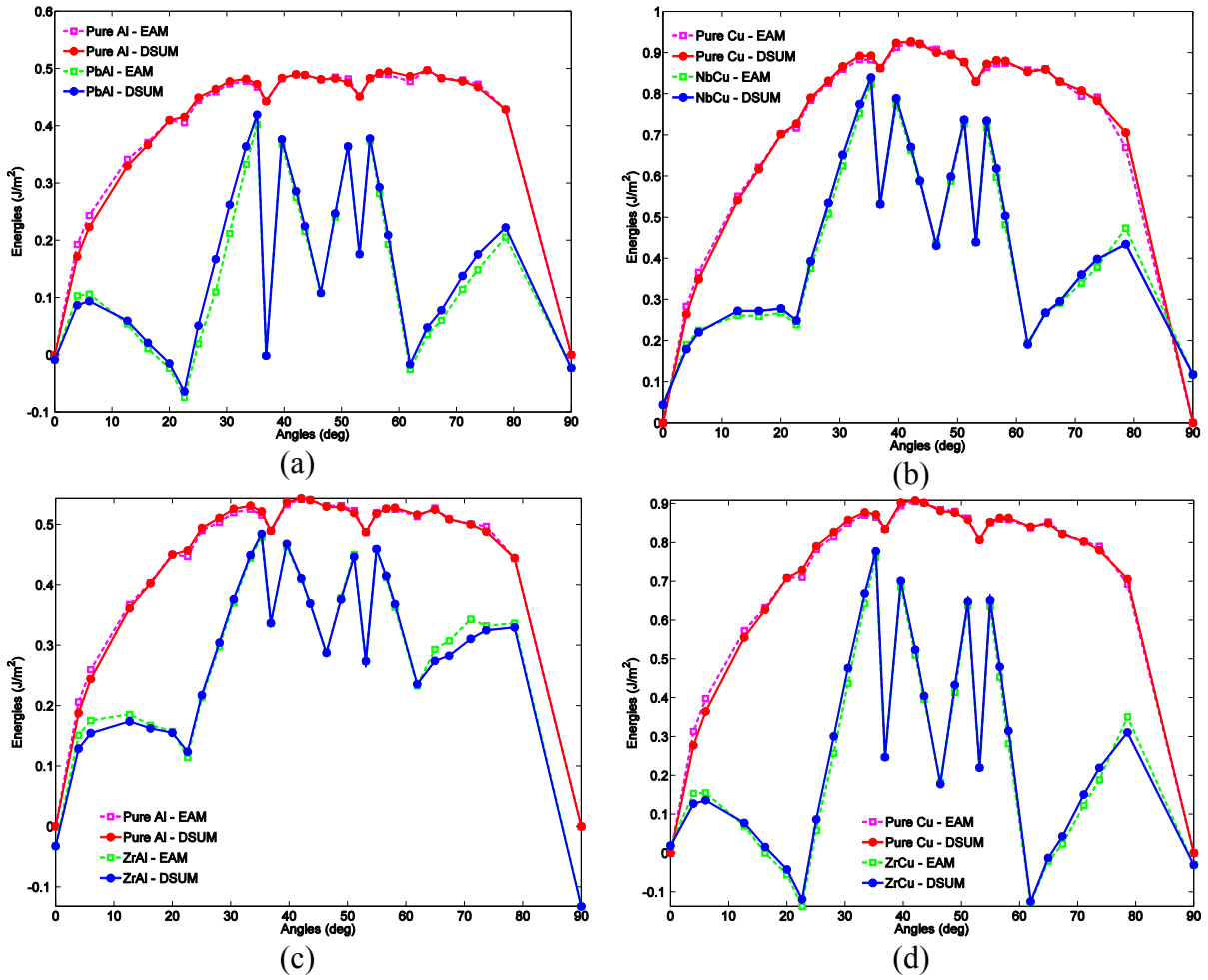


Figure 2.2: Dependence of energies of (100) symmetric tilt grain boundaries on the tilt angle for four systems. Respectively: (a) Pb doped Al; (b) Nb doped Cu; (c) Zr doped Zr and (d) Zr doped Cu systems. The rectangle lines are computed directly from atomistic models with EAM potential, the solid circle lines are obtained from DSUM model. The red and purple lines correspond to pure metal system, the blue and green lines represent grain boundary energy of solute induced systems.

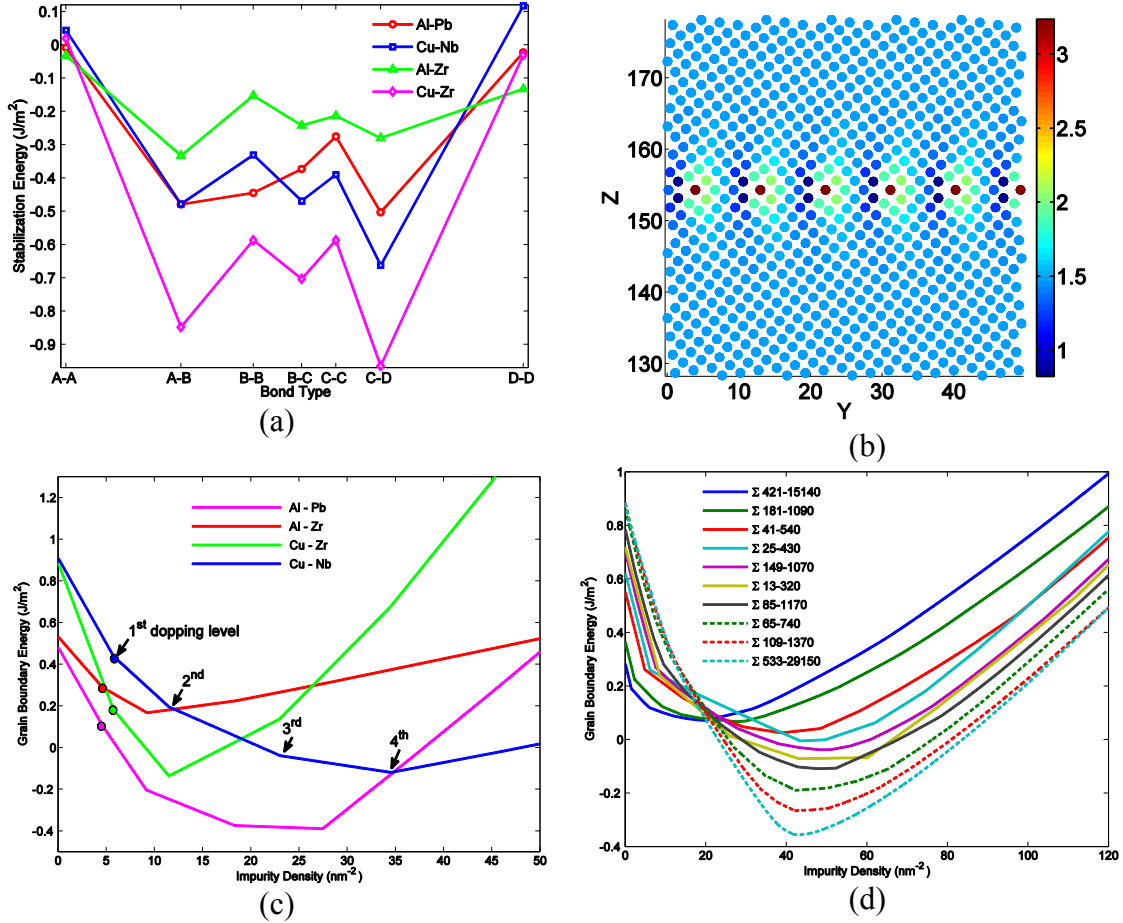


Figure 2.3: Stabilization effects shown by (a) Energies of different bond types of four alloy systems; (b) energy change of substituting a copper atom for a zirconium atom at different sites in the  $\Sigma 17-530$  grain boundary. (c/d) Dependence of grain boundary energy on area density of impurities in different alloy systems / with different tilt angles.

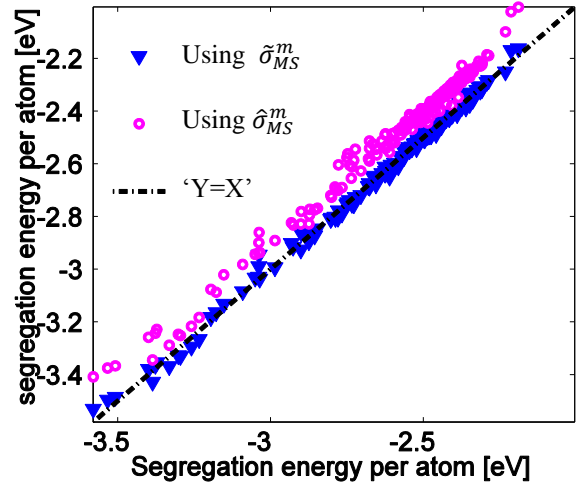


Figure 2.4: Comparison between expansion obtained and full calculations of segregation energies for Cu-Zr alloy. Values denoted by triangles are obtained from Eq. (2-9) only, and the circles are computed under the approximation of Eq. (2-10). Data with circle are elevated by  $0.1 \text{ eV}$  intentionally so that two sets of data are distinguishable.

## Chapter 3 Studying Motion of $\langle 100 \rangle$ Tilt Grain Boundaries Using Molecular Dynamics

### Simulation

In the study of grain boundary migration of metallic materials using molecular dynamics simulation, grain boundary mobilities and activation energies are often found to be different from experimentally observed values. To reconcile the discrepancies, tremendous effort has been made to replicate experimental conditions in molecular dynamics simulations, e.g. as low a driving force as possible, near zero grain boundary velocity. In the present study, we propose an analytic method that removes effects from non-physical conditions such as high driving force or high temperature. The analytic model presumes that two types of rate limiting events coexist during grain boundary migration. Kinetics parameters, such as activation energies, of these events are different and therefore should be modeled separately. Activation energies from this model are closer to experiment than previously reported values. Further, by analyzing the evolution of atomic structures, these two types of rate limiting events correspond to shear coupled migration and grain boundary sliding mechanisms.

### 3.1 Introduction

Molecular dynamics simulations (MDSs) have been used to model the dynamic behavior of grain boundaries (GBs). However, despite continuous efforts in this area during the past decades<sup>[42], [44]–[46], [64]–[67]</sup>, our ability to simulate GB motion and to predict microstructure evolution from these simulations is still lacking. In principle, MDS with embedded atom method (EAM) potentials can provide a relatively accurate description of the

atomistic energy of metal systems. However, GB properties such as GB mobilities and activation energies predicted by MDS are often different from experimentally measured values. To reconcile the discrepancies between molecular dynamics simulation and experiments, methods have been developed that are intended to make experimental conditions such as grain boundary velocity of  $10^{-8}$  m/s and driving force about  $10^{-2}$  MPa accessible to MDS [36], [48]. Published in 2006, Janssens *et al.* proposed an orientation dependent driving force method to study GB migration in f.c.c. aluminum bicrystals. They used a driving force in their work of 0.025 eV per atom or 244 MPa on the interfaces at a simulation temperature of 800 K ( $\sim 0.8T_m$ ). Despite the driving force being several orders of magnitude higher than the driving force used in experiments, some boundaries, including all of the  $\langle 111 \rangle$  twist boundaries, were found to be immobile with this method. Soon after this work, Zhou and Mohles [65] claimed that the driving force used in the above mentioned work was too large, and that boundary migration velocity and driving force are nonlinear. To obtain a GB velocity at the limit of a zero driving force, they computed a series of GB velocities under different driving force conditions and then extrapolated the velocity-driving force curve to obtain GB mobility at a zero driving force. However, Zhou and Mohles' work still requires an elevated temperature and driving force (so that the GBs are mobile). In related work by Trautt *et al.* [45], GBs in a bicrystal were treated as a one dimensional random walking particle so that the GB mobility is linearly proportional to its position fluctuation in a MDS. Different from the driving force methods, this random walk method requires MDS at an equilibrium condition with zero driving. However, it still requires a high temperature,  $0.9T_m$ , to create sufficient fluctuations for a meaningful statistical analysis. Recent work by

Deng and Schuh improved the statistical method of the original random walk method by applying a small driving force as a bias. By comparing the boundary fluctuation before and after applying the bias, they were able to compute the GB mobility and activation energy at a low temperature,  $\sim 0.2 T_m$  with mild driving force 0.01 eV ( $\sim 100$ MPa).

Reaching the limits of low driving force and low temperature is the common goal in MDS studies of GB migration with the goal of MDS replicating experimental results when the limits are reached. In many publications, the authors indicate that the discrepancy between MDS results and experimental values arise from either elevated temperature or high driving force. For instance, Trautt et al<sup>[45]</sup> asserted that GB mobilities are sensitive to the driving force and implied that the driving force methods underestimate GB mobilities. Furthermore, Deng and Schuh suggested that<sup>[68]</sup> that the different driving forces not only lead to different mobility but may also leads to different GB migration mechanisms. More specifically, they concluded that, “grain boundary motion is diffusional” at low driving force and low temperature limit while “*grain boundary migration exhibits the characteristic kinetic scaling behavior of a ballistic process*” under conditions of high driving force and high temperature.

In many aspects, results from MDS with mild conditions are more convincing, although this has been disputed. In a review paper by Mishin et al<sup>[69]</sup>, for example, the authors reviewed many publications and concluded that “*the GB mobilities extracted from the simulations, no matter which method was applied, are consistently higher than experimental mobilities*”. Furthermore, the activation energies of GB migration always underestimate the experimental values, sometimes by as much as an order of magnitude”.

Another study by Mendeleev et al <sup>[70]</sup> carefully compared the MDS results from different methods and concluded that both the GB mobility and activation energy are independent of the nature of the driving force.

In this chapter, we propose an analytic method that can reconcile the differences between MDS and experiments. By studying the migration mechanisms of symmetric tilt grain boundaries (STGB), we concluded that more than one rate limiting process coexists during GBM. These processes were categorized into two classes, corresponding to coupled shear and GB sliding by conventional definition. An analytical expression that incorporates two rate constants is then proposed to interpret the temperature dependence of GB mobility. Activation energies resulting from our model are then compared to experimental values to validate our theory. This chapter concludes with a discussion regarding why micro-mechanisms affect the MDS and leads to divergent results under different MDS conditions.

### **3.2 Direct MDS with Pure Metal Systems**

A total of 28  $\langle 100 \rangle$  symmetric tilt angle grain boundaries of f.c.c. copper with tilt angles varying from  $3.95^\circ$  to  $78.58^\circ$  were created in three-dimensional periodic computational cells. All GBs were carefully constructed according to coincident lattice theory so that the  $\Sigma$  is as small as possible. Each computational cell accommodates a total number of 54648 to 100416 atoms. The tilt grain boundary cut each computational cell into two exact halves, each of which are mirror symmetrical and have a minimum thickness of 15.1 nm. The tilt axis is along x direction and the normal vector of each grain interface is along the z axis. Each atomistic model was fully relaxed using a conjugate gradient energy

minimization algorithm. Simulation boxes defining the periodic boundaries were also resized to ensure that the total pressure of the block is zero so that no artificial inner stresses are introduced. Grain boundary energies of all 28 microstructures were computed as a reference to which both GB mobilities and GB activation energies can compare. An EAM potential from Sheng<sup>[62]</sup> for pure copper was used in both energy minimization and MDS of GBM. It is a highly optimized EAM potential designed for simulation of crystal structure and mechanical properties at any temperature. It is able to produce accurate matches with experiments, such as elastic constants, vacancy formation energy, stacking fault energy, and melting temperature.

GB motion simulations were performed for all 28 GBs using the orientation-dependent driving force method developed by Janssens et al<sup>[42]</sup>. Specifically, the potential energy of atoms in one grain are elevated by a value of  $\Delta E$ . Because of the energy difference on the two sides of a GB interface, atoms with an elevated potential energy are driven to move towards the GB interfaces and finally merge with atoms in the other grain so that overall energy of the system can be lowered. In all our simulations, a driving force of 0.1 eV, which equals to about 340MPa, was used. Temperature was controlled in all of the simulations using the Nose-Hoover thermostat as suggested in Janssens's paper<sup>[42]</sup>. To study the tilt angle dependence of activation energies, we collected MDS trajectories in three parameter space: misorientation angle  $\theta$ , temperature T and independent sample index  $v$ .  $r^{3N}(t; \theta, T, v)$  where temperature ranges from 800K to 1150K with a uniform step size of 50K. This sample index means that for each tilt angle GB and each temperature, 12 independent MDS trajectories with randomized initial atom velocities were generated to

produce an ensemble average of GBM. A total number of  $28 \times 8 \times 12 = 2688$  MDS trajectories were collected and analyzed.

For each MDS trajectory, GB position  $z_{gb}(t; \theta, T, v)$  was determined from the maximum in the centro-symmetry parameter profile in the z-direction (the z axis is normal to the GB plane). GB velocity was calculated from the slope of the ensemble averaged GB position line. Mobility was then calculated as  $m_{gb}(\theta, T) = v_{gb}(\theta, T)/P$ , where  $P=340\text{MPa}$  as mentioned above. Finally the activation energies were computed from fitting mobilities to an Arrhenius equation through an Arrhenius plot of the form

$$\ln[m_{gb}(\theta, T)] = -\frac{E_a(\theta)}{kT} + \ln A \quad (3-1)$$

### 3.3 Mobility Calculation with Transition Path Sampling Method

Transition path sampling (TPS) is a set of rare event sampling methods in trajectory space. Rare events in computer simulations are the events that rarely occur but proceed quickly when they occur. GBM is one such example. According to a study of the shear coupled migration of a symmetrical tilt angle GB in copper by Rajabzadeh *et al*<sup>[71]</sup>, the energy landscape along the GB motion path is not flat. A metastable transition state presents between two stable states. Similar results (Figure 4.2) are also obtained from our study of GB sliding events. The energy barriers along the GB motion path make the barrier crossing events the migration rate limiting events. Therefore, according to the TPS theory, the transition rate, and hence the grain boundary mobility, can be obtained from the time correlation functions of configurations in trajectory space.

To apply the TPS method to the GB migration problem, we first define a “reaction” for GB migration as



where A and B are two stable configuration along the migration coordinate. As shown in Figure 3.1, suppose a STGB in the bicrystal finds three consecutive stable states, state A, B and C, respectively. According to Figure 4.2 and our priori knowledge<sup>[71]</sup> we know that there must be unstable transition states that reside in between each two stable states.

In a typical transition path calculation, a number of dynamic paths of length  $t$  are collected as ordered configurations sequences:  $z(t) \equiv \{z_0, z, z_{2\Delta t} \dots, z_t\}$ . According to transition state theory, the reaction rate constant for Eq. (3-9) is directly related to the time correlation function

$$C_{AB}(t) = \frac{\langle h_A(z_0)h_B(z) \rangle}{\langle h_A(z_0) \rangle} \approx k_{A \rightarrow B} \cdot t \quad (3-3)$$

where the  $\langle \dots \rangle$  denotes the ensemble average,  $h_A(z_0)$  and  $h_B(z_t)$  are the histogram of grain boundaries at position A at time  $t=0$ , and position B at time  $t$ , respectively. Eq. (3-9) measures the probability of finding a grain boundary at position B at time  $t$  given that it initially was at A.

To link the reaction constant  $k_{A \rightarrow B}$  to the mobility, a theoretical model for grain boundary mobilities is needed. Of many candidates<sup>[54]</sup>, we choose the standard model that can be found in many text books. For instance, in the book by Gottstein and Shvindlerman<sup>[41]</sup>, grain boundary mobility is modeled by atom jumping across the grain boundary under the driving force  $P$ .

$$v_{gb} = ve^{-\frac{E_a}{kT}} \cdot \left[ 1 - e^{-\frac{PA_{gb}(z_B - z_A)}{kT}} \right] \cdot (z_B - z_A) \quad (3-4)$$

where  $z_A$  and  $z_B$  are the GB coordinates (in our calculation, it is along the z axis) at A and B,  $E_a$  is the energy barrier height, or the activation energy between A and B, and  $A_{gb}$  is the total area of the GB. In addition, according to transition theory:

$$k_{A \rightarrow B} = ve^{-\frac{E_a}{kT}} \quad (3-5)$$

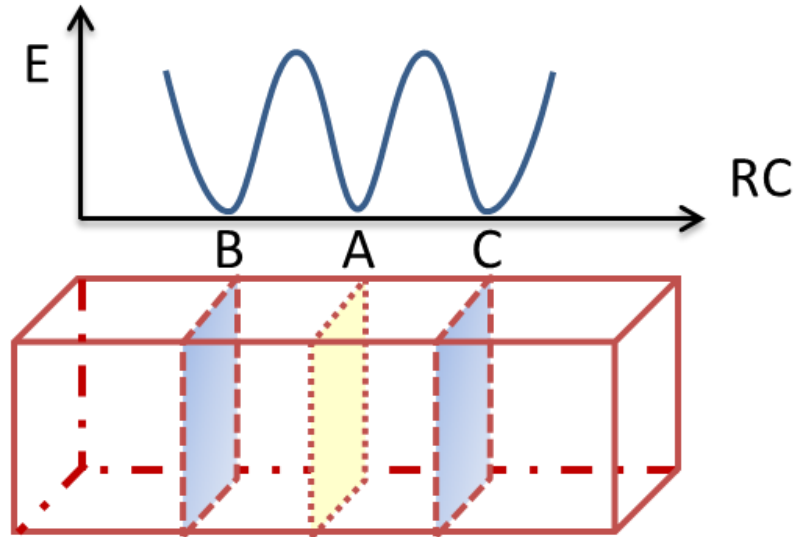


Figure 3.1: Demonstration of three stable states (A, B, C) during a simulation of grain boundary migration. State A is the initial state during the TPS calculation and the reaction coordinate is defined as the position of the grain boundary.

Combining Eqs. (3-9), (3-4) and (3-9) gives the expression for mobility

$$\mu_{gb} \equiv \frac{v_{gb}}{P} = k_{A \rightarrow B} \cdot \frac{A_{gb} \delta z^2}{kT} \quad (3-6)$$

where  $\delta z = z_B - z_A$  is the distance the GB moves when it successfully overcomes the energy barrier between state A and B.

## 3.4 Results

### 3.4.1 Direct MDS with Driving Force

Mobilities at 800K and activation energies are summarized and shown in Figure 3.2. The first non-zero mobility is from  $\Sigma 41-540$  whose tilt angle is  $12.68^\circ$ . Two GBs with smaller tilt angles of  $3.95^\circ$  ( $\Sigma 421-15140$ ) and  $6.03^\circ$  ( $\Sigma 181-1090$ ) are zero. Those zero values are not the true values for the two GBs, but only because the two GBs are immobile under a driving force of 340 at any temperature from 800K to 1150K. This agrees with experiments in that there is a significant drop in GB mobility from the high- to low angle regime<sup>[36]</sup>, and the transition angle for  $\langle 100 \rangle$  tilt GBs is believed to be around  $8.6^\circ$  for all f.c.c metals<sup>[48]</sup>. Due to a lack of experiment data in copper, we are not able to tell the correctness of our data. However, by comparing our results to mobilities listed in ref<sup>[45]</sup>, we conclude that our mobilities are on the same order as past reported data.

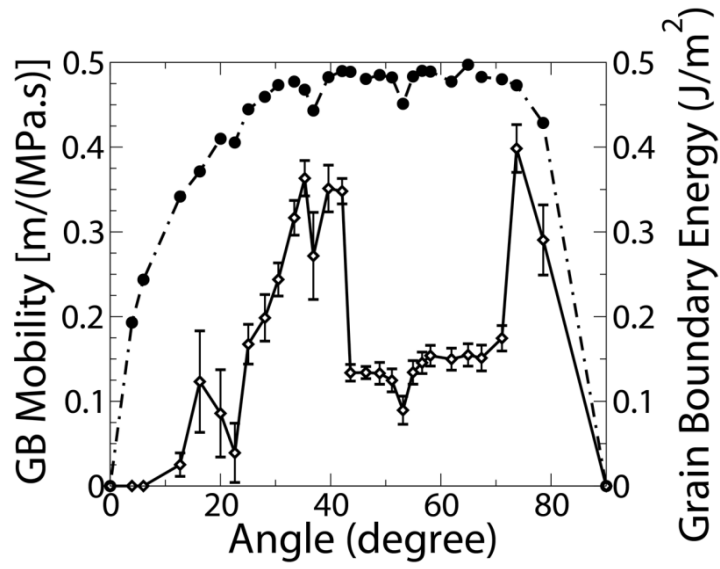
As for the activation energies, data for GBs with tilt angles below  $22.62^\circ$  are missing because the temperature dependence of GB mobility for those small angle GBs do not follow the Arrhenius equation very well. This may be attributed to non-activated GBM mechanisms in certain temperature regions. Similar behavior was also reported in ref<sup>[35]</sup>. From Figure 3.2, we can see that activation energies of GBM for most tilt angles are very small ( $<0.4\text{eV}$ )

compared to experimental values. For instance, the average activation energy for GBs with tilt angles in the range from 36.87° ( $\Sigma 5$ -210) to 53.13° ( $\Sigma 5$ -310) is 0.12eV which is smaller by a factor of 6 - 7 than 0.81eV, the activation energy measured experimentally in ultra-fine grain copper systems<sup>[72]</sup>. We believe that the discrepancy arises from a misinterpretation of mobility data.

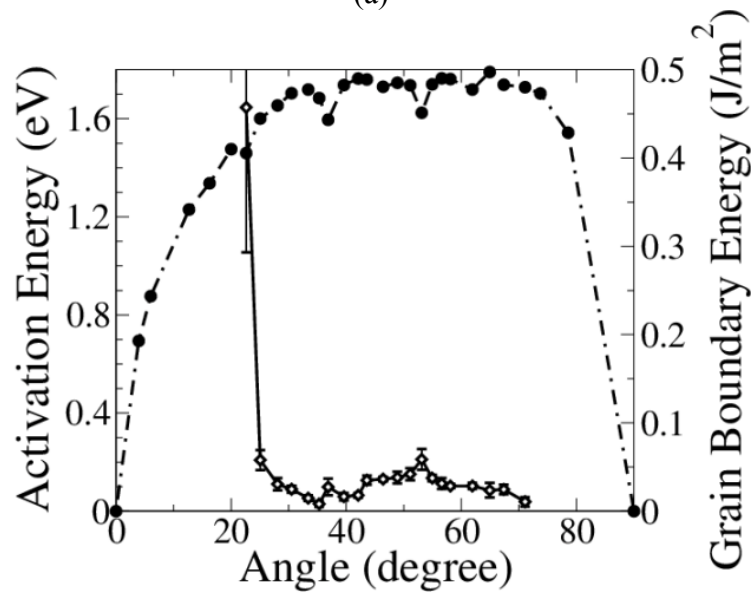
Conventionally grain boundary motion is considered a single rate limiting process, given that the energy barrier of the kinetics is  $E_a$ . Suppose that a short distance of  $\delta z$  is gained when the rate limiting event happens; grain boundary motion can then be modeled as

$$v_{gb} = \frac{dz_{gb}}{dt} = \frac{\delta z \cdot k \cdot dt}{dt} = \delta z \cdot A e^{-\frac{E_a}{kT}}$$

This equation has been validated for many cases and was used to derive GBM activation energies for all publications mentioned in the introduction section. This model has one caveat, however: it relies upon the assumption that there is only one GBM mechanisms during a MDS of GBM.



(a)



(b)

Figure 3.2: Tilt angle dependence of (a): Mobilities at 800K and (b): corresponding activation energies for STGBs of copper as listed in the Table 2.1. The dashed dots are the stationary GB energies as reported in Figure 2.2.

To probe the micro mechanisms during GBM, we examined the GBM trajectory of a  $\Sigma 17-530$  structure by calculating the displacement of each atom at the end of trajectory with respect to their initial positions. The y-component of displacements as well as the initial and final positions of all atoms are plotted in Figure 3.3. Two micro-mechanisms are apparent from the displacement plot. Displacements of atoms at the two ends ( $z < 20 \text{ \AA}$  or  $z > 130 \text{ \AA}$ ) distribute linearly along the z axis. The lines correspond to shear coupled GBM through which GBM distance is linearly proportional to shear strain<sup>[51]</sup> parallel to the GB plane. Shear coupled mechanisms happen throughout the GBM, as indicated by the linear part in the sawtooth wave line plot in Figure 3.3. Another noticeable mechanism occurs at jumps between every two linear segments. These jumps represent the GB sliding events as discussed in ref<sup>[35], [51]</sup>. Generally it is believed that both mechanisms coexist during GBM, but GB sliding events have a much higher energy barrier and may be overshadowed by fast shear mechanisms when they are available<sup>[35]</sup>. On the other hand, shear coupled GBM accumulates lateral translation as it proceeds. In many experiments where a large size of GB sample is used, the lateral translation may be prohibited or limited.

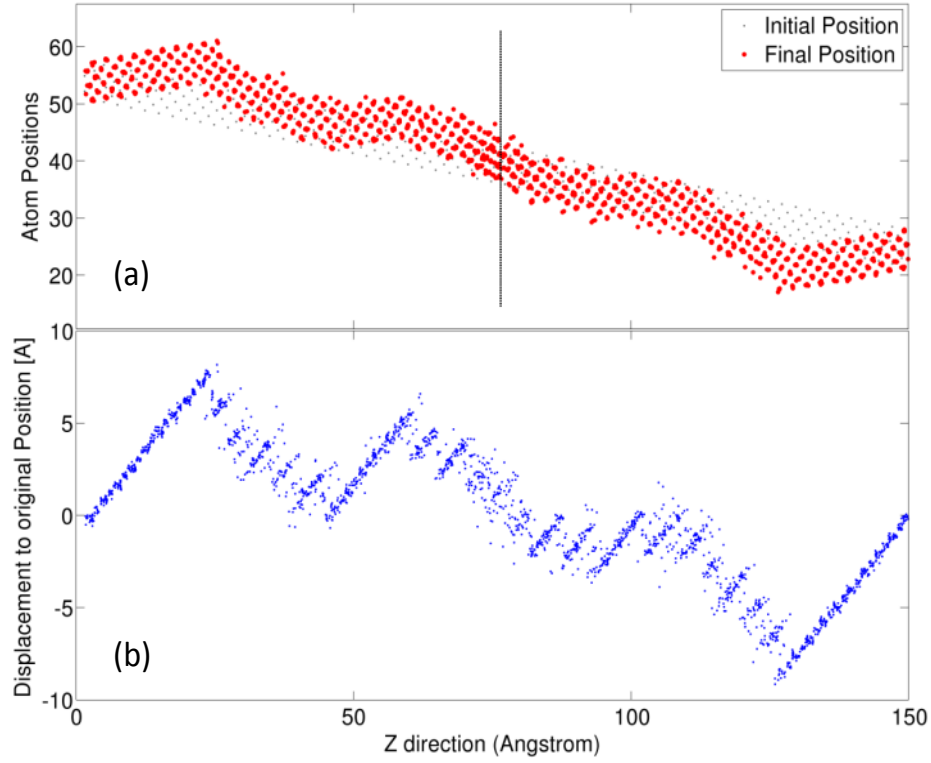


Figure 3.3: (a), initial and final position of atoms in  $\Sigma 17-530$  STGB, (b) y-component of displacement profile of atoms in (a) along z-direction.

To incorporate both mechanisms in GBM, we propose the following formula:

$$m_{gb}(\theta, T) = m_1 e^{-\frac{Ea_1(\theta)}{kT}} + m_2 e^{-\frac{Ea_2(\theta)}{kT}} \quad (3-7)$$

This formula arises from the assumption that GB moves by two major mechanisms, where each has an energy barrier of  $Ea_1$  and  $Ea_2$  respectively. A distance of  $\delta z_1$  or  $\delta z_2$  is gained when event “1” or event “2” happens so that

$$\begin{aligned} v_{gb} &= \frac{dz_{gb}}{dt} = \delta z_1 \cdot k_1 + \delta z_2 \cdot k_2 \\ &= \delta z_1 \cdot A_1 e^{-\frac{Ea_1}{kT}} + \delta z_2 \cdot A_2 e^{-\frac{Ea_2}{kT}} \end{aligned} \quad (3-8)$$

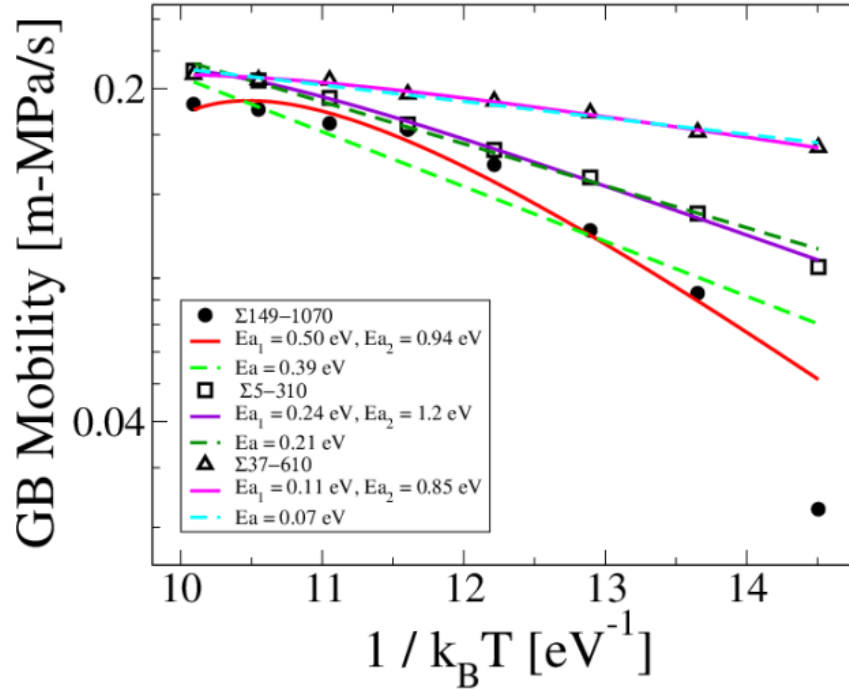


Figure 3.4: Demonstration of activation energies computed by fitting temperature dependent GB mobility to different equations. The symbols are ensemble averaged MDS results, dashed lines are the fits using Eq. (3-1) and solid lines are the fits according to Eq. (3-7)

Mobilities of three GBs were fit to Eq. (3-7) and the results are summarized in Figure 3.4.

The activation energies of GBM for these three GB systems are now comparable to experimental values. For instance, the two activation energies for the  $\Sigma 5-310$  GB are 0.24 eV and 1.2 eV respectively. Judging from the absolute values, we infer that GB sliding has an activation energy of 1.2 eV and the energy barrier for shear coupled GBM is about 0.24 eV. This conjecture is consistent with a recently published paper in which the energy barrier for the  $\Sigma 13-320$  STGB through shear coupled mechanism is 0.283 eV. In addition, the value of

1.2 eV for GB sliding is also reasonable. Considering that GB sliding is accomplished through atom diffusion along the GB, the activation energy should be comparable to the activation energy of self-diffusion along grain boundaries. According to ref <sup>[73]</sup>, this value is 107kJ/mol, or 1.11eV for diffusion along stationary GBs in coarse grained copper.

The reason why Eq. (3-7) works better than Eq. (2-7) is because the two mechanisms are actually competing processes during GBM. Taking the numeric fitting of data for the  $\Sigma 13$ -320 STGB to Eq. (3-7) as an example, the pre-exponents are  $m_1 = 2.64$  and  $m_2 = -7840$ . According to Eq. (3-8),  $m_2$  being negative indicates that each time sliding occurs, the GB moves backward, i.e.  $\delta z_2 < 0$ . This is also shown clearly in Figure 3.3 where the linear segments overlap each other and each time a jump happens, the GB moves from one end of a linear segment to the next one by moving back a little. When a single Arrhenius term equation is used to model the temperature dependence of GB mobilities, the competing effects are averaged out and the displayed activation energy is smaller than the activation energy of either mechanisms.

### 3.4.1 Transition Path Sample Calculations

The fact that more than one mechanism is involved during GBM makes MDS of GBM complicated. In this case, the TPS method, *i.e.* Eq. (3-9), which concerns only one type of event becomes very useful. To illustrate this, we applied the TPS method to the  $\Sigma 17$ -530 STGB with MDS.

As shown in the Figure 3.5, the temporal evolution of  $C_{AB}$  extracted from the TPS method is linear as predicted in Eq. (3-3) and the mobility yielded therefrom is  $18 \text{ m MPa}^{-1} \text{ s}^{-1}$

<sup>1</sup>, or equivalently  $1.8 \times 10^{-8} \text{ m}^4 \text{ J}^{-1} \text{ s}^{-1}$ . This result is consistent with previous calculations<sup>[45]</sup> but one magnitude larger than the mobility computed from direct MDS as shown in the Figure 3.2. This result indicates that both the GBM events captured in our TPS calculation and the GBM modeled by interface random walk method<sup>[45]</sup> follow the same mechanism, i.e. shear coupled mechanism.

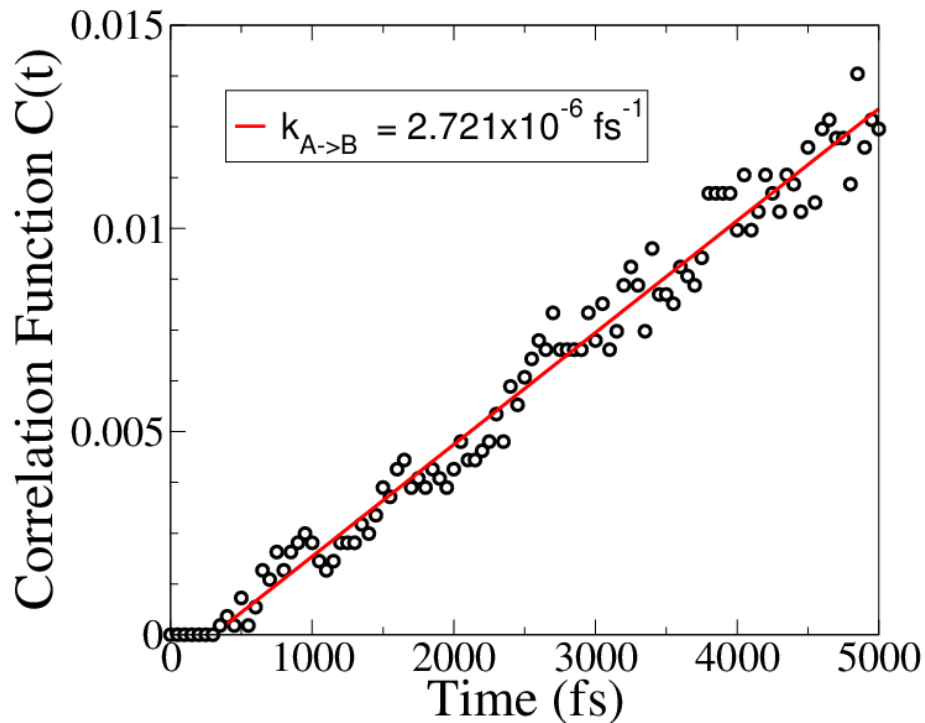


Figure 3.5: Correlation function and its linear fit for the  $\Sigma 17$ -530 STGB at 600K.

Our TPS calculation bears many similarities to the random walk method on the theory level: (i) Neither of them requires a driving force, unlike the synthetic driving force

method<sup>[42]</sup>. (ii) Both of them work well at low temperature. For example, our calculation is done at 600 K while the minimum temperature used in Figure 3.2b is 800K. (iii) Both of them compute the correlation functions. The TPS method calculates the correlation of being at state A and being at state B (as shown in the Figure 3.6). The random walk method calculates the correlation of GB positions. If the transition from A to C is also taken into account, and if we define a new variable as

$$D \equiv \delta z^2 (C_{AB} + C_{AC}) / t \quad (3-9)$$

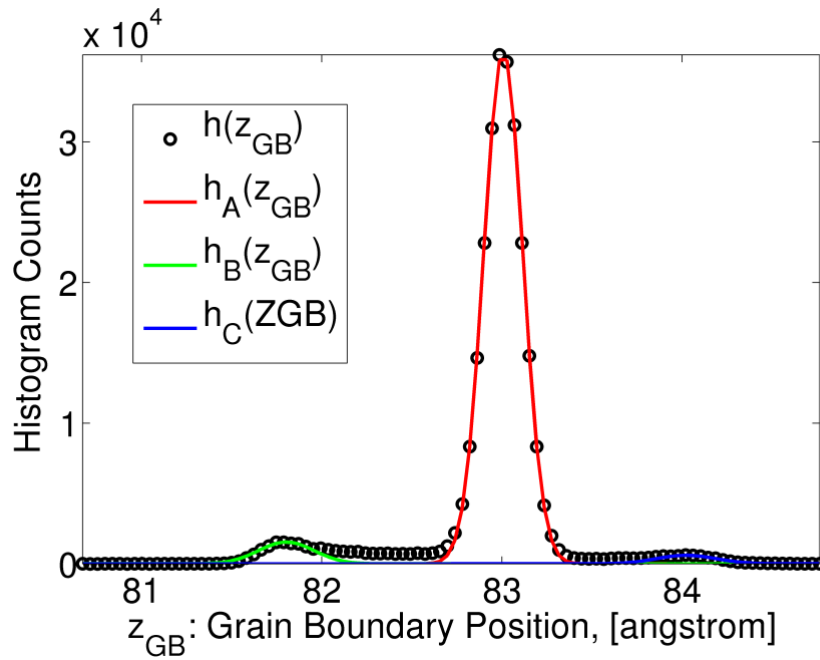


Figure 3.6: Histogram plot of  $\Sigma 17-530$  STGB being at different stable states at  $t=5000\text{fs}$ .

Further assuming that the GB has equal odds of jumping to state A or C, i.e.  $C_{AB} = C_{AC}$ .and combining Eq. (3-9) with Eq. (3-6) gives  $D = 2kT\mu_{gb}/A$ . This is the same formula as the one given by the random walk method<sup>[45]</sup>. However the two methods are not exactly the same. The most apparent difference is that our TPS calculation is mechanism specified, which means it models one type of mechanism and accordingly the rate expression (Eq. (3-6)) is exact. On the other hand in the random walk method any knowledge of the GB migration mechanisms is hidden. Moreover, considering that a GB is a 2D interface, the random walk method's use of the average GB position implies that different parts of the GB move independently. This is a very strong assumption. While in TPS calculation, the position of the GB is discretized. This assumes that all parts of the GB move together. Considering that the flat interface is energetically favorable for STGB, we believe that the TPS calculation provides a better interpretation of GBM.

### **3.5 Conclusion**

In this chapter, migration of STGB with various misorientation angles in copper bicrystals in response to a synthetic driving force method is simulated at different temperatures. Mobilities and activation energies of different GBs are then calculated and compared to the work of others. Mobilities were found to be of the same order as experimental values. Consistent with MDS results in almost all of previous publications, our activation energies are significantly smaller than experiment values. However, we propose that two mechanisms, namely coupled shear and GB sliding coexist during GBM, and the displayed activation energy is an average of two mechanisms. To model both mechanisms,

we propose a two Arrhenius term equation to which the temperature – mobility dependence is fitted. The fitting results reveals that the two mechanisms are competing during GBM and activation energies for each processes are comparable to the valued obtained experimentally. The fact that multiple mechanisms coexist during GBM inspired us to study different GBM mechanisms with TPS techniques. An investigation of the shear coupled GBM mechanism was performed in the research. The resulting mobility is consistent with previous random walk study of grain boundary mobility done by Trautt et al[74].

## Chapter 4 Micromechanics of Grain Boundary Shearing from Atomic Modeling

### 4.1 Introduction

Grain boundary (GB) migration is of essential importance in the science and engineering of polycrystalline materials. Molecular dynamics simulations have been used to model the dynamic behavior of grain boundaries. However, despite continuous efforts in this area during the past decades<sup>[42], [44]–[46], [64]–[67]</sup>, our ability to understand fundamental mechanisms are still limited to very few cases.

During grain growth, the two grains that meet at a grain boundary may, shear relative to one another in the lateral direction parallel to the grain boundary plane or migrate along the direction normal to the grain boundary. If the lateral translation rate is linearly proportional to the migration rate, then this mechanism is called shear-coupled motion, and the linear coefficient is called the coupling constant. In contrast, the motion is called grain boundary sliding (GBS) if the grain boundary does not move laterally to the shearing direction. It is believed<sup>[35], [75]</sup> that shear coupled motion is energetically preferred when geometrically allowed, but all grain boundary motion involves at least some amount of sliding, especially in cases like triple junction migration where the lateral translation of one grain against another is prohibited<sup>[35], [74], [76]</sup>. On the other hand, many systems are dominated by GBS. For instance, most of  $\langle 110 \rangle$  and  $\langle 111 \rangle$  grain boundaries<sup>[75]</sup> only slide and do not shear couple; the majority of superplastic strain in nanocrystalline metallic systems is created by grain boundary sliding<sup>[77]</sup>; deformation of grain boundary networks demands

accommodation of grain boundary sliding<sup>[76]</sup> and more generally grain boundaries with high energy at elevated temperature are more susceptible to GBS<sup>[78]</sup>.

GBS is of equal, if not greater, importance to the coupled shear during grain boundary migration processes and a considerable effort has been placed on this topic. Conventionally, GBS is studied on the macroscopic scale and is often described by various empirical governing equations. For example, in the review by Meyers *et al.* GBS mechanisms were categorized into regimes that depend on grain size. In another review paper by Landon<sup>[79]</sup>, GBS events were divided into two groups from a morphology viewpoint, Rachinger grain boundary sliding which produces no grain elongation and Lifshitz GBS which does. More recently, studies have begun focusing on the microscopic mechanisms of GBS. In Van et al.'s paper<sup>[76]</sup>, for example, GBS is accomplished by either atomic shuffling or stress-assisted free volume migration processes. In the studies by Winninga et al<sup>[47], [48]</sup>, dislocation climb is the major microscopic mechanism for grain boundary sliding, and the accompanying diffusion through bulk or along grain boundary is attributed to the activation energy differences between low angle grain boundary and high angle grain boundaries.

Despite previous efforts, our understanding of grain boundary sliding is still limited. A major reason is that GBS in the past studies always takes place with concurrent accommodating processes, such as grain boundary migration<sup>[78], [80], [81]</sup>, grain rotation<sup>[74], [82]</sup>, and inter-granular fracture<sup>[83], [84]</sup>. The symbiotic behavior of various dynamics processes is called cooperative GBS and contributes more than 50% of the total strain during super-plastic deformation<sup>[82], [83]</sup>. In this chapter, we instead of focus on how GBS is correlated with other compatible inter-granular processes and single out the GBS by finding the minimum

energy pathway (MEP) connecting two stable states before and after grain boundary sliding. The nudged elastic band technique is employed to search the MEP and the energy profile is calculated along the reaction coordinate (RC) of the MEP. Geometric characteristics of grain boundary sliding are then modeled by analyzing the unstable structures taken from the NEB calculations. The NEB calculation is then validated by comparing its values to the activation energies calculated from the Arrhenius equation.

## 4.2 Simulation

To obtain the two stable states that bracket a grain boundary sliding event, molecular dynamics simulations of f.c.c. copper bicrystals in response to synthetic driving force<sup>[42]</sup> of 0.05 eV were first performed at 700K using an embedded atom model (EAM) potential for copper<sup>[62]</sup>. Settings of the simulations are illustrated in Figure 4.1.

The simulation box contains two mirror symmetric grains, between which is a  $\Sigma 13$ -320 symmetric tilt angle grain boundary. Periodic boundary conditions were applied to all three spatial directions and thus the system contains two symmetrical tilt angle grain boundaries (STGBs). The center GB is subject to a synthetic driving force from the right to the left as shown in the Figure 4.1. The GB connecting  $z = 0$  and  $z = L_z$  was set to immobile by fixing atom positions within two 12Å thick slabs at the two ends of the cell.

Illustrated in Figure 4.1 (b) is the resulting atom configuration of the system after a time span of  $\Delta t = 1.0$  ps. Lateral translation along the  $y$  direction ( $v_{shear}$ ) and grain boundary migration along the  $z$  direction ( $v_{gb}$ ) were recorded during the simulation.

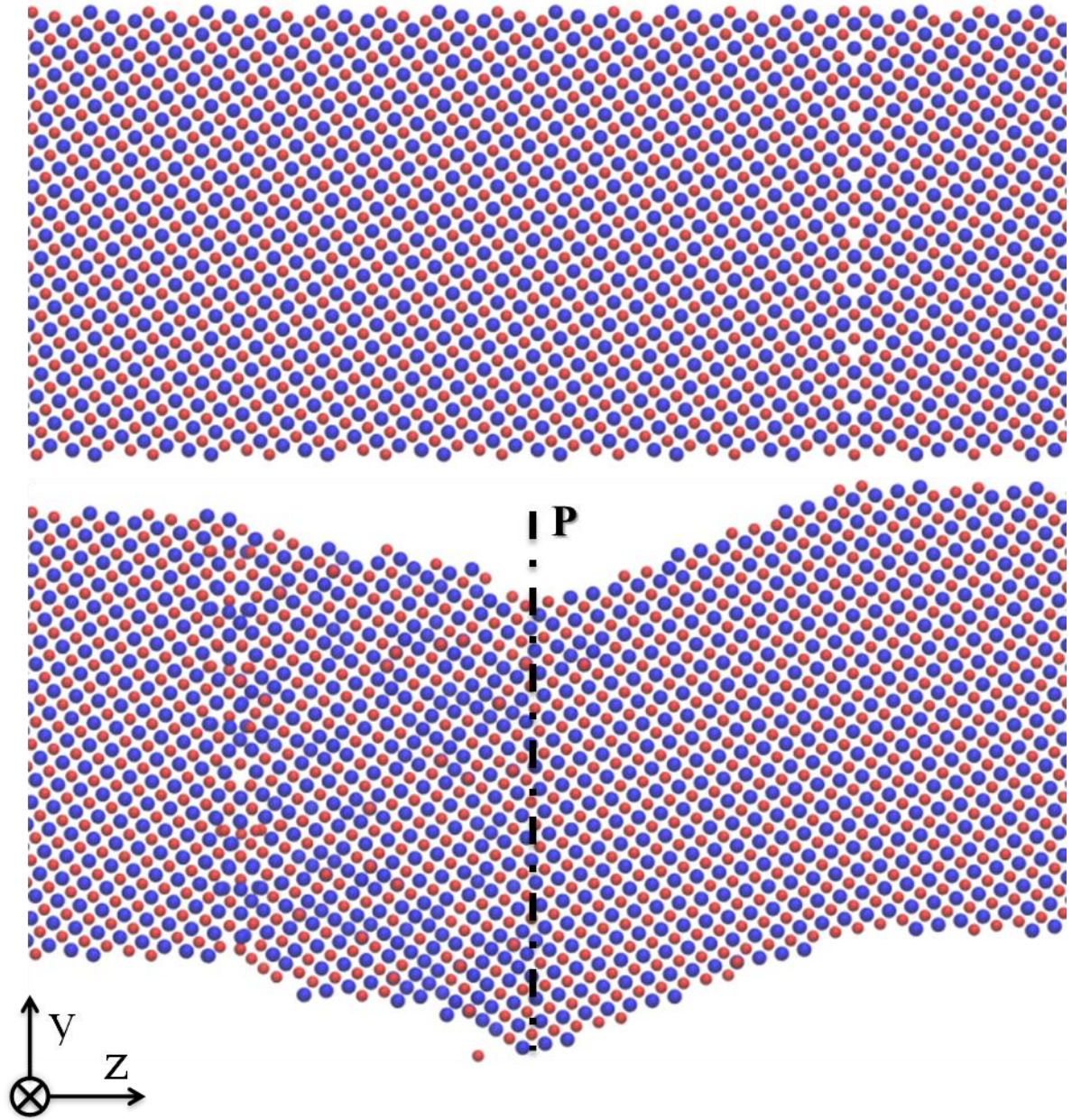


Figure 4.1: Illustration of atomistic model used in the simulation.

The two velocities are coupled in the beginning as reported by Cahn et al<sup>[51]</sup>. The coupling was then broken by grain boundary sliding as the grain boundary moved to position P shown in the Figure 4.1 (b). Atom configurations before and following the first grain

boundary sliding event were recorded and are named as “reactant” and “product” or stage A and B in the following text. Both the reactant and the product were fully relaxed at 0K to obtain corresponding stable structures. The optimum transition path between the two states was identified utilizing the nudged elastic band (NEB) method<sup>[85], [86]</sup>.

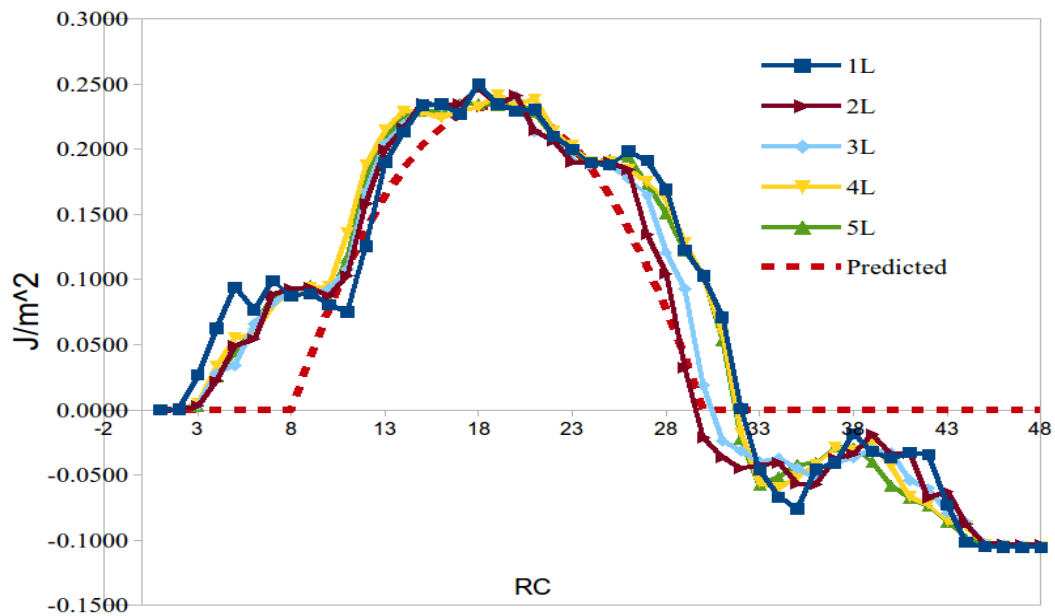


Figure 4.2: Energy profile along RC for  $\Sigma 12$ -320 with different systems sizes

Overall 48 intermediate images along the grain boundary sliding (“reaction”) pathway were involved in the NEB calculation. Each was energy minimized while maintaining equal spacing to neighboring images. The energy profiles as a function of reaction coordinate (RC) for systems with different lengths along the  $y$  direction are shown in Figure 4.2.

Three peaks exist along the RC. The major peak value of 0.224eV is the energy barrier for GBS. By analyzing the two small energy peaks prior and post the GBS event at RC=8 and RC=38, we found that these two unstable states correspond to two coupled shear events. This is reasonable because coupled shear is energetically favorable. Before the GBS event happens, coupled shear is balanced by the normal direction driving force and counter driving force due to accumulated shear stress.

After a GBS event, a coupled shear event happens almost immediately because the balance is broken due to the relief of accumulated shear stress by GBS. This indicates that GBS is the rate limiting process for the grain boundary migration (GBM) at low temperature. Follow convention<sup>[71]</sup>, system sizes are measured in units of repeating disclination structures<sup>[28], [71]</sup>. For  $\Sigma 13$ -320 STGB,  $1L = 1L_{[320]} = 13\text{\AA}$ . Different from the case of shear coupled motion<sup>[71]</sup>, energy profiles of GBS do not change significantly with system sizes. This has at least two implications. First, GBS is more likely the rate determining process during grain growth than is the shear coupled motion. This is because grain boundary mobility and the activation energy of a specific grain boundary type are intrinsic properties of a material and are considered as unchanged to systems sizes<sup>[41]</sup>. Actually, it has been found that shear coupled GBM presents many abnormal behavior beyond the range of conventional understanding of grain boundary migration<sup>[75]</sup>. Second, the fact that energy barrier for shear coupled GBM decreases significantly with grain boundary size indicates that calculations of grain boundary mobility under equilibrium conditions, such as the random walk method<sup>[45]</sup> and derivative methods thereafter<sup>[64]</sup>, may overestimate the true grain boundary mobility.

This is because shear coupled motion, if available, moves faster and is energetically more favorable than other GBM mechanisms at low temperature without a driving force<sup>[35], [75], [87]</sup>.

### 4.3 Results and discussion

Different from coupled shear GBM, GBS does not progress through disconnected motions<sup>[71], [88]</sup>. Analysis of the metastable configurations along the MEP shows structural changes as demonstrated in the Figure 4.3. The colored arrows denote the geometry change for typical shear and GBS. Atoms on the two sides of each arrow are considered as equivalent atoms because the position on the end of one arrow will copy the position of the atom on the beginning of the arrow after coupled shear or a GBS event happens. Take the coupled shear as an example, its geometry vector is  $\frac{1}{2}[01\bar{1}]$ . This indicates that the coupling constant for this tilt angle grain boundary is  $\beta_{[032]} = 1/5 = \tan \theta_{\langle [01\bar{1}], [032] \rangle}$ . This value has been proven to be correct both experimentally and numerically<sup>[71], [74], [75], [87]</sup>. Whereas there has been an explosion in the number of papers dealing with geometry coupling phenomenon in shear coupled grain boundary migration, there rarely has been any reports talking about geometry aspects of grain boundary sliding. By comparing the atomistic configurations before and after a sliding event as illustrated in the Figure 4.3, we propose that  $[00\bar{1}]$  is the characteristic vector for the sliding event with two accompanying shear coupled events. This means that for each time grain boundary migrate leftward by  $\Delta Z_{gbs}$ , the left grain will move upward, relative to the right grain, by  $\Delta Y_{gbs}$ . These values are:

$$\Delta Z_{gbs} = \frac{[00\bar{1}] \cdot [02\bar{3}]}{|[00\bar{1}]||[02\bar{3}]|} = \frac{3}{\sqrt{13}},$$

$$\Delta Y_{gbs} = -\frac{[00\bar{1}] \cdot [032]}{|[00\bar{1}]||[032]|} = \frac{2}{\sqrt{13}} \quad (4-1)$$

To further elucidate the contribution of GBS to the overall GBM, NEB calculations with similar setups were performed for 26 symmetric tilt angle grain boundaries (STGBs) with misorientation angle ranges from 12.68 ° to 78.58 °. Meanwhile non-equilibrium constant temperature molecular dynamics simulations (MDS) of GBM under a synthetic driving force were performed for the same set of systems at different temperatures from 400K to 1150K to extract activation energies from the temperature dependence of GB mobilities.

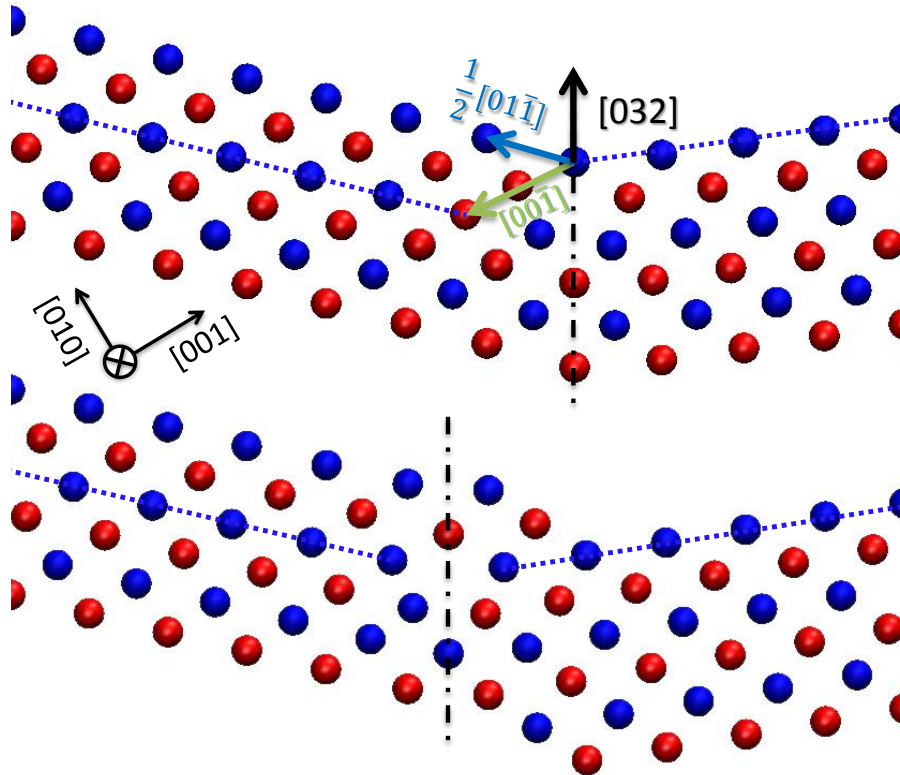


Figure 4.3: Geometry characteristics of grain boundary sliding.

The relationship between the NEB energy barrier heights ( $\Delta E_{NEB}$ ) and GB misorientation angles ( $\theta$ ) are summarized in Figure 4.2, from which a good match is shown between  $\Delta E_{NEB}(\theta)$  and activation energies ( $E_a(\theta)$ ). This is not surprising. According to transition state theory, the activation energy (eV) can be viewed as the energy required for one atom to jump across a GB interface, and the NEB energy barrier ( $\text{J/m}^2$ ) is the energy required for a GBM event where a GB is treated as one dimensional object. The two quantities are connected by Eq. (4-2) based on the reasoning that at 0K, elevation of the internal energy of atoms in one grain by the amount of activation energy will just make them move across the GB. On the other hand, the GBS is just possible if the GB energy is elevated by  $\Delta E_{NEB}$ . On these premises, the work required to drive a GB to slide along the  $\hat{Y}$  direction, which is  $p\Delta V = (E_a/V_{atom}) (\delta Y_{GBS} A_{GB}/2)$  as is demonstrated in the Figure 4.4, is equal to the energy required to activate the GBS, i.e.  $\Delta E_{NEB} \cdot A_{GB}$ . This gives us a relationship to convert a unit of activation energy (eV) to that of the NEB energy barrier height by:

$$\frac{p\Delta V}{A_{GB}} = \frac{1}{2} \frac{E_a \cdot \delta Y_{GBS}}{V_{atom}} \approx \Delta E_{NEB} \quad (4-2)$$

where  $\delta Y_{GBM}$  is the shear strain change due to a GBS event,  $V_{atom} = a^3/4$ ,  $a$  is the lattice constant and the  $1/2$  is because the activation energy barrier is symmetric with respect to  $\Delta Y_{GBM}$ . Details of  $\delta Y_{GBM}$  are discussed in the following text. For  $\Sigma 13-320$ ,  $\Delta Y_{gbs} = 2a/\sqrt{13}$  as is given in Eq. (4-1). GBS energy barrier heights, activation energy and its translation based Eq. (4-2) are shown in Figure 4.4. The reasonable match among curves not only supports the validity of our analysis but also indicates GBS events are the rate limiting process for the GBM. In addition, it shows that the NEB calculation provides a quick and

elegant way to estimate activation energies for GBM. Conventionally, activation energy calculations require non-equilibrium MDS at various temperatures and MDS at each temperature usually takes a long time to finish due to the slow dynamics nature of GBM. In addition each MDS must be carried out for multiple times to compute ensemble averages. In contrast, the NEB calculation only needs to be performed once for each system.

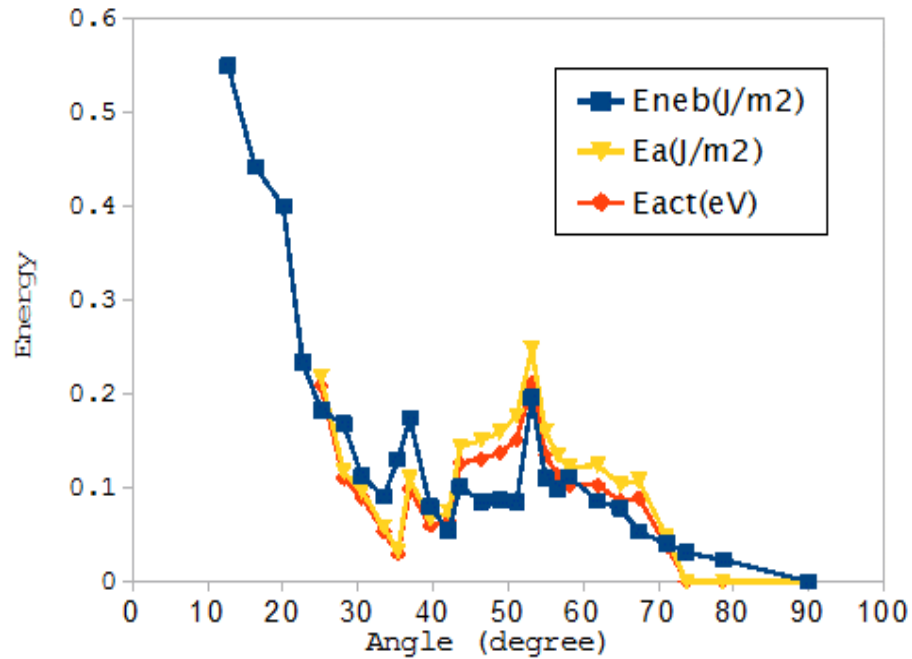


Figure 4.4: Comparison between barrier heights from NEB calculations and activation energies from Arrhenius law

## **Part 2, Nano reactive material**

### **Chapter 5 An Introduction to Nano Energetic Materials**

Nano energetic materials (NEMs) are emerging as next generation reactive materials that have high energy density and reactivity. NEMs can be grouped into two categories depending on the composition and reaction type.

#### **5.1 Nano metallic composites**

Reactive nano-metallic composites (RNMCs) are usually alternating nano-laminates synthesized using vapor deposition that consists of two or more metallic materials that produce significant heat when mixed. RNMCs can be classified according to the composites' components. Basically they contain two types of metals: one metal with high reducibility, such as Al, Li and Mg, and one with less reducibility, such as Ni, Zr and Pt.

RNMCs are generally stable in low temperature and intermixing typically occurs only at high temperature. The types of intermixing (reaction) for nano-metallic composites can also be divided into two groups: slow reaction at mild elevated temperature and fast self-sustained combustion ignited by flame or laser pulse. This former is often seen in differential scanning calorimetry experiments where the temperature is ramped linearly from a low initial temperature to a preset high temperature at a rate of  $\beta$  (°C/min), and heat release (W/g) is recorded as a measure of the degree of reaction to which the mixing proceeds. Usually

multiple peaks are apparent in DSC thermographs as a result of two competing processes. (1) Typically reaction rates grow exponentially with temperature. (2) Amount of reactant decrease also exponentially (integral of reaction rate with respect to time) with the temperature. Peak temperatures obtained from DSC experiments can be used to find the activation energy for the reaction/mixing. Activation energies for a few typical systems are listed in the Table 5.1 . It has been found that the activation energies for reactions in RNMCs are frequently comparable to the activation energies of various diffusion processes in solids. This suggests that most of the reactions in RNMCs are diffusion controlled <sup>[89], [90]</sup>.

Table 5.1: Experimental measured parameters for typical metallic laminate composites.

	$E_a$ (eV) from DSC	BL Thickness (nm)	Temperature °C	$-H_{mix}$ (kJ/mol)
Ni – Ti	1.1 – 1.2	10 – 100	~1450	34 <sup>[91]–[94]</sup>
Ti – Al	1.5 – 2.4	4 - 200	~1100	73 <sup>[95], [96]</sup>
Ni – Al	~0.8 <sup>[97]</sup> , 1.26 – 1.9	25 – 200	> 1200	28 – 59 <sup>[91], [98], [99]</sup>
Zr – Al	1.84±0.05	17 – 90	>1500	53 <sup>[100]</sup>
Pt – Al	1.0	76 – 550	> 2800	57 – 100 <sup>[101], [102]</sup>
Nb – Si	0.8	39 – 312	> 1500	41.8 <sup>[103]</sup>

The other type of reaction for RNMCs is commonly referred to as a self-sustaining reaction in which ignition is triggered at a local site and spreads out because the heat release rate due to the local reaction is much faster than the heat dissipation rate. The ignition conditions vary widely depending on the size of RNMCs and thermal dissipation conditions. A few reported ignition conditions are listed in the Table 5.2, from which we can see that powder systems normally have higher ignition temperatures than the nano laminate system,

and that transition metal composites usually require high ignition condition. As for the local temperatures for self-propagating reactions of RNMCs, they are usually so high that they often exceed the melting point of one or more constituent metal. For instance, the local temperature for self-sustaining reaction in a Pt – Al NRMC can be greater 2800 °C, while the melting temperature of Al is only about 660 °C. The feature of high reaction temperature and enormous exothermicity make RNMCs suitable for self-propagating high temperature synthesis (SHS).

Table 5.2: A list of ignition temperature for metallic composite systems

	<b>Ignition conditions</b>
<b>Ni – Ti Laminates</b>	~ 300 – 400 °C [92]
<b>Ni – Ti Powders</b>	~ 900 – 930 °C [92]
<b>Ni – Al Laminates</b>	~ 223 °C [97]
<b>Nb/Ti/Mo – Si Laminates</b>	> 1000°C [103]

## 5.2 Nano thermite composites

Nano-thermite composites (NTC) are reactive composites consisting of metals (often named as the fuels) and metallic or non-metallic oxides (also known as the oxidizers). A generic chemical reaction equation can be expressed as a common form of oxidation-reduction reaction



Compare to metallic composites, thermites not only have much larger enthalpy of formation but also has more stable enthalpy of formation. That being said, enthalpy of

formation for RNMCs is dependent on the final reaction products, which vary widely depending on the alloy's phase diagram and the reacting temperature. Meanwhile, the reacting temperature is a result of competition between the endothermic reaction and the heat dissipation. This indicates that the effective enthalpy of reaction for the same RNMCs may vary from one experimental condition to another. For example, during the self-propagated combustion of an Al/Ni RNMC, the equilibrium phase diagram suggests a transient product of solid AlNi and liquid at a local temperature about 1700K<sup>[93]</sup>. In the more mild reaction condition with reacting temperature below ignition temperature, however, various products are reported<sup>[98]</sup> such as Al<sub>9</sub>Ni<sub>2</sub>, Al<sub>3</sub>Ni, Al<sub>3</sub>Ni<sub>2</sub> and Al<sub>82</sub>Ni<sub>18</sub>, with the effective enthalpy of formation varying accordingly.

Also different from RNMCs, which are mostly laminated and synthesized using vapor deposition, most of the reported NTCs are mixture of loose powders composed of metal and oxidizer nanoparticles. Although in many cases metal and oxidizer particles are in intimate contact and can be viewed as bilayer materials, the reactivity is lower by a factor of 2 to 3 in powder mixture systems compare to multilayer films<sup>[104]</sup>.

In searching of NTCs that have high possible reaction rates and low ignition decays, many NTCs with various nano-structures have been synthesized based on modern nano synthesizing technologies, such as deposition<sup>[105], [106]</sup>, Atomic layer deposition<sup>[107]</sup>, nanoporous templates. Blobaum *et al.* sputter deposited alternating layers of Al – CuO thin films (with bilayer thickness of 1 $\mu$ m) onto silicon substrates<sup>[105]</sup>. Recently, more laminated NTCs, including Zr/CuO, Mg/CuO *etc*, have been synthesized by Mily *et al*<sup>[106]</sup>. Yuma, et al. synthesized Al coated CuO nanowires (NWs) by first electroplating Cu onto steel plate to

grow Cu NWs, then oxidized Cu with thermal annealing and finally deposited Al onto CuO NWs with by magnetron sputtering. Ferguson et al.<sup>[107]</sup> synthesized enhanced thermite composites by coating SnO<sub>2</sub> onto Al nano particles (NPs) using the atomic layer deposition (ALD).

Table 5.3: Recent advances in synthesizing nano-thermites using various technologies.

Material	Nano structuring	Reaction specifications	Synthesis methods
<i>Al/CuO<sub>x</sub></i> multiplayer foils	Bilayer thickness ~1μm	$E_a = 146 - 460$ kJ/mol, combustion temperature $\geq 2846$ K	Sputter deposition <sup>[105]</sup>
Al, Mg, Zr + CuO multilayer films	Bilayer thickness 350 – 500nm	Onsets of reaction occurs 800 °C, 500 °C, and 300 °C for the Al, Mg, and Zr systems respectively	sputter deposition <sup>[106]</sup>
Fe <sub>2</sub> O <sub>3</sub> coated KMnO <sub>4</sub> + Al NPs	~150nm NP with 4 – 16nm coating	Reactivity can be increased by a factor of 10.	Aerosol spray- pyrolysis <sup>[108]</sup>
<i>Al/CuO<sub>x</sub></i> Core/shell NWs	Average length: 3- 7μm and diameter: 40-90nm.	$E_a = 250 - 207$ kJ/mol	Electroplating and deposition <sup>[109]</sup>
SnO <sub>2</sub> coated Al NPs	$R_{Al} \approx 51.2$ nm $R_{SnO_2} \approx 3.4$ nm	Detonates orders of magnitudes more rapidly than uncoated Al nano particles.	Atomic layer deposition <sup>[107]</sup>
Fe <sub>2</sub> O <sub>3</sub> NWs embedded in Al	NW diameter: ~50nm, length: ~25nm	Ignition temperature as low as 400°C, combustion temperature as high as 4000°C	Nano-porous alumina template <sup>[110]</sup>
Al + Fe <sub>2</sub> O <sub>3</sub> NPs	NP diameter: 100 – 200nm	Burning rate is increased by a factor of 10.	Enhanced assembling <sup>[111]</sup>

Nano-porous templating has also been used to synthesize nano thermites, for example, Fe<sub>2</sub>O<sub>3</sub><sup>[110]</sup> and CuO<sup>[112]</sup> NWs embedded in an Al matrix. Another example of a

novel nano thermite structure is made using an enhanced assembling method in which mixing of metal and oxidizers in making conventional thermites is enhanced by adding charges or functional groups onto the thermite reactants<sup>[111],[113]</sup>. More details of these nano-thermites' synthesizing methods, nano structuring, and reaction specifications can be found in the Table 5.3 and in a review by Rossi *et al*<sup>[114]</sup>.

### **5.3 Characterization and modeling solid reaction for nano reactive materials**

It has been widely proved that reaction kinetics in NEMs is controlled by mass transport from one reactant into the others. Similar to the categorization of reaction types for NEMs, studies of reaction kinetics in NEMS can also be grouped into two categories. One focuses on modeling the self-propagating combustion and the other focuses on fitting the kinetics data obtained from the thermal analysis.

#### **5.3.1 Modeling Self – Propagated Combustion**

Thanks to the strong exothermal reactions, NEMs have found wide application in industry through self – propagating high temperature synthesis (SHS) process. The propagation speed of combustion front/flame has been proven critical in understanding the reaction mechanisms and kinetics in many situations. In most cases, NEMs with high possible combustion speed is preferable and numerous efforts have been dedicated to achieve that goal. For example, it has been shown that mixtures of nanoparticles, nano rods or nano wires can increase combustion speed several orders compared to conventional micro-size particles<sup>[115]</sup>. Moreover, compared to physical mixing composites, self – assembled composites can achieve higher combustion speed<sup>[113]</sup>. Analytical models for different NEM

systems may vary significantly. In this section, the ideal system of multilayer laminates is considered only for simplicity.

As mentioned above, the self – propagation combustion of NEMs are mostly diffusion controlled. Hence the governing equations for self – propagating combustion usually consists of at least a mass diffusion equation, (Eq.(5-2)) and heat dissipation equation (Eq. (5-3))

$$\frac{\partial C}{\partial t} = \nabla \cdot (D \nabla C) \quad (5-2)$$

$$C_p \frac{\partial T}{\partial t} = \nabla \cdot (\kappa_T \nabla C) + \dot{Q} \quad (5-3)$$

where  $C$  and  $D$  are the concentration of reactants and diffusion coefficients, respectively, and  $C_p$  and  $\kappa_T$  are the heat capacity and diffusivity, respectively, and  $\dot{Q}$  is the heat generation from solid reactions. The latter is usually a complex empirical function of the composition and temperature of the solid. For instance, in a paper by Jayaraman *et. al*<sup>[116]</sup>,  $Q$  is assumed proportional to the reactants' concentration, i.e.  $\dot{Q} \propto \dot{C}(t)$ , while in the papers by Salloum *et. al*<sup>[117]-[119]</sup>,  $Q$  is proportional to the integral of the squared composition over the combustion region, i.e.  $\dot{Q} \propto \partial \int_{\Omega} C^2(t) d\Omega / \partial t$ .

To analytically solve Eq. (5-2) and Eq.(5-3), they are normally reduced to one dimension along the flame propagation direction with radical approximations<sup>[117], [120]</sup>. The most important result (out of many meaningful findings based on analytical work) for self – propagated combustion in laminated thin foils is the following expression

$$v^2 \propto \frac{\lambda^2 R T_f^2 \cdot A e^{-\frac{E_a}{R T_f}}}{\delta^2 E_a (T_{f0} - T_0)} \quad (5-4)$$

where  $\lambda$  is the thermal diffusion coefficient,  $T_f$ ,  $T_{f0}$  and  $T_0$  are the peak temperature, ignition temperature of the flame and the environmental temperature respectively,  $\delta$  is the thickness of each layer (assuming layers of equal thickness), and  $A$  and  $E_a$  are the pre-exponent and the activation energy of the atomic diffusion. Eq. (5-4) indicates that the propagation speed is proportional to the inverse of laminate thickness. This has been proved both numerically and experimentally<sup>[121]</sup>.

### 5.3.2 Modeling the thermal analysis curves

In the study of solid state reactions, thermal analysis, isothermal or non-isothermal aims at measuring the dependence of reaction rates on the temperature, i.e. the relation expressed as

$$\frac{d\alpha}{dt} = A e^{-\frac{E_a}{RT}} f(\alpha) \quad (5-5)$$

where  $\alpha$ ,  $A$  and  $E_a$  (known as the kinetic parameters) are the extent of reaction, pre-exponent and activation energy, respectively. The function  $f(\alpha)$  is known as physio-geometry kinetics model function which, in most cases, is derived by assuming an ideal reaction mechanism in a simple reaction geometry. Let's take the most frequently used 1-D diffusion model as an example: Assume an intermediate layer, whose thickness is  $l$  and grows with time, is formed during the redox reaction in a bilayer Al – CuO composite as shown in Figure 5.1. Further assume that the overall kinetics is controlled by Al migrating to CuO. By saying that, the

growth rate for the middle  $Al_2O_3$  layer is proportional to the amount of Al atoms migrated from Al region to the interface between the  $Al_2O_3$  and the CuO.

Table 5.4: Frequently used model functions for solid state reactions

Symbol	Model	Model function $f(\alpha)$	$g(\alpha)$
D1	1-D diffusion	$\frac{1}{2\alpha}$	$\alpha^2$
D2	2-D diffusion	$-\frac{1}{\ln(1-\alpha)}$	$(1-\alpha)\ln(1-\alpha) + \alpha$
D3	3-D diffusion	$\frac{3}{2} \frac{(1-\alpha)^{2/3}}{1-(1-\alpha)^{1/3}}$	$\left[1 - (1-\alpha)^{1/3}\right]^2$
D4	4-D diffusion	$\frac{3}{2} \frac{(1-\alpha)^{1/3}}{1-(1-\alpha)^{1/3}}$	$1 - \frac{2}{3}\alpha + (1-\alpha)^{2/3}$
R2	2-D phase boundary migration	$2(1-\alpha)^{1/2}$	$1 - \sqrt{1-\alpha}$
R3	3-D phase boundary migration	$3(1-\alpha)^{1/3}$	$1 - (1-\alpha)^{1/3}$
A2	2-D nucleation	$2(1-\alpha)[- \ln(1-\alpha)]^{1/2}$	$[- \ln(1-\alpha)]^{1/2}$
A3	3-D nucleation	$3(1-\alpha)[- \ln(1-\alpha)]^{2/3}$	$[- \ln(1-\alpha)]^{1/3}$
R <sup>1</sup>	1 <sup>st</sup> order reaction	$1-\alpha$	$-\ln(1-\alpha)$
R <sup>n</sup>	Nth order reaction model (n≠1)	$(1-\alpha)^n$	$\frac{1 - (1-\alpha)^{-(n-1)}}{n-1}$

According to the Fick's law, this relationship can be expressed as

$$\frac{dl}{dt} = D \frac{dC_{Al}}{dx}$$

where  $C_{Al}$  is the concentration profile of Al atoms,  $D$  is the diffusion coefficient and  $l$  is the thickness of the barrier layer ( $Al_2O_3$ ). Further, assume that the concentration of Al atoms distributes linearly across the barrier layer, i.e.  $dC_{Al}/dx = C_{Al}^0/l$ , where  $C_{Al}^0$  is the saturated concentration of Al in Al. Applying the linear approximation leads to the following expression

$$\frac{dl}{dt} = D \frac{C_{Al}^0}{l} \quad (5-6)$$

Let  $\alpha \equiv l$  and  $A \equiv 2C_{Al}^0D = 2C_{Al}^0D_0 e^{-\frac{E_a}{RT}}$ , Eq. (5-6) can be reduced to the same form as Eq. (5-5) with model function  $f(\alpha) = 1/2\alpha$ .

Similarly, model functions for more complicated reaction geometries or mechanisms can be derived and several of them are summarized in the Table 5.4. More information can be found in a review article by Ammar and Flanagan<sup>[122]</sup> or other similar review articles<sup>[123]–[127]</sup>.

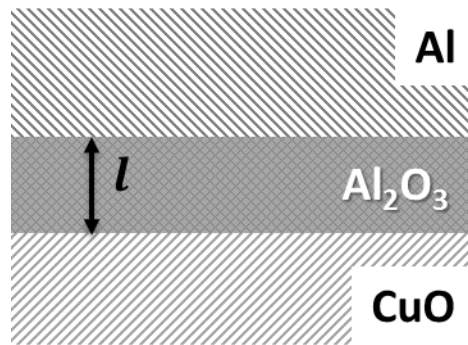


Figure 5.1: Illustration of idea 1-D diffusion model for laminate Al – CuO thermite composite

Despite that the genetic kinetic functions have been widely used in the past decades, they are facing adverse criticism in many aspects<sup>[123], [125]</sup>, such as:

1. The physical meanings of the kinetic parameters are unclear. The cause of this is at least two fold: (i) experimental data can often be fit to multiple model functions in practice; and (ii) Kinetic parameters, such as pre-exponent parameters, are non-specific when it comes to real problems.
2. Often the retrieved kinetic parameters such as activation energies are dependent on experiment factors due to the conflict between inherent uncertainties in the solid-solid reactions and the over simplification for the generic model functions.

With the model functions in hand, the thermal analysis data can be interpreted by two analytical methods: model fitting and the isoconversion method respectively. Both of the two methods start from integrating the model functions in Eq. (5-5).

$$\int_0^t A e^{-\frac{E_a}{RT(\tau)}} d\tau = \int_0^\alpha \frac{d\alpha'}{f(\alpha')} \equiv g(\alpha) \quad (5-7)$$

where  $\tau$  and  $\alpha'$  are dummy variables for integration. The right side of Eq.(5-7), i.e.  $g(\alpha)$ , is known as the “temperature integral”, typical forms of which can be found in the Table 5.4.

The left side of the equation is dependent on the thermal condition. Under isothermal conditions, the integral is  $A \exp(-E_a/RT) \cdot t$ . Under non-isothermal conditions, only an approximate form can be found due to the non-linearity inherent to the exponential integral.

One assumption introduced by Coats–Redfern<sup>[128]</sup> gives rise to Eq.(5-8). It assumes that temperature is linearly dependent on time, i.e.  $T(t) = \beta t + T_0$  where  $\beta$  is the heating rate and  $T_0$  is the initial temperature,

$$\ln \frac{g(\alpha)}{T^2} = \ln \left[ \frac{AR}{\beta E_a} \left( 1 - \frac{2R\bar{T}}{E_a} \right) \right] - \frac{E_a}{RT} \quad (5-8)$$

where  $\bar{T}$  is the average experiment temperature.

The model fitting method and isoconversion method diverge hereafter depending on how Eq.(5-8) is interpreted. Take a DSC curve from a numerical simulation, which we will discuss in detail in the next chapter, as an illustration.

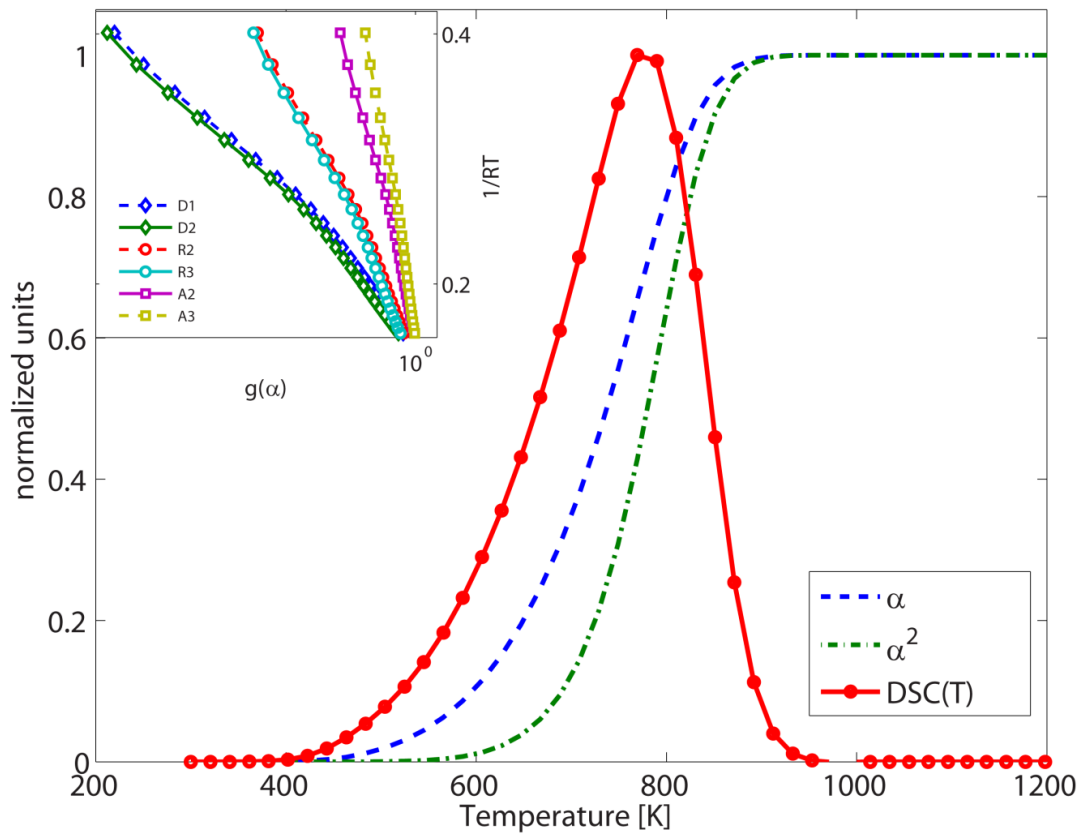


Figure 5.2: Demonstration of using a model fitting method to interpret DSC curves. The solid line with cycles is the normalized DSC curve as a function of temperature. The insert are the model fitting curves based on various model functions listed in Table 5.4.

The model fitting methods treat the activation energy as a constant, and calculate  $\alpha$  from thermal analysis data. In this case it can be calculated as a cumulative integration over temperature, i.e.

$$\alpha(T) \equiv \frac{\int_{T_0}^T DSC(T')dT'}{\int_{T_0}^{\infty} DSC(T')dT'} \quad (5-9)$$

The model fitting curves can then be found by substituting various forms of  $g(\alpha)$  into Eq. (5-8). Theoretically the best  $g(\alpha)$  that provides the best linearity of the plot  $\ln[g(\alpha)/T^2]$  vs.  $-1/RT$  can be chosen as the “correct model” and its negative slope is the value for “correct” activation energy. However, as demonstrated in Figure 5.2, in practice many models fit almost as well as (or from another angle, as badly as) the best model does.

Different from modeling fitting method, which require only one DSC curve, isoconversion method require multiple curves with, for example, different heating rates. Slight rearrangement of Eq. (5-9) will yields

$$\ln \frac{\beta}{T^2} = \ln \left[ \frac{AR}{g(\alpha)E_a} \left( 1 - \frac{2R\bar{T}}{E_a} \right) \right] - \frac{E_a}{RT} \quad (5-10)$$

Similar to model fitting method, extent of reactions, or in this context, conversions are calculated through Eq. (5-9). Further if temperatures ( $T_f$ ) at which certain fraction ( $f$ ) of conversion are found and are substituted into Eq.(5-10), the first term on the right hand side will become constant. The plot of  $\ln[g(\alpha)/T_f^2]$  against  $-1/RT_f$  will then give rise to

linear lines as shown in the Figure 5.3. This method is known as the modified Coats–Redfern<sup>[122]</sup> method.

Generally speaking it is widely believed that the isoconversion method is superior to the model fitting method, but generally speaking they both have pros and cons:

1. Model fitting methods require assumptions, which means an explicit form for  $g(\alpha)$ , which is likely an oversimplified model for real solid reactions derived under the isothermal assumption, is required before data fitting. It has been shown that this can give rise to highly uncertain kinetic parameters<sup>[129]</sup>, especially for non-isothermal data<sup>[123]</sup>.
2. The isoconversion method is considered a model-free method due to its model non-specific nature. However, it is because of this nature that the isoconversion method can only evaluate the activation and no other<sup>[122]</sup>.
3. Both of the methods require integration over DSC/DTA to obtain the extent of reaction, i.e.  $\alpha$  which is very likely erroneous. Notice that Eq.(5-10) is strikingly similar to Kissinger's analysis<sup>[130]</sup> only that temperatures used in Kissinger's analysis are temperatures at which DSC curves reach maxima but here they are temperatures with fixed state of transformation. As a matter of fact, they are often used indiscriminately in thermal analysis. This leads to some error, but on the other hand, it is often very inaccurate to integrate a DSC/DTA curve to obtain the degree of transformation due to the uncertainties in determining the base line and errors in the measurement of the sample temperature. Compare the tradeoff between two errors, the former is often favored in practice. In the next chapter, we will develop a new

method in which either the integration over DSC/DTA or the approximation that isoconversion temperature equals the peak temperature is not required.

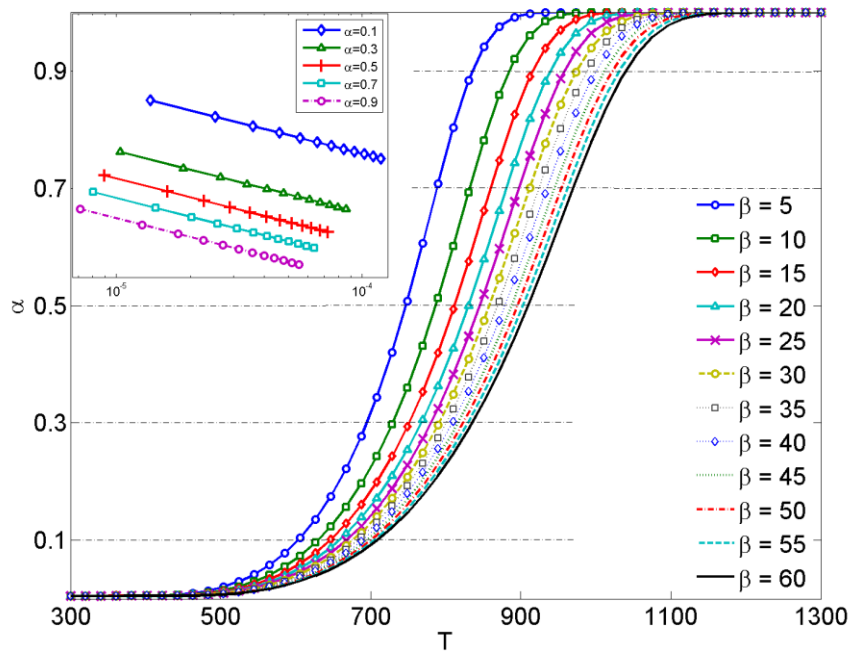


Figure 5.3: Demonstration of using isoconversion method to analyze DSC curves with various heating rates. The temperatures at which certain degrees of reaction have proceeded were found as the cross points of solid curves and horizontal dashed lines. The insert shows the fitting of the Eq.(5-8).

Recall that Eq.(5-8) is only one approximation out of many. For decades, researchers have made different approximations, many of which are applicable only under very strict conditions. Interested readers can find profound information from many excellent reviews in this area<sup>[122], [127], [131]-[133]</sup>.

## **Chapter 6 Interpretation of Differential Scanning Calorimetry Data of Energetic Nanostructures based on Diffusion-Controlled Kinetics**

### **6.1 Introduction and Background**

As mentioned in the previous chapter, nano-structures within which energy is released by solid-state reactions are of interest from both fundamental science and application viewpoints. Thermites, for example, release energy via solid-state reduction-oxidation reactions involving oxygen transfer from a metal oxide to a complementary metal. Similarly, multi-metal systems can release energy via formation of thermodynamically-stable alloys. Nano-structuring these systems can produce an extremely large interfacial area within a small volume, which in principle can be exploited to control power and sensitivity to temperature and external perturbations like shock loading. Rational engineering of such structures, however, requires understanding how the nano-structure combines with the intrinsic chemical kinetics of the solid-state reaction to control the amount and rate of energy release.

Techniques such as differential scanning calorimetry (DSC) and differential thermal analysis (DTA) are well established for probing solid reaction kinetics. In a traditional power-compensated DSC experiment, the sample and reference materials are kept thermally insulated from each other but the temperatures of both are synchronized and elevated linearly with time. The amount of energy that is necessary to synchronize the temperature is recorded as a function of temperature. In DTA, identical heat flows to both the sample and reference material is maintained, and an uncompensated temperature difference between the two is

measured as a function of temperature. Kinetic parameters such as activation energies have been obtained from DSC using a Kissinger analysis<sup>[130]</sup> and its derivatives,<sup>[134]–[136]</sup> including studies of nanostructured multi-layered systems.

Existing methods for extracting reaction kinetics from DSC curves can be categorized into two groups, peak temperature methods that require the temperature at which the maximum transformation rate is reached, and isoconversion methods<sup>[136]</sup> where the time to complete a certain degree of transformation is considered. Despite the wide application and apparent success of these analyses in interpreting DSC and DTA data<sup>[97], [100], [109]</sup>, as mentioned in the previous chapter, the following limitations still exist:

4. The physical meaning of the apparent kinetic parameters retrieved from a Kissinger-like analysis is not always clear. To explore possible reaction mechanisms, thermal analysis data can be fit to an assumed  $f(\alpha)$  using a “*trial-and-error*” procedure. This method, however, is prone to inaccuracies because experiment data can often be fit to more than one kinetic function with apparently equal success<sup>[132], [137]</sup>.
5. Peak temperature methods, such as Eq.(6-1), are generally more precise than the isoconversion methods. This is because in a strict isoconversion the degree of transformation is usually calculated by cumulatively integrating the DSC/DTA thermogram. This method can be very inaccurate due to uncertainties in determining the base line and errors in the measurement of the sample temperature. On the other hand, in strict peak temperature methods, expressions for the kinetic function  $f(\alpha)$  are required. For practical reasons only simple and empirical algebraic expressions, such as the  $n^{\text{th}}$  order equation, are used. Those equations are almost all based on

approximations<sup>[133], [138]</sup> and are considered proper largely because the actual kinetic functions are too complicated to be derived.

6. In other situations, the maximum rate temperature is often considered the same as the temperature at the constant amount transformed. However, this assumption is not always true and it is highly dependent on the reaction mechanism. Use of peak temperatures indiscriminately may lead to large uncertainties.
7. In general the effects of geometry on reaction kinetics is not considered. This limitation is the most especially pertinent for DSC to understand solid-state reaction kinetics in nanostructures.

In this chapter, an explicit form of a non-isotherm function for diffusion controlled kinetics is proposed that is based on Fick's diffusion equation. This form is used to derive analytical expressions for DSC curves and their peak temperature that leads to a Kissinger-like analyses of diffusion controlled kinetics. Furthermore, in addition to the heating rate dependence of peak temperatures as revealed by all Kissinger-like analyses, our kinetic function is able to take laminate, cylindrical and spherical geometries into account by changing a single parameter. To illustrate the utility of this new relation, the change in temperature at the maximum in the first DSC peak with bi-layer thickness for a Zr – CuO nano-laminate thermite and a multi-layer Ni/Al aluminide are analyzed, and it is shown that data for the different bi-layer sizes all fall on the same straight line with an appropriate geometry scaling.

## 6.2 Formulation

The starting point is the one-dimensional mass diffusion equation

$$\frac{\partial C(x, t)}{\partial t} = x^{-m} \frac{\partial}{\partial x} \left[ x^m D \frac{\partial C(x, t)}{\partial x} \right] \quad (6-1)$$

where the dimensionless Schvab-Zeldovich variable  $C(x, t)$  describes the degree of atom mixing at position  $x$  and time  $t$ <sup>[116], [119], [139], [140]</sup>. The initial conditions and  $C(x, t)$  are defined so that for the region initially containing the species responsible for exothermic reaction  $C(x, 0) = 1$ , while throughout the region to which this species diffuses initially  $C(x, 0) = -1$ . The quantity  $m$  in Eq. (6-1) denotes the geometry and the corresponding coordinate system in which Eq. (6-1) is defined. Values of  $m=0, 1$  and  $2$  correspond to laminates (Cartesian coordinates), wires (cylindrical coordinates) and spheres (spherical coordinates), respectively (see Figure 1). Diffusion is assumed normal to the interfaces between the initial regions for each structure (i.e. quasi-one-dimensional diffusion), and the kinetic parameters for diffusion are assumed to be the same for both regions. For the laminates this leads to a constant value of  $C(x, t > 0) = 0$  at the interface between the different regions. This boundary condition is imposed on the solution for the cylindrical and spherical geometries, as well as the natural boundary condition  $\partial C / \partial r|_{r=0} = 0$ . Although prior studies suggest that thermite reactions, for example, are often regulated by oxygen diffusion<sup>[141]–[143]</sup>, Eq. (6-1) does not discriminate with respect to reacting species or diffusion mechanisms.

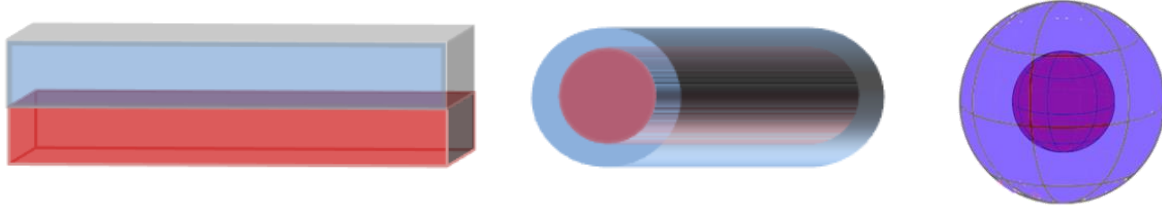


Figure 6.1: Illustration of sample geometries considered. Left: Laminate, Center: Cylinder, Right: Sphere.

Based on the assumption that mass diffusion is the rate limiting process, DSC curves can be defined as

$$DSC\left(\frac{T - T_0}{\beta}\right) = \dot{Q}(t) = \Delta H \frac{\partial}{\partial t} \int_{\Omega} C(x, t) d\Omega \quad (6-2)$$

where  $\Delta H$  is the enthalpy change for the chemical reactions,  $\Omega$  denotes the reaction region,  $T_0$  is the initial temperature and  $\beta$  is the heating rate.

The slab geometry consists of a bilayer with thickness  $L$  and periodic boundaries (i.e. an infinite number of layers). The reaction zone  $\Omega$  is every other layer of the laminate, and  $d\Omega = dz$ . With this geometry an analytical solution to Eq. (6-2) can be obtained using a Green's function<sup>[144]</sup> as

$$DSC(t) = \frac{2D(t)}{\sqrt{\pi\Theta(t)}} \left( 1 + 2 \sum_n q^{n^2} + q^{(n+1)^2} \right) \quad (6-3)$$

$$\Theta(t) \equiv \int_0^t D(t) dt, \quad q \equiv -e^{-\frac{L^2}{4\Theta(t)}}$$

where  $n$  is the order to which the analytical solution is truncated. The peak temperatures ( $T_p$ ) can be obtained by finding the temperature at which the derivative of Eq. (6-3) with respect to  $T$  is zero,

$$\left. \frac{d DSC(T)}{dT} \right|_{T_p} = \beta \left. \frac{d DSC(t)}{dt} \right|_{t_p} = 0. \quad (6-4)$$

Assuming a diffusion coefficient with an Arrhenius form  $k(T) = k_0 e^{-E_a/RT}$ , and that the activation energy for mass diffusion is much larger than the Boltzmann factor at the peak temperature ( $E_a \gg RT_p$ ), an approximate solution to Eqs. (6-3) and (6-4) can be found as

$$2 \ln \frac{E_a}{RT_p} + \frac{E_a}{RT_p} = - \ln \frac{\beta L_z^2}{\beta_0 L_z^2} + \ln \frac{E_a D_0}{\beta_0 L_z^2 R \Theta_p}. \quad (6-5)$$

In this expression  $\Theta_p$  is a constant corresponding to the laminate,  $L_z$  is the bilayer total thickness, and  $\beta_0 = 1^\circ\text{C} \cdot \text{min}^{-1}$  is a nondimensionalization factor for heating rates. Details of mathematical derivation from Eq. (6-1) and (6-2) to Eq. (6-5) are included in the Appendix.

In principle Eqs. (6-1) and (6-2) can also be solved for the cylindrical and spherical geometries using a Green's function. However, it was found that the resulting expressions are complicated and it is impractical to find a simple analytical solution to Eq. (6-2) or Eq. (6-4). Recognizing this, Eq. (6-2) and Eq. (6-4) were solved numerically using a finite difference method with various system sizes and heating rates. The resulting DSC peak temperatures fit Eq. (6-5) very well by only altering the geometry constant  $\Theta_p$ , which is 0.10, 0.54, and 0.24 for slab, cylindrical and spherical geometries, respectively. More details of these fits are given in the validation section below.

### 6.2.1 Analytical Derivation based on Diffusion Equations

In the one dimension case, the solution to Eq. (6-1) with time dependent diffusivity is well known<sup>[145]</sup>

$$C(x, t) = \frac{1}{2} \sum_{n=0}^{\infty} (-1)^n \left[ \operatorname{erf} \left( \frac{x - (n+1)L}{\sqrt{4\Theta(t)}} \right) - \operatorname{erf} \left( \frac{x - nL}{\sqrt{4\Theta(t)}} \right) \right] + \frac{1}{2} \sum_{n=0}^{\infty} (-1)^n \left[ \operatorname{erf} \left( \frac{x+(n+1)L}{\sqrt{4\Theta(t)}} \right) - \operatorname{erf} \left( \frac{x+nL}{\sqrt{4\Theta(t)}} \right) \right]. \quad (6-6)$$

Eq. (6-2) can be Further simplified by applying Gauss's theorem:

$$DSC(t) = \Delta H \int_0^L \frac{\partial}{\partial t} C(z, t) dz = 2D(t)\Delta H \left. \frac{\partial C(x, t)}{\partial x} \right|_{x=0} \quad (6-7)$$

Combining the above two equations yields Eq. (6-3). To obtain Eq. (6-5), an approximation must be made as shown in the following equation

$$\Theta(t) \approx \frac{RT^2}{\beta E_a} D(t). \quad (6-8)$$

which comes from the asymptotic expansion. This approximation results in less than a 1% error in the temperature range of  $0^\circ\text{C} < T < 1300^\circ\text{C}$  and the activation range of  $30\text{kJ/mol} < E_a < 300\text{kJ/mol}$ . Substituting this approximation into Eq. (6-3) gives

$$DSC(t) = \left( 1 - 2e^{-\frac{1}{4\Theta_t}} + e^{-\frac{1}{\Theta_t}} + \dots \right) \frac{\sqrt{\Theta_t} E_a}{RT} \quad (6-9)$$

$$\Theta_t \equiv \frac{E_a K_0}{R\beta L^2} \left( \frac{RT}{E_a} \right)^2 e^{-\frac{E_a}{RT}}.$$

To locate the DSC curve peak position,  $\xi_t$  is treated as an independent variable, and a value for  $\xi_p$  is found that makes  $DSC'(\xi_p)$  zero, and then  $T_p$  is found from  $\xi_p$ .

$$DSC'(\Theta_t) = \frac{\partial}{\partial t} \left[ \left( 1 - 2e^{-\frac{1}{4\Theta_t}} + e^{-\frac{1}{\Theta_t}} + \dots \right) \frac{\sqrt{\Theta_t} E_a}{RT} \right] \approx \frac{\partial}{\partial t} \left[ \left( 1 - 2e^{-\frac{1}{4\Theta_t}} + e^{-\frac{1}{\Theta_t}} + \dots \right) \sqrt{\Theta_t} \right] \cdot \frac{E_a}{RT} \quad (6-10)$$

An approximate is made here because  $E_a/RT$  always changes slowly compared to  $\Theta_t$  and therefore it can be viewed as a constant in the derivatives. The root of the above equation is independent of any system parameters can be found numerically as:

$$\Theta_p \approx 0.10 \quad (6-11)$$

This equation together with the definition of  $\xi_t$  can predict peak temperatures as is given in Eq. (6-5).

### 6.2.2 Derivation based on the Isoconversion Assumption

Although the detailed derivation shown above from the Fick's diffusion Eq.(6-1) through Eq. (6-5) is critical for understanding the approximations leading to Eq. (6-5), it is often too complicated to apply the same derivation to arbitrary geometries involving complicated kinetics. On the other hand, many empirical or semi-empirical kinetic functions (e.g  $f(\alpha)$  and  $g(\alpha)$  discussed above) have been proposed over the past decades<sup>[90], [127], [131], [132], [137], [146], [147]</sup>. Starting from one-dimensional controlled kinetics in a slab geometry, it is shown in this subsection how the geometric dependence can be derived from those kinetic functions despite many of them originating from uncertain assumptions.

It is well established<sup>[148]</sup> that the rate equation for an infinite flat plane follows the parabolic law

$$l^2 = kt \quad (6-12)$$

where  $l$  is the thickness of the product layer and  $k$  is an effective kinetic constant that is assumed to follow Arrhenius behavior  $k = k_0 \exp(-E_a/RT)$ . Derivatives of Eq.(6-12) with respect to time give

$$2l dl = k_0 e^{-\frac{E_a}{RT}} dt = k_0 e^{-\frac{E_a}{RT}} \frac{dT}{\beta}. \quad (6-13)$$

Integrating the two sides, applying the KAS approximation<sup>[134]</sup> and taking the natural logarithm results in the expression

$$2 \ln \frac{E_a}{RT} + \frac{E_a}{RT} = - \ln \frac{\beta L^2}{\beta_0 L_z^2} + \ln \frac{E_a k_0}{\beta_0 L_z^2 R}. \quad (6-14)$$

Eq. (6-14) is very similar to Eq. (6-5) except that Eq. (6-14) describes the dynamic balance between the thickness of the intermixing layer and the system temperature. Furthermore, if isoconversion is applied, which assumes that DSC curves always reach peaks at a fixed state of transformation<sup>[137], [147]</sup>,  $l = \alpha L$  when  $T = T_p$ . The resulting Eq. (6-15)

$$2 \ln \frac{E_a}{RT_p} + \frac{E_a}{RT_p} = - \ln \frac{\beta L^2}{\beta_0 L_z^2} + \ln \frac{E_a k_0}{\beta_0 L_z^2 R \alpha^2} \quad (6-15)$$

is almost the same as Eq. (6-5) except for small difference in the pre-exponential term, which indicates that the rate constant  $k$  in Eq. (6-12) is related to the inter-diffusion coefficient  $D$  by  $k = \alpha^2 D / \Theta_p$ .

Compared to the analysis in the previous section, the derivation based on an empirical kinetic function is much easier, although the predicted kinetic constant is not well defined. Under the isoconversion assumption, the analysis is applicable to other kinetic systems. For example, the kinetic function for interface controlled reactions is described by Eq.(6-16)<sup>[127]</sup>

$$\frac{dl}{dt} = k_0 e^{-\frac{E_a}{RT}}. \quad (6-16)$$

This is an empirical function describing the reaction in flat plane systems<sup>[90]</sup>. Performing operations similar to those above result in the expression

$$2 \ln \frac{E_a}{RT_p} + \frac{E_a}{RT_p} = - \ln \frac{\beta L}{\beta_0 L_z} + \ln \frac{E_a k_0}{\beta_0 L_z^2 R \alpha}, \quad (6-17)$$

which predicts that peak temperature is a function of combined factor  $\beta L$  instead of  $\beta L^2$  as predicted by the parabolic law.

### 6.2.3 Thermal Conduction Modeling

In Eq. (6-2), temperature is assumed to increase linearly with time during the calorimetric scanning experiments. While this is true for ideal DSC experiments, for DTA experiments it is the heat flow to both the sample and the reference material that is constant. Temperature differences between the two are recorded and thermal input/output is computed. Hence, the temperature of the reference material increases linearly with time whereas the temperature of the sample increases non-uniformly throughout the experiments. To probe how the inclusion of heat exchange with the environment will affect the DSC curves as well as temperature profiles of the sample material, we introduce the following equation

$$C_p^s \frac{\partial T}{\partial t} = \kappa_{TC}(\beta t + T_0 - T) + DSC(t) \cdot C_0 \Delta H, \quad (6-18)$$

which gives the energy change in the sample material  $C_p^s \partial T / \partial t$  as the sum of the heat conduction  $\kappa_{TC}(\beta t + T_0 - T)$  and the heat generated from the reaction  $DSC(t) \cdot C_0 \Delta H$ . In these equations  $C_p^s$  ( $\text{kJ m}^{-2} \text{K}^{-1}$ ) is the heat capacity per unit area,  $\kappa_{TC}$  ( $\text{kJ m}^{-2} \text{s}^{-1} \text{K}^{-1}$ ) is the heat conductance,  $C_0$  is the initial concentration of diffusant, and  $\Delta H$  is the reaction enthalpy.

Eq. (6-18) is a first-order linear inhomogeneous ordinary differential equation. Its solution with initial condition  $T(0) = T_0$  is

$$T(t) = T_0 + e^{-\alpha_{TC} t} [\alpha_{TC}^{-1} \beta e^{\alpha_{TC} t} (\alpha_{TC} t - 1) + \alpha_{TC}^{-1} \beta] + e^{-\alpha_{TC} t} \int_0^t DSC(t') \cdot C_0 \Delta H e^{\alpha_{TC} t'} dt' \quad (6-19)$$

where  $\alpha_{TC} = \kappa_{TC} / C_p^s$  ( $[\text{s}^{-1}]$ ) is the heat conduction rate. In this temperature profile  $T(t)$  is a functional of  $DSC(t)$  which in turn is dependent on temperature profile.

### 6.3 Model Applications and Validation

The equations derived in the last section are used to analyze QCM data for a nano-laminate thermite and aluminide, where we show that the geometry scaling not only reduces the scatter in the activation energy but also gives new insight into kinetic mechanisms leading to energy release. We also characterize the model in terms of DSC peak shape, and validate the geometry factors for modeling multi-layer cylindrical and spherical geometries.

#### 6.3.1 Nano-Laminate Zr – CuO and Al – CuO Thermite

The experimental details regarding the synthesis and characterization of this system are given elsewhere, and so only a relatively brief description is given here.<sup>[106]</sup> Multiple layers of thermite reactants were deposited in an alternating geometry on C plane Sapphire by physical vapor deposition using dual beam magnetron sputtering sources positioned 180° from each other. Deposition rates were determined by X-Ray reflectivity. This process produces very sharp and relatively flat interfaces as characterized with TEM. The overall thickness of the sample was kept constant at (1088nm for Zr – CuO and 1069nm for Al – CuO) while the number of bi-layers was varied from 1 to 5. The thickness of a metal layer was kept proportional to its neighboring oxide layer so that the molar amounts of redox agents were balanced. The samples were characterized by constant heat flow DSC under Argon in a temperature range from 100°C to 1200°C at five different heating rates of 5, 10, 15, 20 and 25 °C min<sup>-1</sup>. For each sample a baseline was established by a second ramp done at the same heating rate and to the same final temperature. The temperature at which the first exothermic maximum was reached was recorded and is given in Table 6.1.

Table 6.1: Temperatures of the first DSC peaks measured for a Al/CuO and Zr/CuO nanolaminate

Heating Rate (°C/min)	1 <sup>st</sup> DSC peak temperatures (°C)									
	Zr – CuO					Al – CuO				
	1BL	2BLs	3BLs	4BLs	1BL	2BLs	3BLs	4BLs	5BLs	
5	436.0	371.5	340.2	333.0	908.5	866.1	807.3	794.7	908.5	
10	453.1	392.7	364.1	362.0	957.4	893.6	828.1	821.9	957.4	
15	462.5	453.4	378.6	365.0	949.0	905.5	856.3	821.4	949.0	
20	428.1	440.7	402.3	369.6	967.1	929.2	874.6	868.0	967.1	
25	496.7	406.1	409.0	377.1	983.5	917.4	856.3	839.5	983.5	

Shown in Figure 6.2A and Figure 6.3A are the Zr/CuO data and Al/CuO from Table 6.1 plotted according to Kissinger plot. <sup>[130], [134], [149]–[151]</sup>, i.e. Eq. (3-9) The solid lines are fits to the data for each set of bilayers (the columns of Table 6.1). There is considerable scatter in the data, with the slopes of the lines giving effective activation energies between 39 and 108 KJ/mole. Shown in Figure 6.2B and Figure 6.3B are the same data plotted according to Eq.(6-5). Plotted this way, which accounts for different layer thicknesses, the scatter in the data is significantly reduced, and the data are well described by a single line. The slope and intercept from a least squares fit to the data (the solid line in the plot) yields an activation energy of 73.5 kJ/mole and a prefactor  $D_0$  of  $4.58 \times 10^{-11} \text{ m}^2/\text{s}$  for Zr/CuO composite and an activation energy of 122.1 kJ/mole and a prefactor  $D_0$  of  $8.73 \times 10^{-11} \text{ m}^2/\text{s}$  for Al/CuO system.

$$\ln\left(\frac{\beta}{T_p^2}\right) = \ln\left(\frac{AR}{E_a}\right) - \frac{E_a}{RT_p} \quad (6-20)$$

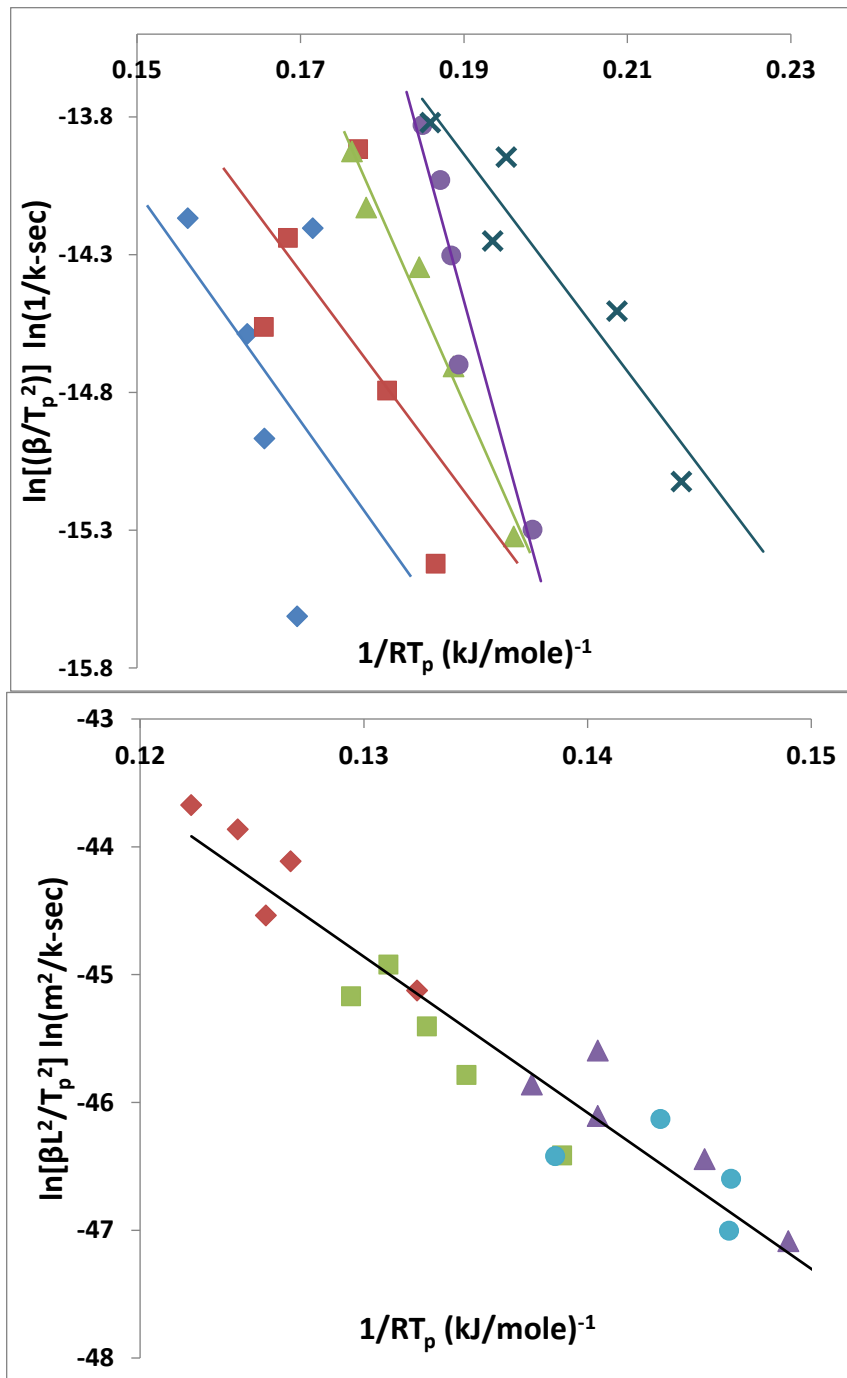


Figure 6.2: Plots of the Zr/CuO data in Table 6.1. (A) Given as a Kissinger plot, *i.e.* Eq. (3-9). (B) Plotted via Eq.(6-5). Diamonds, squares, triangles, circles and ×'s correspond to 1-5 bilayers, respectively

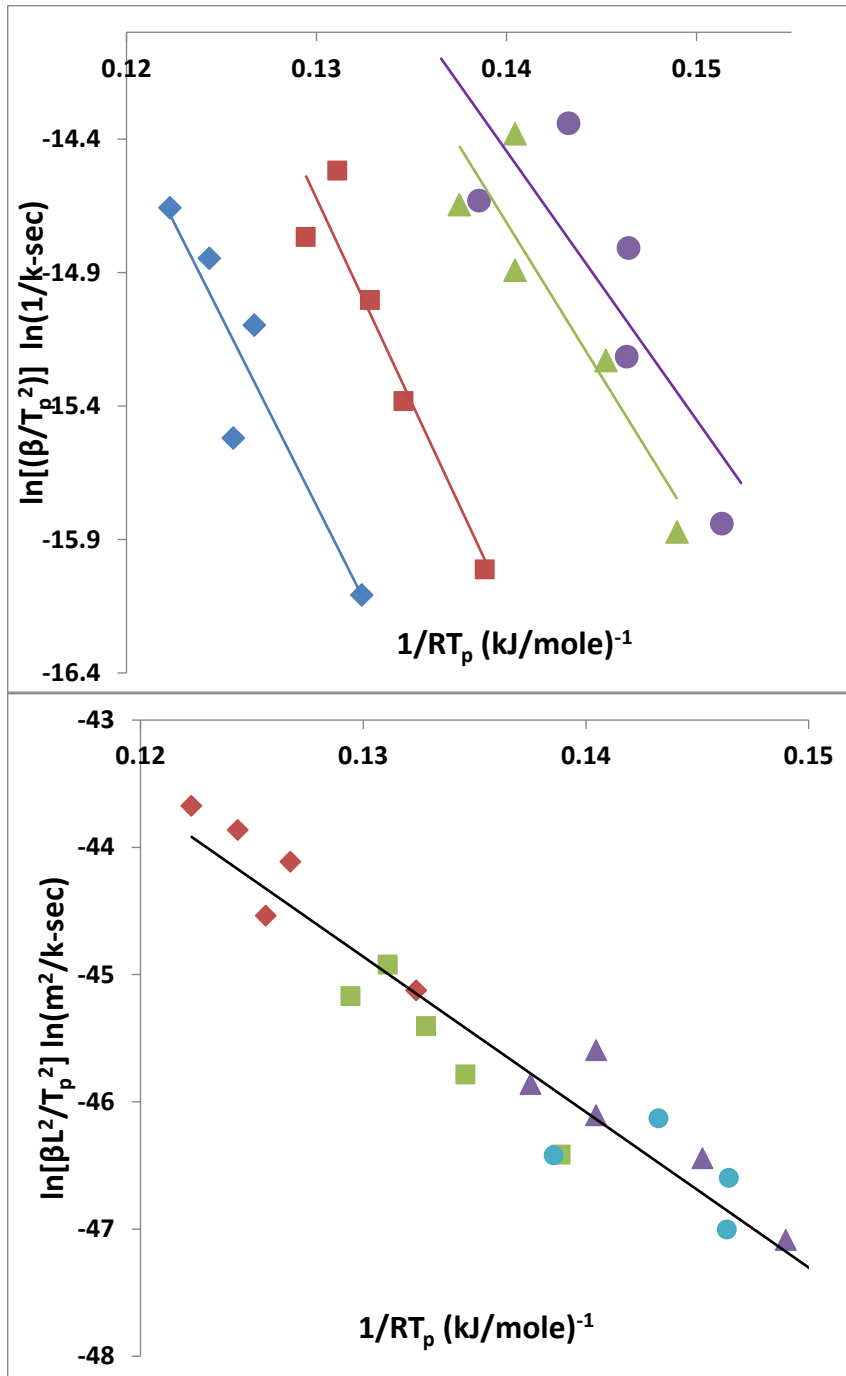


Figure 6.3: Plots of the Al/CuO data in Table 6.1. (A) Given as a Kissinger plot, *i.e.* Eq.(3-9). (B) Plotted via Eq.(6-5). Diamonds, squares, triangles and circles correspond to 1-4 bilayers, respectively.

Plotted in Figure 6.4 as the thick solid line is the diffusion coefficient predicted from the plot in Figure 6.2B over the temperature range at which the peak temperatures were measured. The thinner solid lines and the open diamonds are experimental data for self-diffusion of oxygen in Zr<sup>[152]–[156]</sup>, while the dashed and dotted lines correspond to experimental data for oxygen self-diffusion in ZrO<sub>2</sub> and in CuO, respectively<sup>[157]–[160]</sup>. The length of the lines corresponds to the temperature region over which the measurements were taken. The effective rate from analysis of the DSC data is closest to that for oxygen diffusion in zirconium, although the slope (and hence activation energy) is not well matched to O in Zr.

There are several possibilities for why the DSC rates do not appear to match this self-diffusion data, including the assumption of a constant diffusion coefficient in our model for the diffusion of the reacting species throughout the system, the heating or dynamics specific to the reaction, or large concentration gradients that create driving forces that are different from those leading to self-diffusion. Nonetheless it is reasonable to assume that mass diffusion is the rate limiting step to this nano-thermite reaction under DSC conditions based on the scaling behavior with system geometry.

In addition to the temperature at the maximum in the first DSC peak, the model can be analyzed in terms of peak shape. Plotted in Figure 6.5 as the dotted lines is a set of experimental DSC curves for different numbers of bi-layers for Zr-CuO nanolaminates at a heating rate of 5K/min for each sample. The curves have been offset along the y axis for clarity. Plotted as the solid lines are the curves given by Eq.(6-3) with the sum in Eq. (6-3) fully converged. The filled circles indicate the peak positions used to help fit the kinetic data

in Eq.(6-17), and the thick dashed curve shows the fit to those temperatures. For three bi-layers the experimental and model peak shapes matches reasonably well. However, for fewer bi-layers the experimental peak is sharper than the model, while for more bi-layers the experimental peaks are broader than the model. There also higher-temperature peaks in the experimental DSC peaks that are not part of our model.

To better understand the origin of the discrepancy between experimental peak shapes and those given by Eq.(6-3), a set of numerical calculations were carried out to explore the influence of heat transfer on the peak shape. These were carried out by solving Eqs.(6-1), (6-2) and (6-18) iteratively. Given the initial guess of temperature profile as  $T^{(0)}(t) = \beta t + T_0$ , the  $DSC(t)$  curve is calculated from Eq. (6-3). The resulting  $DSC(t)$  profile is then substituted into Eq. (6-19) to update the temperature profile. This is repeated until the temperature profile converges so that the stable temperature profile satisfies both Eq. (6-3) and (6-19).

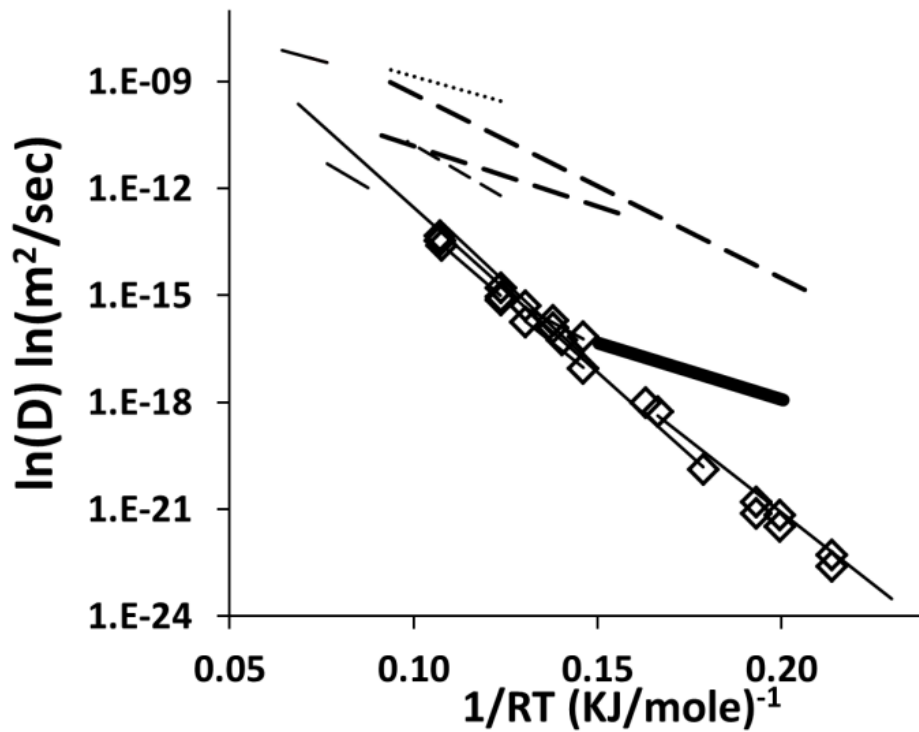


Figure 6.4: Natural logarithm of diffusion coefficient as a function of the inverse of the temperatures times Boltzmann's constant. The thick solid line is the diffusion coefficient predicted from the plot in Figure 2B over the temperature range at which the peak temperatures were measured. The thinner solid lines and the open diamonds are experimental data for self-diffusion of oxygen in  $Zr^{[152]-[156]}$ ; dashed and dotted lines correspond to experimental data for oxygen self-diffusion  $ZrO_2$  and in  $CuO$ , respectively<sup>[157]-[160]</sup>. The line lengths correspond to the temperature over which the measurements were taken.

This iterative algorithm does not always converge. For example, the temperature profile will diverge if the heat conductance is under-estimated. This is reasonable because the rate of heat accumulation grows exponentially with the sample temperature while the rate of heat dissipation only scales linearly. In the extreme adiabatic case, thermite combustion is

likely to take place rather than slow reaction. On the other hand, the  $DSC(t)$  curve is not significantly changed with very high heat conductivity.

Plotted in Figure 6.6 are numerically-calculated peak shapes for a five bi-layer system and heating rate 5K/min. The heat capacity and reaction enthalpy were taken from the JANAF tables<sup>[161]</sup> and four different values of heat conductance  $\kappa_{TC}$  were used in addition to the analytic model. From the plot it is clear that peak shape is a strong function of the degree of heat transfer, which for the analytic model is essentially infinite (i.e. the temperature follows the programmed heating). Hence it is not surprising that the analytic model does not reproduce experiment peak shapes. On the other hand, the peak position varied only about 12°C between the analytic model and the lowest thermal conductance. Hence neglecting heat conductance does not appear to significantly change the kinetic data derived from this model.

Table 6.2: DSC peak temperatures as a function of heating rate and bilayer thickness for Ni – Al bimetallic multilayer system

<i>Heating Rate</i> (K/min)	<i>1<sup>st</sup> Peak Temperatures <math>T_p</math>(K)</i>				
	<i>L=20nm</i>	<i>L=40nm</i>	<i>L=80nm</i>	<i>L=160nm</i>	<i>L=320nm</i>
20	496.9	503.2	514.4	525.8	541.0
40	506.8	513.6	525.6	534.7	552.4
80	516.4	526.3	534.5	547.0	564.5
160	526.1	538.8	544.9	557.6	578.2

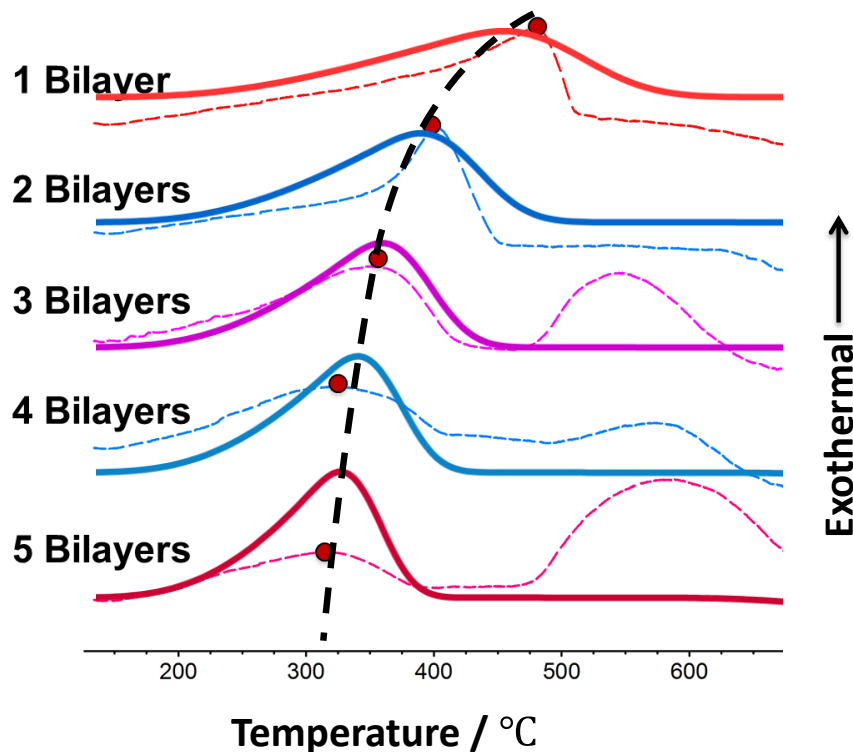


Figure 6.5: DSC curves for a Zr-CuO nano- laminate for different numbers of bi-layers. Dotted lines are experimental data; the solid lines are from Eq.(6-3). The curves are offset along the y axis for clarity. The points are used to determine the diffusion kinetics, while the dotted line represents the fit of Eq.(6-5) to the experimental data.

### 6.3.2 Interpretation of Kinetics in a multi-layer Ni/Al Aluminide

Similar to thermite systems, multi-layer aluminides are comprised of alternating two-dimensional layers of aluminum metal and one other metal such as Ni, Ti, Mo and Zr. Heat is released by inter-diffusion and alloy formation, or by the formation of more stable phases as temperature is increased. Barmak, Michaelson and Lucadamo used DSC to study reactions in sputter-deposited Ni/Al multi-layer films.<sup>[89]</sup> In their studies a 1:3 molar ratio of Ni/Al was maintained, with periodicities ranging from 320 nm down to fully co-deposited films.

Using x-ray diffraction, DSC, electrical resistivity measurements and transmission electron microscopy, they concluded that reactions of Ni and Al form either an ordered or amorphous NiAl phase at the inter-lamella interfaces during deposition for all thicknesses. For films with modulation periods smaller than about 20 nm, they observed a single peak in the DSC with a temperature at the peak maximum that is independent of layer thickness. For larger film modulations a second peak was observed at a higher temperature, and the temperatures at both peak heights increased with increasing layer thickness. For both peaks, the authors used a Kissinger analysis for each modulation size above 20 nm to determine activation energies for the processes contributing to reaction. The resulting activation energies for each layer thickness for the first peak showed considerable scatter, and ranged from 1.25-1.55 eV, with no apparent correlation to modulation size.

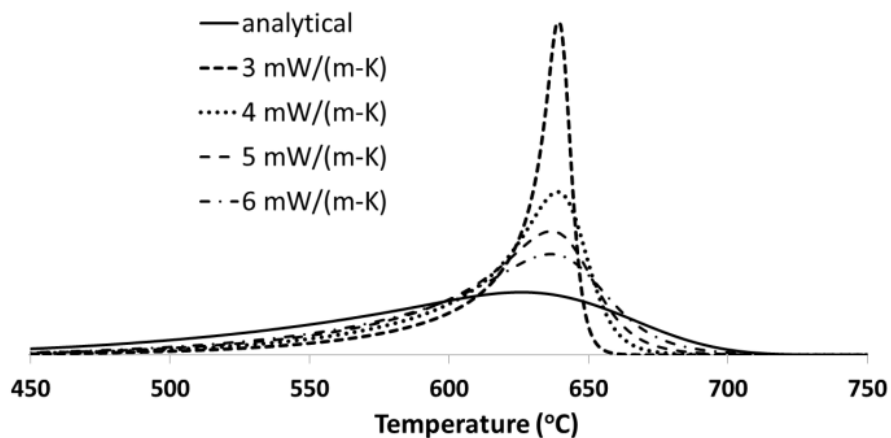


Figure 6.6 Peak shape calculated from Eq.(6-19) for different values of thermal conductance.

The peak temperatures for the first DSC peak for different modulations sizes for these systems, which were read from the Fig. 8 in reference <sup>[89]</sup>, are shown in the Table 6.2. Plotted in Figure 6.7a and b is this data scaled according to Eq. (6-5) and Eq. (6-17), respectively. For the former the data falls on separate curves, while for the latter all of the data falls on a single curve. This indicates that in this Ni – Al system the reaction captured by the 1<sup>st</sup> peak of in the DSC traces is governed by the linear growth law as described by Eq. (6-17) rather than diffusion controlled kinetics as described by Eq. (6-5). This is consistent with the analysis of Barmak, Michaelson and Lucadamo, who interpreted their growth kinetics in this regime as being a planar phase transition that is heterogeneously nucleated all along the interface, as opposed to homogeneous nucleation within the layers. This conclusion could not be made from a traditional Kissinger analysis. The data scaled as in Figure 6.7b also reduces the scatter in the data, and allows an activation energy to be determined with less statistical uncertainty. This rescaling yields an activation energy of 1.50 eV, which is slightly higher than the average value of 1.42 eV given in reference <sup>[89]</sup>.

### 6.3.3 Cylindrical and Spherical Systems

It was stated above that Eq.(6-5), which was derived for a laminate structure, could be equally well applied to cylindrical and spherical geometries if a different geometry factor is used. To explore the extent to which this approximation holds, we compared the analytic prediction of Eq. (6-5) with the proper geometry factors to DSC data generated for multi-layer nano-wires and nano-particles by numerically solving Eq. (6-1), (6-2) and (6-4) for

these respective structures along the radial direction. Calculated data was used because of the lack of suitable experimental data for systems of this type.

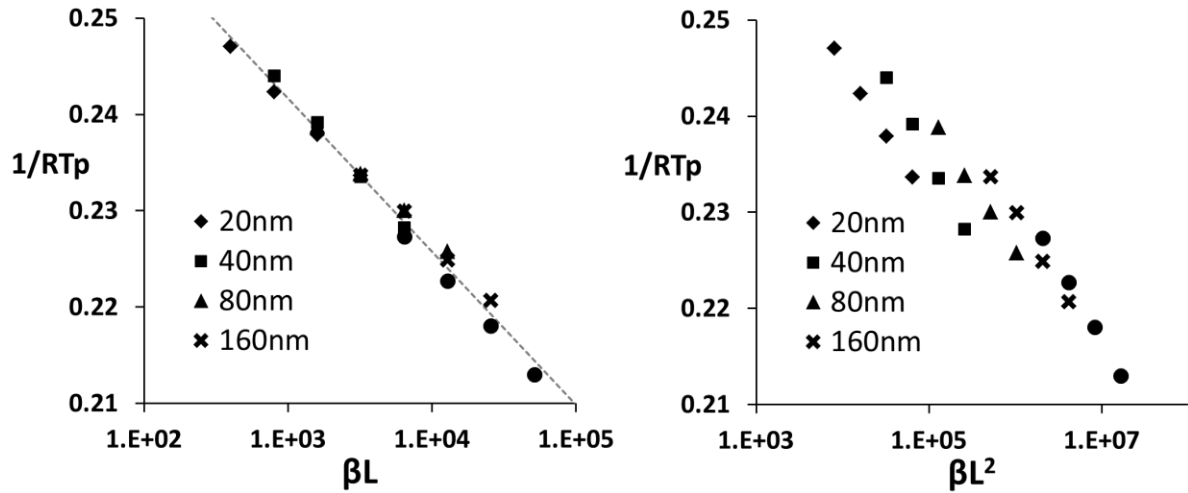


Figure 6.7: Plot of data from Table II. (a) Scaled according to Eq. (6-5). (b) Scaled according to Eq. (6-17).

Plotted in Figure 6.8 is the inverse of the calculated peak temperatures as a function of the scaling factor  $\beta L^2$  (on a logarithmic scale) as suggested by Eq. (6-5). Two sets of activation energies and pre-exponential constants for the diffusivity were used,  $E_a = 50 \text{ kJ/mol}$ , and  $D_0 = 2 \times 10^{-13} \text{ m}^2/\text{s}$ , and  $E_a = 300 \text{ kJ/mol}$  and  $D_0 = 1 \times 10^{11} \text{ m}^2/\text{s}$ . The data include radii of 250-1000 nm, bi-layer sizes of 1, 2, 3, and 4, and heating rates heating of 5, 10, 15, 20 and 25 °C/min. The numerical results scale reasonably linearly on this plot for all geometries and both sets of diffusivity parameters, and the slopes of these lines were used to determine the geometry factors  $\Theta_p$  given above. As stated above, although

Eq.(6-5) was derived for laminar geometries, it appears to work well for other geometries with an appropriate geometry factor.

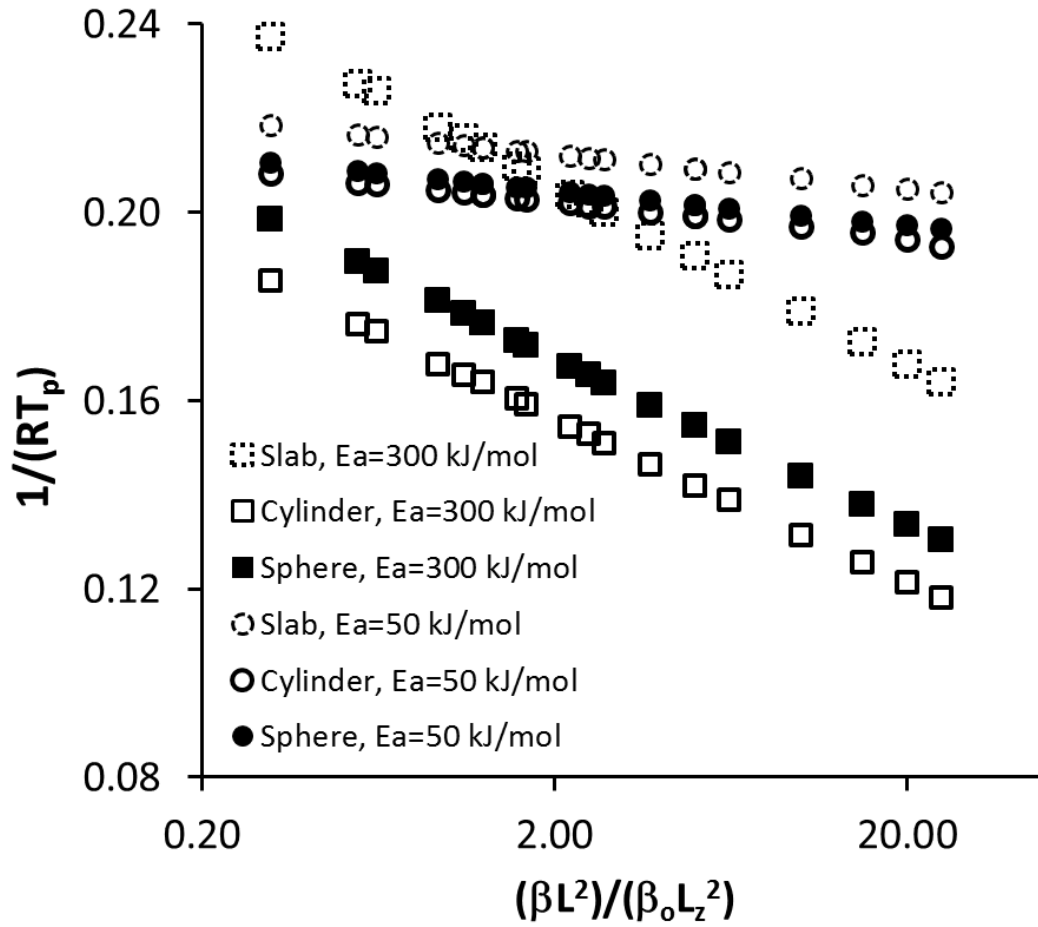


Figure 6.8: Plot of data from numerical DSC curves for laminar, cylindrical and spherical multilayer systems scaled as given by Eq.(6-5).

## 6.4 Conclusions

A new expression is derived for DSC curves for solid-state reactions with diffusion controlled kinetics. Based on Fick's diffusion equation, the new form is used to derive an analytic expression for the temperature at the maximum peak height that is similar in form to a Kissinger analysis, but that explicitly takes into account the system geometry. It was found that this expression, which was derived for laminar geometries with alternating initial compositions, is also applicable to cylindrical and spherical multi-layer geometries with an appropriate change in a geometry constant.

The new expression was used to analyze two reactive multi-layer nano-laminate systems, a Zr/CuO thermite and an Al-Ni aluminide. In both cases an appropriate scaling of DSC peak temperatures by layer thickness yielded activation energies that fall on a single line, and that have values that can be derived with a higher level of precision than those determined from a traditional Kissinger analysis. The for nano-laminate thermite the data scaled with the square of the bi-layer thickness, while for the aluminide the data scaled with the thickness, suggesting two different types of underlying kinetics.

The peak shape given by the analytic expression as well as numerical solutions to the kinetic equations was characterized as a function of the degree of heat dissipation. It was found that although the peak shape is highly sensitive to heat dissipation, the temperature at the peak height is not a strong function of heat dissipation. This helps establish the limitations of this expression in terms of describing DSC data.

## Chapter 7 Simulation of Electric Ignited Self-Propagating Reaction in Nano Thermites based on Diffusion-Controlled Kinetics

### 7.1 Introduction

As discussed in the Chapter 5.3.1, the conventional way of modeling self-propagating reactions in energetic materials include mainly heat and mass diffusion. However, this approach has some apparent drawbacks:

8. It is isolated from DSC/DTA analysis. In conventional thermal analysis, reactions are controlled by a linear rising temperature. The maximum sample temperature is usually below the melting temperatures of the comprising components and the rising rate is normally below 1 °C/s. Hence the reaction rates are usually moderate and can be modeled by empirical functions as summarized in Table 5.4. In contrast, in the studies of self-propagating reactions, the maximum temperature is normally higher than the melting temperature of any comprising components and the local temperature rising rate can be as high as  $10^5 - 10^7$  °C/s<sup>[96]</sup>. How to build a model that is consistent with both cases is still an unsolved challenge.
9. Despite many research efforts in simulating self-propagating reactions in NEMs, only in very few cases has particular attention been given to the reaction mechanisms at the level of nano thin films. From a chemical viewpoint, the major criticism of the commonly accepted approach is its oversimplified account of the chemical kinetics. As a matter of fact, multistep mechanisms are clearly suggested by experimental results.

10. A major issue plaguing both the understanding of the self-propagating reaction mechanisms and the practical use of NEMs is that the method of sample preparation often plays a large role in the observed reactivity. Even with the same technique, sample-to-sample variations may be significant enough to alter the reactivity. These issues have led to the needs for better ways to describe micro-mechanisms of thermite reactions.

In this chapter, computer simulations find use in two ways. First of all, a comprehensive computer simulation model that includes various process parameters is presented. Parameters can be determined according to experimental data, and the trained model can then be utilized to predict physical/chemical properties of NEM samples with diverse initial structures. This can help unveil how the initial design of NEMs affects each kinetic process and how it acts on the overall reactions. Then proper designs of NEMs can be constructed by computer simulations to tailor the mass transport and energy release.

Second, micro mechanisms of thermite reactions are still controversial. For example, no conclusions have been made for the questions that which of the two process, the metal diffusion to the oxides or the oxide diffusion to the metal, dominates thermite reactions. Answers to the question are likely different under different situations. In our study, competition among various mechanisms are summarized in a comprehensive model with various process parameters that can be trained by experimental physical/chemical properties, such as Differential Scanning Calorimetry (DSC) curve, of well-structured NEMs. Resulting parameters can qualitatively characterize the interaction among all dynamic processes.. In

this research, details of the numerical model are reported and corresponding results are present to show how computer simulations aid the design of NEMs materials.

## **7.2 Electric Ignition Experiments and Setups of Numerical Simulations**

Synthesis details of laminated structures were given in the section 6.3.1 and elsewhere<sup>[102]</sup>, and so only a relatively brief description is given here. Multiple layers of thermite reactants were deposited in an alternating geometry, and cut to 1cm × 1cm to ensure comparison of equal amounts of reactants. To enable electric ignition, platinum conductors were introduced either on the two sides of the laminates, as illustrated in the Figure 7.1a, or embedded in the surface of the laminates, as shown in Figure 7.1b. A constant electric potential ( $V_0 = 0.1$ ) was applied on the two Pt conductors on the two sides of the laminates or along the Pt wire on top of the laminates.

Three distinctive numerical simulations were carried out in this research. The three examples described have significantly reduced the computational burden by mapping nano-laminate dynamics to two dimensions. Further studies will emphasize similar mappings where appropriate, as well as fully three-dimensional systems where needed.

Illustrated in the figure below are three example sets of numerical simulations, one that treats the X-Y cross sections and the other two treat X-Z cross sections. Formulations of each models are presented in the following three subsections and results are given and discussed in the next sections.

The details and general results of the two simulations are presented in the Figure 7.1.

### 7.2.1: On interface parallel planes

In this scheme, a set of coupled partial differential equations and associated numerical solver was developed to model nano-laminate reactivity at the continuum level. As detailed below, this simulation incorporates electrostatics, Joule heating, energy dissipation, mass transport, melting and chemical dynamics.

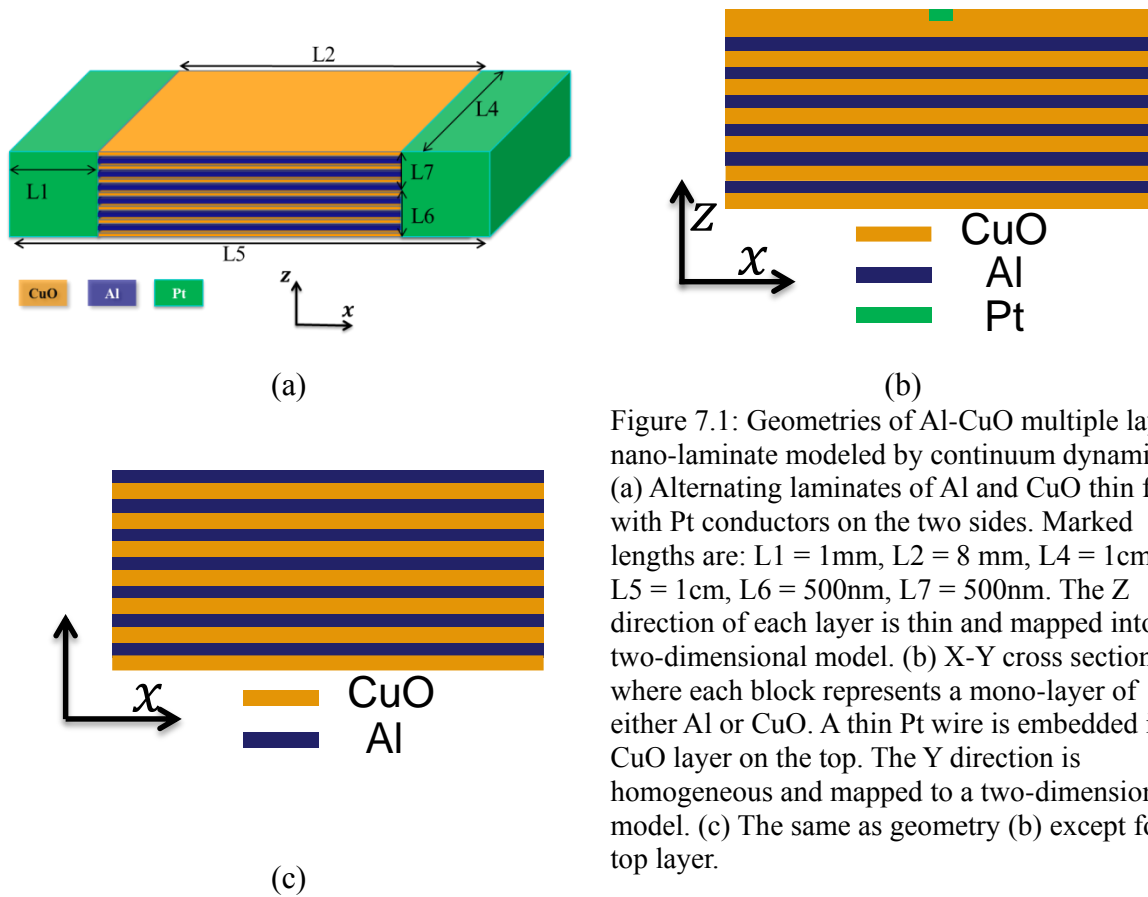


Figure 7.1: Geometries of Al-CuO multiple layer nano-laminate modeled by continuum dynamics. (a) Alternating laminates of Al and CuO thin foils with Pt conductors on the two sides. Marked lengths are:  $L1 = 1\text{ mm}$ ,  $L2 = 8\text{ mm}$ ,  $L4 = 1\text{ cm}$ ,  $L5 = 1\text{ cm}$ ,  $L6 = 500\text{ nm}$ ,  $L7 = 500\text{ nm}$ . The Z direction of each layer is thin and mapped into a two-dimensional model. (b) X-Y cross section where each block represents a mono-layer of either Al or CuO. A thin Pt wire is embedded in a CuO layer on the top. The Y direction is homogeneous and mapped to a two-dimensional model. (c) The same as geometry (b) except for top layer.

Due to the symmetry along the z direction, the reactive models were restricted to two dimensional Cartesian coordinates to reduce the computational burden. Two layers that correspond to metal and copper oxide were included in the system. Energy flow across the two layers is described by the heat conduction law

$$\dot{Q}_{T,C} = \kappa_{T,C} \Delta T \quad (7-1)$$

where  $\dot{Q}_{T,C}$  is the heat conduction rate,  $\kappa_{T,C}$  is the interfacial thermal conductance and  $\Delta T$  is the temperature drop between the two layers.

Other processes such as Joule heating, mass and heat transport (Fourier and Fick laws) chemical reactions and phase transformations (melting) are described by in-plane partial differential equations. For example, in-plane heat transport is assumed to follow Fourier's law:

$$\rho_m C_{p,m} \frac{\partial T}{\partial t} - \nabla \cdot (\kappa_T \nabla T) = \dot{Q}_{T,C} + \dot{Q}_r + \dot{Q}_m + \dot{Q}_e \quad (7-2)$$

where  $\rho_m$  is the mass density,  $C_{p,m}$  is the specific heat capacity per unit mass,  $\kappa_T$  is the thermal conductivity, and  $\dot{Q}_r$  is the heat generation rate from chemical reactions. The latter quantity has a positive value for exothermal reactions and a negative value for endothermic reactions.  $\dot{Q}_m$  represents the heat change rates by phase transition, in our case, melting.  $\dot{Q}_e$  is the heat generation rate due to joule heating which is described by:

$$\dot{Q}_e = \mathbf{J}_e \cdot \mathbf{E} = (\sigma_e \mathbf{E}) \cdot (\mathbf{E}) = \sigma_e |\nabla \varphi_e|^2 \quad (7-3)$$

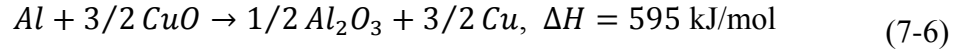
where  $\mathbf{J}_e$  is the electric current density,  $\mathbf{E}$  is the electric field strength,  $\sigma_e$  is the conductivity of the conductor and  $\varphi_e$  is the electric field potential. The conductivity is taken as a function of spatial coordinates and temperature as

$$\sigma_e = \frac{1}{\rho_e} = \frac{1}{\rho_{e0}[1 + \alpha_{e0}(T - T_{e0})]} \quad (7-4)$$

where  $\rho_e$  is the electric resistivity of the conductor and  $\rho_{e0}$  is the resistivity at reference temperature  $T_{e0}$ . The parameter  $\alpha_{e0}$  is an empirical parameter fitted to experimental data. According to Maxwell's equation, the electric potential field follows Laplace's equation

$$\nabla(-\sigma_e \nabla \varphi_e) = 0 \quad (7-5)$$

Thermite reactions are taken into account in different forms depending on the reaction stoichiometry. For example, the cupric thermite reaction with pure aluminum is



In our calculation, the extent of reaction is calculated from  $f_{v,Al}$ , which describes how much volume fraction of Al is been reacted. The heat generation rate from reaction can then be computed as

$$\dot{Q}_r = \dot{\xi} \cdot \Delta G_f = \frac{\rho_{m,Al} \dot{f}_{v,Al}}{M_{Al}} \Delta G_f \quad (7-7)$$

In addition, the reaction rate of Eq. (7-1) is assumed to follow an Arrhenius law

$$\dot{\xi} = A e^{-\frac{E_a}{RT}} \quad (7-8)$$

where  $E_a$  and  $A$  are the activation energy and pre-exponential, respectively. Unless known from other sources, these are taken as parametric quantities in our modeling.

Similar to chemical reactions, melting of a substance  $\alpha$  is described by  $f_{l,\alpha}$ , the fraction of liquid phase to total substance. In general

$$\tilde{\rho}_{m,\alpha} \Delta H_{m,\alpha} \dot{f}_{l,\alpha} = \dot{Q}_{m,\alpha} \quad (7-9)$$

where  $\tilde{\rho}_{m,\alpha} \equiv f_{v,\alpha} \rho_{m,\alpha}$  and  $\Delta H_{m,\alpha}$  are the effective mass density and the enthalpy change of melting of substance  $\alpha$ , respectively.

Periodic boundary conditions for  $y = 0$  and  $y = L_4$  were used. Fixed boundary conditions for temperature and electric potential at  $x = 0$  and  $x = L_5$  were used, i.e.

$$\begin{aligned} T|_{x=0} &= T|_{x=L_5} = 0 \\ \varphi|_{x=0} &= 0, \quad \varphi|_{x=L_5} = 0.1 \end{aligned} \quad (7-10)$$

Free surface boundary conditions for all other variables and other boundaries were used, e.g.

$$\left. \frac{\partial \varphi}{\partial x} \right|_{x=0, L_5} = 0.$$

Equations (7-1) - (7-10) define a complete set of partial differential equations that are being investigated by numerical simulation.

### **7.2.2: Simulation along the Interface Perpendicular Plane**

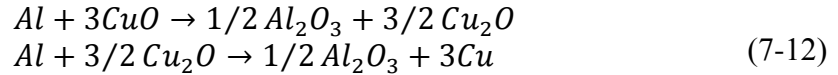
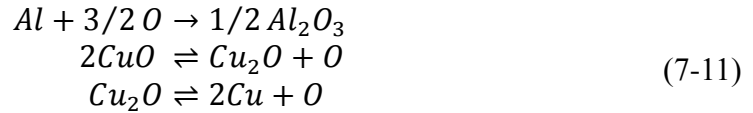
Different from the first set of simulations, simulations on the XZ plane has allowed us to model mass and energy transport across alternative layers. This emphasizes the following aspects:

11. It is able to deal simultaneously with different mechanisms and further can be used to determine if (and where) there is a rate limiting step. For example, competition between oxygen and metal ion transport can be quantified;
12. Instead of only two layers, this simulation can model any arbitrary arrangement of the laminate structure. Therefore the factor of specific interface area can be taken into account.
13. In this configuration anisotropy is considered. More specifically, coordinates in the Z direction are discretized such that each grid point corresponds to one atomistic layer. This allows chemical reactions between atomistic layers to be treated differently from

chemical reactions happening in the bulk. More Details are given in discussion of reaction (7-12) in the following.

Step functions of mole density of different substances are used to represent laminate structures. For example,  $n_{Al}(x, z)$  describes how many moles of pure Aluminum per unit area is in the X-Z plane, i.e. the dimension of  $n_{Al}$  is mole/m<sup>2</sup>. Furthermore, many processes are incorporated in this simulation. In addition to the general conservation law of mass and energy, those processes can be categorized into three groups.

(i) Chemical Reaction: Take cupric thermite reaction with pure aluminum as an example. It includes three elementary reactions, considered in Eq. (7-11), and two phenomenological reactions, as given in Eq. (7-12).



where the two direction harpoon symbol denotes reversible reactions while single direction refers to non-reversible reactions. Eq. (12) is not simply the linear combination of Eq. (7-11). This is because we assume that reaction (12) only happens between two atomistic layers through surface reconstruction other than ion transport as Eq. (7-11).

(ii) Ion transport: In this model all aluminum, copper and oxygen ions are considered as mobile. Flick's law is used to describe ion transport phenomenon with diffusivities taken from the Kakusan database<sup>[158]</sup>.

(iii) Heat transfer and phase transformation: The same as in the other configuration, melting of all substances is considered. In contrast, however, anisotropic heat transfer is treated along the X and Z directions. This is because discretization along the Z direction is at the atom scale. Continuous thermal transport laws, such as Fourier's law, are no longer applicable. Instead we assume that energy flow across the atomistic layers follows the thermal conductance law as described in Eq. (7-1) and the thermal conductance is dependent on local composition of substances and temperature. Values are estimated from the online interfacial thermal conductance database (ITC)<sup>[159]</sup>.

Each process corresponds to a phenomenological equation. However in general only two partial differential equations are solved in addition to the differential equations involving chemical reactions. The first one involves mass diffusion and balance

$$\frac{\partial n_\alpha}{\partial t} = \nabla \cdot (D_\alpha \nabla n_\alpha) + \sum_i \dot{n}_{\alpha, R_i} \quad (7-13)$$

where  $\alpha = Al, Cu, Cu_2O, \dots$  refers to different substances and  $\dot{n}_{\alpha, R_i}$  refers to the change in the number of atoms of substance  $\alpha$  due to reaction  $R_i$ . Similar to the mass transport equation, the energy equations is

$$\sum_\alpha n_\alpha C_{p,\alpha} \frac{\partial T}{\partial t} = \nabla \cdot (\kappa_T \nabla T) + \dot{Q}_{R_i} \quad (7-14)$$

where  $C_{p,\alpha}$  is the standard specific heat (per unit mole) of material  $\alpha$  and  $\dot{Q}_{R_i}$  is the heat released/consumed during chemical reaction  $R_i$ .

Chemical reactions can be described by ordinary differential equations whose forms are dependent on the order of the chemical reactions. Take the first reaction in Eq. (7-11) as an example; its governing equation is

$$\begin{aligned}\dot{n}_{Al,R(7-11)} &= k_{R(7-11)}[O] \\ \dot{Q}_{Al,R(7-11)} &= \dot{n}_{Al,R(7-11)} \times \Delta G_{R(7-11)}\end{aligned}\quad (7-15)$$

where  $[O]$  is the atom fraction of oxygen ion and  $\Delta G_{R_i}$  is the standard free energy change.

Equations (7-13)- (7-15) define a complete set of partial differential equations that can be investigated by numerical simulations.

### 7.2.3: Parameterization of model-based DSC curves

This simulation study is almost the same as the previous one except that the joule heating is removed from the system as shown in (7-1)c. Instead, we set the temperature increase at a constant speed, known as the heating rate  $\beta$  [K/s] in DSC experiments. The DSC curve was calculated by simulation based on following algorithms.

14. Set the temperature of the system to  $T$  and be homogenous.
15. For a short period of time  $\delta t$ , simulate all chemical reaction processes described by Eq. (7-11) and Eq. (7-12). Record overall enthalpy change  $\delta H$  and heat output rate  $\delta H/\delta t$ .
16. Recalculate the specific heat capacity after chemical reaction simulations and record heat input rate  $\sum_{\alpha} n_{\alpha} C_{p,\alpha} \delta T/\delta t$ .
17. Update the temperature of the system to  $T + \delta T$  and repeat step 1-3 until a preset terminal temperature is reached.

### 7.3 Results and discussion

Plotted in the Figure 7.2 are calculated temperature profiles from simulations of the first configuration discussed above. The two levels in panel (a) correspond to aluminum and copper oxide layers. At 0.001s after the voltage is applied the platinum leads heat quicker than both laminate layers, while the aluminum layer heats quicker than the copper oxide due to the higher resistivity of the latter. At time 0.025 s (panel (b)) both laminate structures have the same temperature due to heat transfer that approaches the metal leads. Plotted in panel (c) are the temperature profiles at 0.027 s, which is after initiation of the thermite reaction. At this applied voltage initiation of the thermite reaction occurs near the region where the thermite and lead meet. This results in extreme transient temperatures as apparent in panel (c).

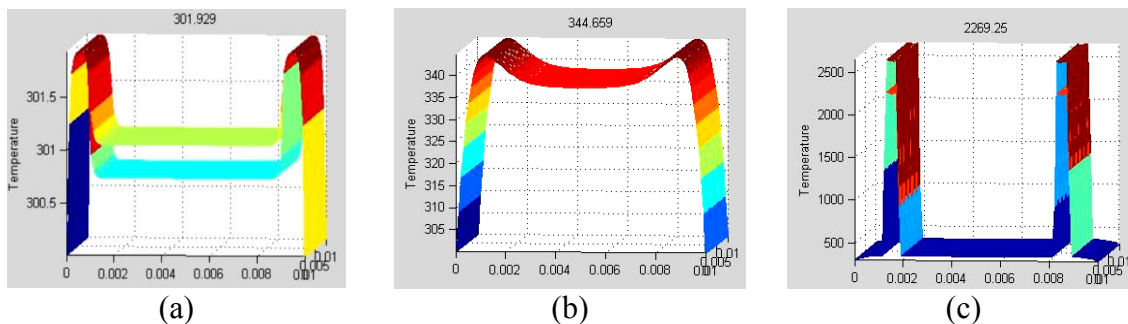


Figure 7.2: Temperature profiles that demonstrates the different stages during joule heating and thermite reaction. (a)  $t=0.001$ s. (b)  $t=0.025$ s. (c)  $t=0.027$ s. The small time and large temperature difference between panels (b) and (c) compared to those between panels (a) and (b) is consistent with the delay time and rapid reaction observed experimentally

The highest temperature at the combustion front (also known as the adiabatic temperature) in the numerical experiment is about 2269K. This is in good agreement with previous reported adiabatic temperature (~2846 K) for the CuO/Al reaction by Zhang and Richmond<sup>[160]</sup>. The propagation speed for the combustion front is about 1m/s, as shown in the Figure 7.4. This is also consistent with previous experimental research that reported a propagation velocity of 1 m/s for 1 $\mu$ m bilayer thickness CuO<sub>x</sub>/Al thermites<sup>[161]</sup>.

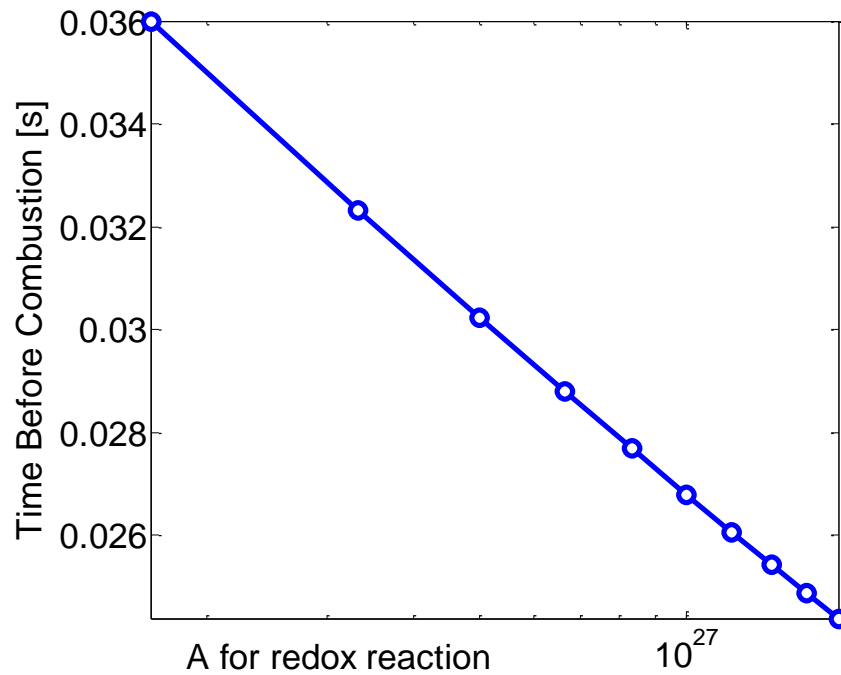


Figure 7.3: Logarithm of time before initiation vs. pre-exponential component with  $E_a=150\text{kJ/mol}$  and applied potential  $V_1=0.1\text{ V}$ .

Plotted in the Figure 7.3 is the time before the rapid rise (thermite initiation) in the simulation as a function of the pre-factor in the reaction Arrhenius rate for constant activation energy of 150kJ/mole and an applied voltage of 0.1 eV. Smaller prefactors require longer times and hence more Joule heating before the self-sustaining reaction is initiated. From an analysis of this numerical data it appears the dependence of the time to initiation on the prefactor is a power law. As far as we know, this behavior has not been reported before for at least two reasons. First of all normally one set of constant pre-factor and activation energy is assumed for one type of thermite. Secondly, in most of the published research only the pre-exponent and activation energy for diffusion is constant because the reactions in thermite combustion are considered controlled.

In traditional thermite modeling kinetic parameters such as activation energy and pre-exponent factor of the rate determining step is determined by comparing calculated reaction propagation speed to experiment values<sup>[162], [163]</sup>. In our simulation, we found that the reaction propagation speed is relatively independent of the pre exponent factor, but strongly correlated to activation energy as shown in the Figure 7.4 and Figure 7.5. This result is similar to the relationship of combustion wave speed and activation energy in metal powder combustion experiments<sup>[162], [163]</sup>.

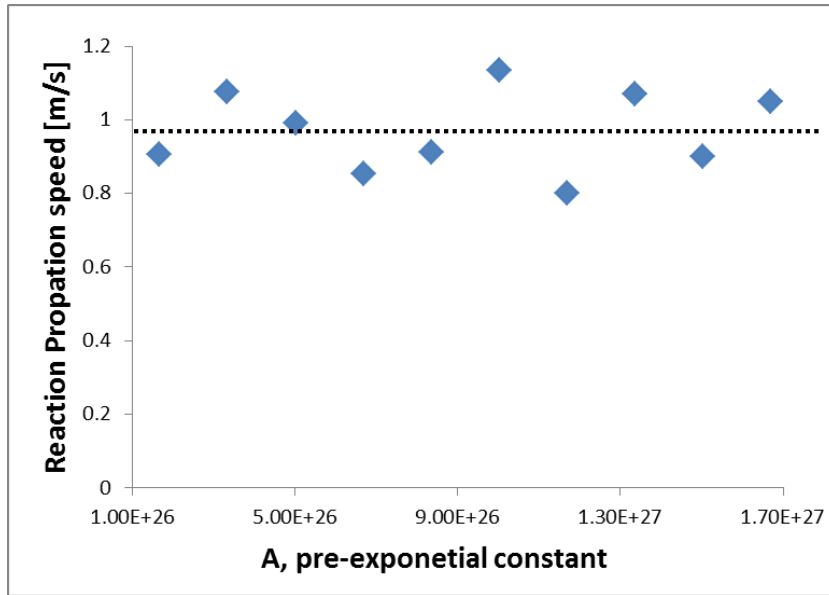


Figure 7.4: Dependence of reaction propagation speed on pre-exponential constant of Eq. (7-6).

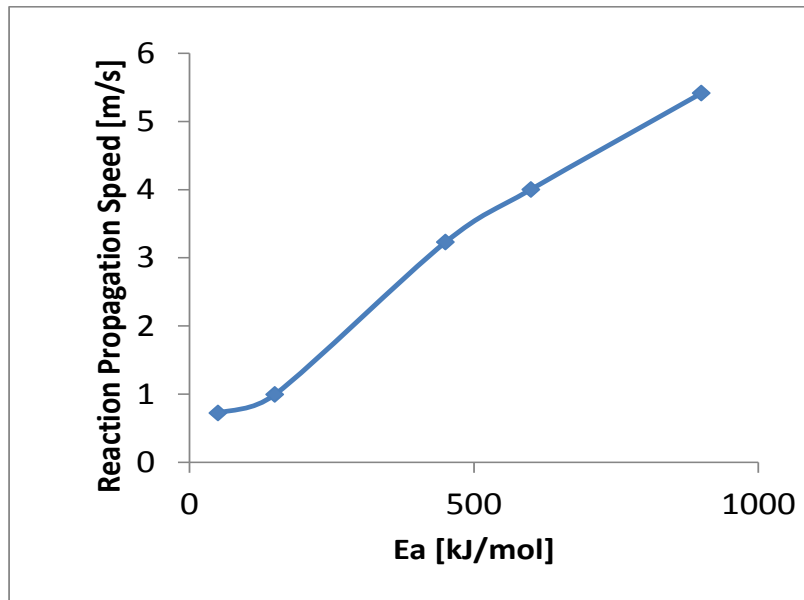


Figure 7.5: Dependence of reaction propagation speed on activation energy of Eq. (7-6).

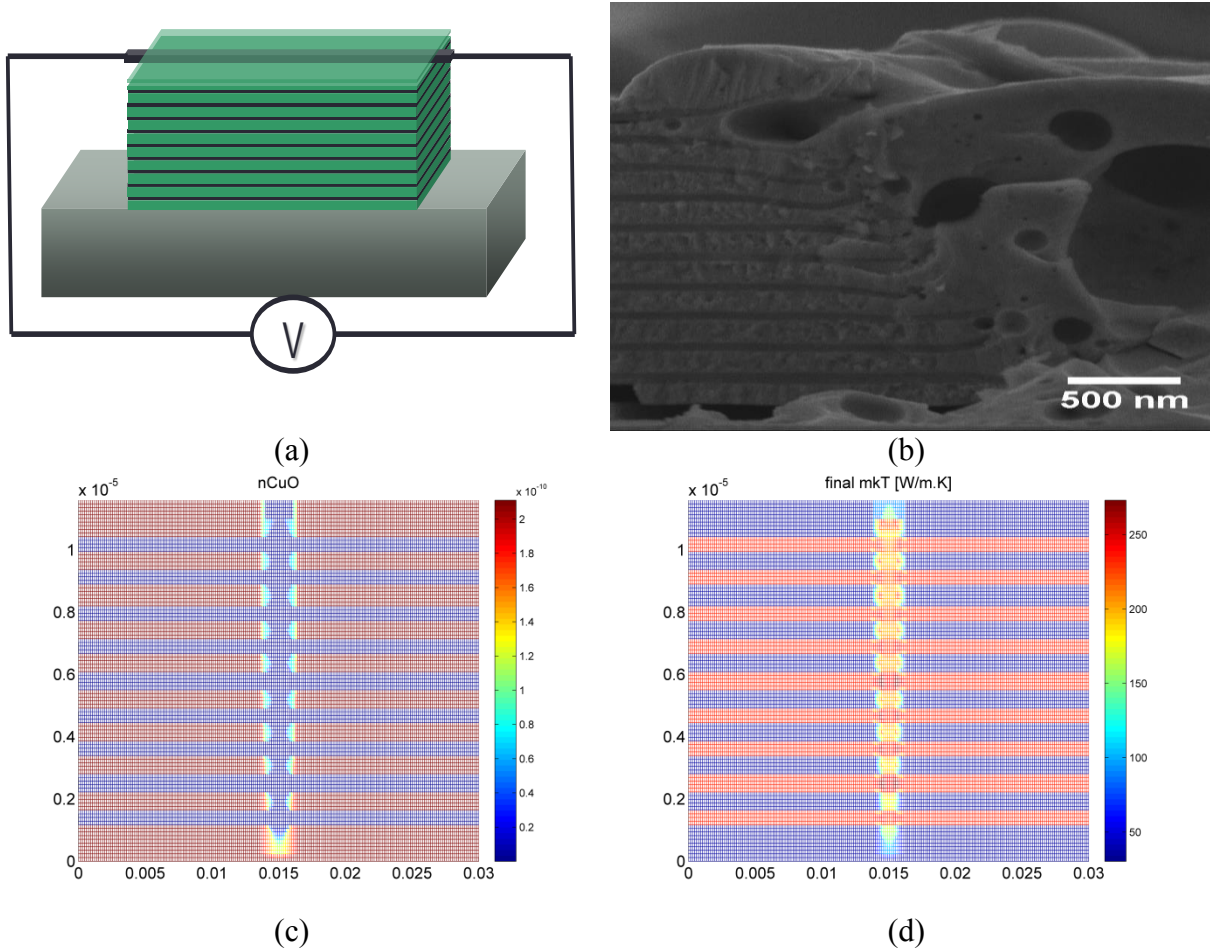


Figure 7.6: The wire heating experiment. (a) The experimental setup, in which a Pt wire is embedded in the top CuO layer, and Joule Heating is applied by applying constant electric potential on the two sides of the Pt wire. (b) The SEM image of the cross section of the final product. (c) The composition mesh of CuO in the final state in the simulation II. (d) The temperature profile before ignition..

In the wire heating case, the heating source comes from the Pt wire on top of the sample as illustrated in Figure 7.1b and Figure 7.6a. In experiments, we found that the combustion can be ignited quickly by Joule Heating in the Pt wire. However, the combustion was localized to a very narrow region and did not propagate to other regions. We believe that

this is due to the competition between the joule heating from the Pt wire and the heat dissipation to the substrate. First of all, the joule heating in the Pt can heat the Pt wire up to 800K quickly within 0.05seconds at which the combustion can be ignited. On the other hand, the heat will diffuse quickly into the substrate due to the contact conductance between the sample and the substrate. Overall, the heat source from the Pt wire and the heat contact conductance on the bottom creates a temperature gradient across the sample as shown in the Figure 7.6d. The temperature profile leads to a strip pattern of the reaction region as shown in the Figure 7.6b.

To make sure our simulations is consistent with conventional thermal analysis (DSC/DTA) results, DSC curves are also calculated based on the numerical simulation. Compared to the DSC curve generated in the Chapter 6, numerical simulation in this case incorporates more information:

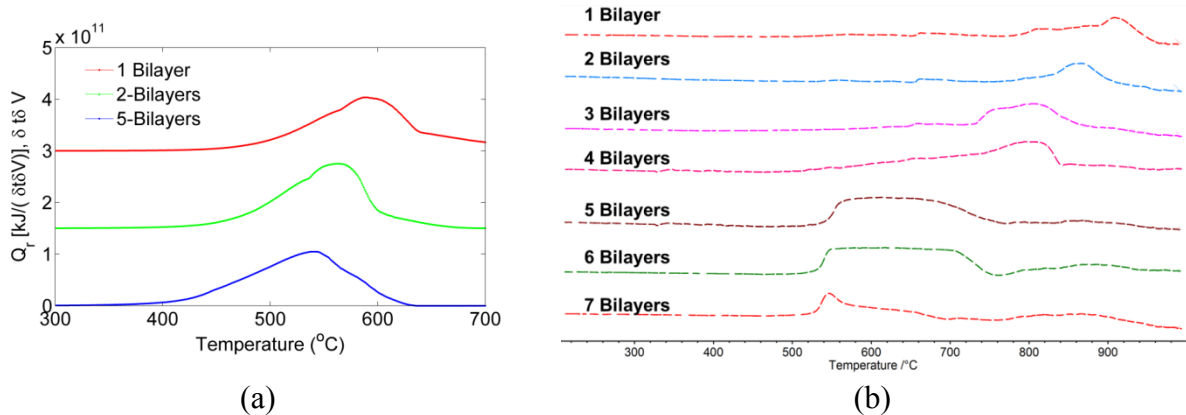


Figure 7.7: Comparison of DSC curve obtained from simulation (a) and from experiments (b). Note that the units of x axis are Kelvin for (a) and Celsius for (b) respectively.

1. In Chapter 6, only mass diffusion is considered since it assumes that diffusion controls the reaction. In this chapter, all five reactions as listed in Eq. (7-11) and Eq. (7-12) are taken into consideration.
2. In Chapter 6, mass diffusivities are dependent on the temperature only. But in this chapter, they are also dependent on the composition of various materials and phases.
3. In Chapter 6, reaction rates are considered. In this chapter they are included in the Eq. (7-15) and are considered as functions of material contents, temperature and phases.

The resulting DSC curves show similar behavior as they were in Chapter 6. This result confirms that the assumptions that reactions are diffusion controlled are valid. In addition this results proves that reaction constants such as pre-exponents or activation energies can play an important role in the thermite combustion as shown in the above text and also do not overshadow the control of mass diffusion.

## **Chapter 8 Proposal for using nano-reactive materials for hyperthermia cancer treatment**

Nano materials have been widely used for cancer therapy; examples include targeted drug delivery, enhanced magnetic imaging, and hyperthermia treatment. The fundamental basis for all the applications is that the nano particles accumulate in the tumor cells.

### **8.1 Nano-material and cancer targeting**

In the battle against cancer, effectiveness of a treatment is usually directly related to the treatment's ability to target and attack the tumor cells. Conventional cancer treatments such as chemotherapies and radioactive therapies are non-specific. This results in deleterious side effects as anti-cancer and radiation attacks healthy cells in addition to pathogen tumor cells. Furthermore, tumor cells usually resist drugs at the tumor level. The poor vascular structure in the tumor region can build a drug resistance shell preventing intravenously distributed therapeutic agents being delivered to the tumor region. In contrast, if carefully designed nano particles can utilize the vascular structure of tumor cells and accumulate automatically in the tumor cell by virtue of the well-known Enhanced Permeability and Retention (EPR) effect.

Generally speaking, nano particles have a relatively uniform size distribution and have an average size of several tens of nanometers. This allows them to pass easily through tumor cells with leaky, hyper-permeable membrane whose pore sizes range from 100nm to 1200nm<sup>[164], [165]</sup>. In addition, tumors have higher than normal interstitial pressure due to their

lack of organized lymphatic system. The resulting outward interstitial drainage fluid flow drives normal tissues away from tumor but has little impact on the nano particles, which can enter the interstitium and be entrapped in the tumor<sup>[166]</sup>. Nano particles are usually coated with hydrophilic polymers. Conventional nano particles without hydrophilic coatings would be accumulated in the mononuclear phagocytes system (MPS) organs such as liver, spleen, lung or bone marrow if administered intravenously. This metabolism route has been demonstrated in vivo in various animals. Detailed research carried by<sup>[167]</sup> showed that doxorubicin coated nano-spheres were opsonized and cleared by the MPS quickly after intravenous administration resulting lower concentration of anti-cancer agent in the tumor region than the case when free doxorubicin was administrated.

Aside from nano particles' having higher retention times than normal tissues, targeted drug delivery for nano particles can be further enhanced by other approaches, such as surface-modification with agents targeting to tumor specific molecules and angiogenesis process. Tumor cell targeting, also known as the tumor-activated prodrug targeting or antibody targeting, coats the nano particles with linkers (usually ligands) that bind to specific accepters on the surface of tumor cells but not the surface of healthy cells. For example, it has been found that the folate receptor is significantly over expressed in many cancers, such as lung, ovarian, brain, neck, head, renal and breast cancers<sup>[168], [169]</sup>. Methotrexate (MTX, an analogue of folic acid and a frequently used targeting agent for folate accepter) coated ion-oxide nano particles showed high uptake level in human cervical cancer cells uptake studies<sup>[170]</sup>. A great example of utilizing folate acceptor comes from the work done by Sonvico et al<sup>[171]</sup>, in which the uptake of folate-conjugated ion nanoparticles by the different

cells were investigated in vitro. The results showed that the uptake number of nanoparticles can be as high as 46, 307 and 65 per cell by human epithelial mouth carcinoma cells, human breast adenocarcinoma cells and human cervix adenocarcinoma cells, respectively.

A tumor cell can grow steadily by passive nutrient diffusion until its size reaches about  $2 \text{ mm}^3$  beyond which phase the angiogenesis process is required to support further expanding of the tumor mass. Angiogenesis targeting as the drug delivery scheme has become the subject of intensive research and has generated numerous innovations for decades<sup>[172], [173]</sup>. The Angiogenesis is especially important in nano particle cancer therapies for at least two reason: (i) the EPR effect shows up only when the angiogenesis process is developing due to the abnormal growth of tumor vessels and tortuosity of the neovascular<sup>[172], [173]</sup>. (ii) Angiogenesis process has been proven critical for the growth, invasion, migration and proliferation of solid tumors. Regulating the neovasculature has been proven effective in preventing tumors translating to the metastatic form which are capable of spreading to other parts of the body<sup>[165], [174], [175]</sup>.

## **8.2 Nano material and magnetic hyperthermia treatment**

Magnetic hyperthermia cancer treatment is a therapeutic procedure in which magnetic particles targeted cancer cells are exposed to high frequency alternating magnetic field (AMF), and accordingly the temperature of tumor loaded tissue is raised to hyperthermia temperature ( $42 \text{ }^\circ\text{C} - 45 \text{ }^\circ\text{C}$ ) due to various relaxation processes and magnetic losses. The rationale is based on the fact that tumor cells being subject to a careful controlled high temperature are more fatal than normal cells because of their abnormal activity, compact

vascular structure and having difficulty dissipating the heat. Early use of hyperthermia usually requires an external magnetic field: Magnetic particles that were injected intravenously or through intra-arterial were directed to the specific sites of the body by external high strength magnets such as rare earth magnets or electromagnets. After magnetic particles are concentrated at the tumor sites, those cells can be killed by AMF heating or anti-cancer drug carried by magnetic particles and released by changing other physiological conditions such as pH or local temperature. Among all the magnetic hyperthermia methods, magnetic nano particle (MNPs) hyperthermia is gaining increased scientific and technological interest due to many attractive possibilities it may offer. First, as nano particles it offers promising capability of targeting tumor cells as mentioned previously. Second the nano particles are magnetic and hence will response to an external magnetic field. This makes them useful to enhance the detection and diagnosing of the tumor with the magnetic resonance imaging (MRI) and to deliver pharmacological active drug to tumor sites under the external magnetic field guidance and release them by AMF heating.

MNP hyperthermia is only one branch of the overall hyperthermia family as shown in the Figure 8.1. A close relative of MNP hyperthermia therapy implants macroscopic magnetic grains directly into the tumor sites. These magnetic grains will then serve as thermal seeds under AMF. Comparing to MNPs, the magnetic seed procedure is less selective and cannot target tumors at the cell level. However it is cheaper and is easier to control. Hence it has been used in clinical practice already while MNP hyperthermia is still in phase II trials. In addition to using magnetic particles (either microscopic or macroscopic scale), localized hyperthermia can also be achieved by magnetic induction in which body

tissue is exposed to high frequency AMF directly and conduction current flow is induced therefrom. Researchers have found that the temperature in many tumors, even if they are at the center of the patients, can be elevated to 42 °C and above by magnetic induction procedure. Aside from localized hyperthermia, the whole body hyperthermia therapy is often mentioned has found use as a complimentary procedure to conventional cancer treatments for a long time. In fact it can be traced back to 5,000 BC when Parminides, a Greek Physician said “Give me a chance to create a fever, and I will cure any disease”.

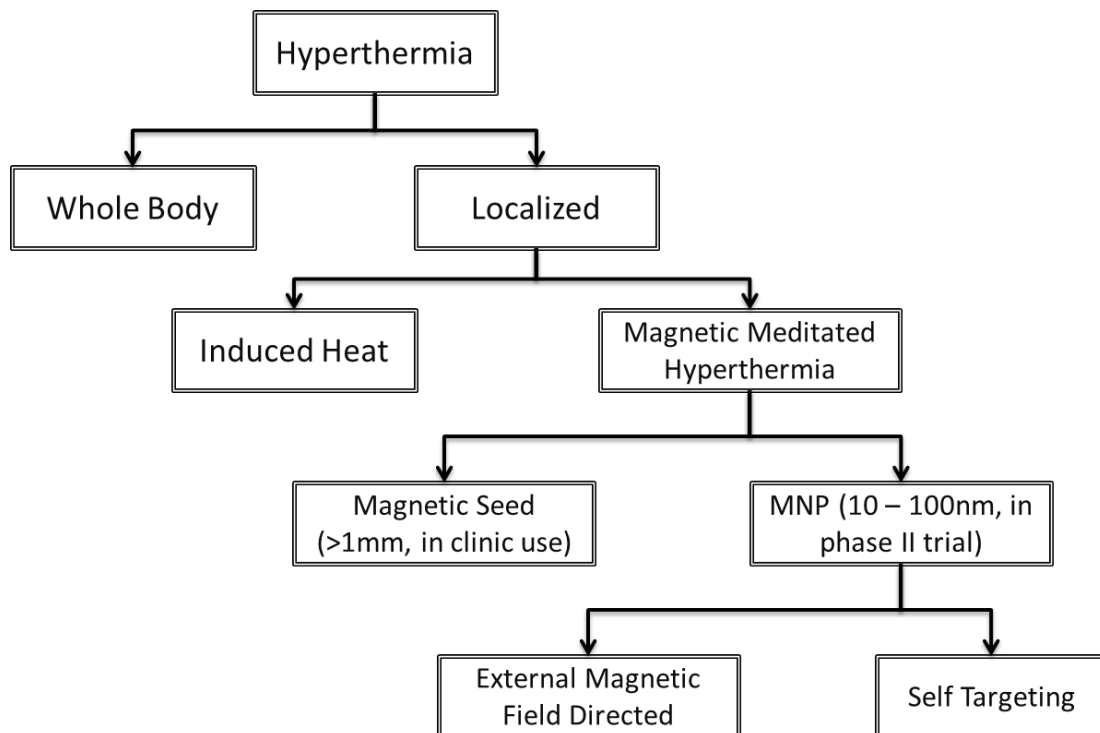


Figure 8.1: Sketch of the family tree for hyperthermia treatments in oncology

### 8.3 Magnetic hyperthermia treatment & specific loss power

The efficiency of heat generation in magnetic hyperthermia treatment is measured by the specific loss power (SLP) or specific absorption rate (SAR). The two terms are often used indiscriminately because they both are the measure of heat dissipation/generation rate in the target tissue; they both have the same unit: W/g and they both depend on the average size, magnetic permeability, and the average density of nanoparticles, AMF magnitude and so on.

In theory, high as possible SLP values are desirable. Higher heat generation efficiency means fewer amounts of magnetic particles are required to elevate the tumor tissue temperature and hence brings less degree of side effects to the patients. In the past decades tremendous efforts have been dedicated to the quest to synthesize magnetic nanoparticles with optimum SLP characteristics. SLP values reported by the overwhelming majority of these researches are in the range of 10 – 500 W/g<sup>[176]–[178]</sup> while some extraordinary results have also been reported. For example Hergt *et al.* reported that SLP of bacterial magnetosomes can be as high as about 1000 W/g under 410kHz and 10kA/m AMF. By taking advantage of the exchange coupling between an inner magnetic core and outer magnetic shell, Lee *et al.* was able to tune the SLP value of core–shell magnetic nanoparticles to as high as 4000 W/g under a frequency of 500kHz and an amplitude of 37.3kA/m AMF.

#### 8.4 Hyperthermia treatment using nano energetic materials

Based on the DSC thermograph, the DSC peak value can be as high as 500 W/g even though it is reduced because the DSC of the second ramp was subtracted from the first one for baseline refinement. This value is comparatively high with that of specific loss power (SLP) in the magnetic nano particle (MNP) hyperthermia cancer treatment in which MNP targeted cancer cells are exposed to high frequency alternating magnetic field (AMF). Due to various relaxation processes and magnetic losses, the magnetic particles loaded tumor cells can be heated to hyperthermia temperature (42 °C – 45 °C) at which tumor cells are more fatal than normal cells because of their abnormal activity, compact vascular structure and having difficulty dissipating the heat. In cancer treatment, the biggest problems come from the spreading and fast proliferation of metastasis tumor cells, which are hard to detect or remove by surgery. Nano particles, thanks to the well-known Enhanced Permeability and Retention (EPR) effect<sup>[175], [179]–[181]</sup>, can pass through and be entrapped in the tumor cells that have leaky, hyper-permeable membrane with pore sizes ranging from 100nm to 1200nm. Because of this, MNP hyperthermia cancer treatment was placed a lot of hope on their ability to target and attack cancer cells precisely.

In terms of practicality, the application of MNP hyperthermia cancer treatment is limited by SLP, which measures the heat generation efficiency of MNPs and also has a unit of W/g:

$$SLP = \frac{1}{m_{MNP}} \frac{dQ}{dt} \quad (8-1)$$

In the expression,  $m_{MNP}$  and  $dQ/dt$  are the total mass and the overall heat generation speed of MNPs respectively. According to the estimation of Hergt *et al.* [176], it would require SLP values to be unrealistically high (more than 1 million W/g) to elevate the temperature of a single metastasis cancer cell in the human body by 5 °C. The word “unrealistic” was used by Hergt *et al.*, because it exceeds the physical limit (~50,000 W/g) of AMF heating. On the other hand, if solid reactions, such as thermite reactions are involved, those SLP values may be achievable.

First we imitate the definition of SLP and define the solid reaction contribution to it by following equation:

$$SLP_s(t_p) \equiv \frac{1}{t_p} \int_0^{t_p} DSC(t) dt \quad (8-2)$$

where  $t_p$  is the time when certain percentage ( $p$ ) of reaction is proceeded. Considering that DSC is linearly dependent on the enthalpy of the reaction ( $\Delta H$ ), SHR therefore also a linear function of  $\Delta H$ . Moreover, under the isothermal condition, the diffusivities are regarded as constants, and thus SHR is approximately linear dependent on the diffusivity when  $p$  is small, i.e.  $SLP_s(t_p) \propto D_0 e^{-E_a/RT}$  or  $\ln[SLP_s(t_p)/D_0] \propto -E_a$  as shown in the Figure 8.1.

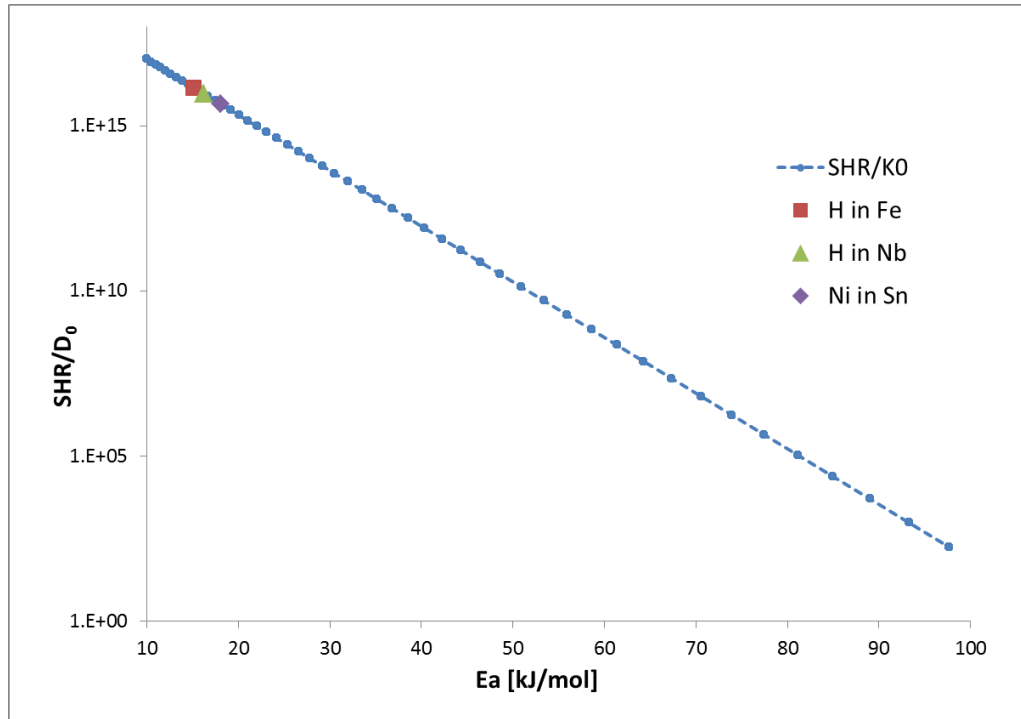


Figure 8.2: Demonstration of the relationship between  $SHR(t_p)$ , activation energy and diffusion pre-exponent in nano energetic materials. The plot was made from numerical solution of 1-D diffusion equation with  $p=0.2$  at the temperature  $36.8\text{ }^\circ\text{C}$  and enthalpy of the reaction is  $1\text{ kJ/g}$ .

As shown in the Figure 8.2, the theoretical SHR value for nano energetic nanoparticles can reach up to  $1 \times 10^{12}\text{ W/g}$  if the diffusivity has an activation energy of  $10\text{ kJ/mol}$  and pre-exponent of  $1 \times 10^{-5}\text{ m}^2/\text{s}$ . Similar diffusion parameters can be found from diffusion database. For instance, parameters for hydrogen diffusion in  $\text{Fe}^{[182]}$ ,  $\text{Nb}^{[183]}$  and Ni diffusion in  $\text{Sn}^{[184]}$  are  $(1.1 \times 10^{-6}\text{ m}^2/\text{s}, 15.1\text{ kJ/mol})$ ,  $(1.0 \times 10^{-6}\text{ m}^2/\text{s}, 16.2\text{ kJ/mol})$  and  $(1.99 \times 10^{-6}\text{ m}^2/\text{s}, 18.1\text{ kJ/mol})$  respectively. Substituting these values into the DSC expression, performing numerical calculation to calculate DSC(t) curve with the same parameters as Figure 8.2, and integrating DSC(t) overtime as mentioned in Eq. (8-2) leads to

SHR values of  $1.57 \times 10^{10}$ ,  $9.33 \times 10^9$  and  $8.88 \times 10^9$  W/g respectively. This is only a conceptual calculation: in a real case, the reactants must be separated carefully, because the solid reactions for above mentioned three couples of materials would proceed so fast, they will react immediately once reactants are in contact at human body temperature.

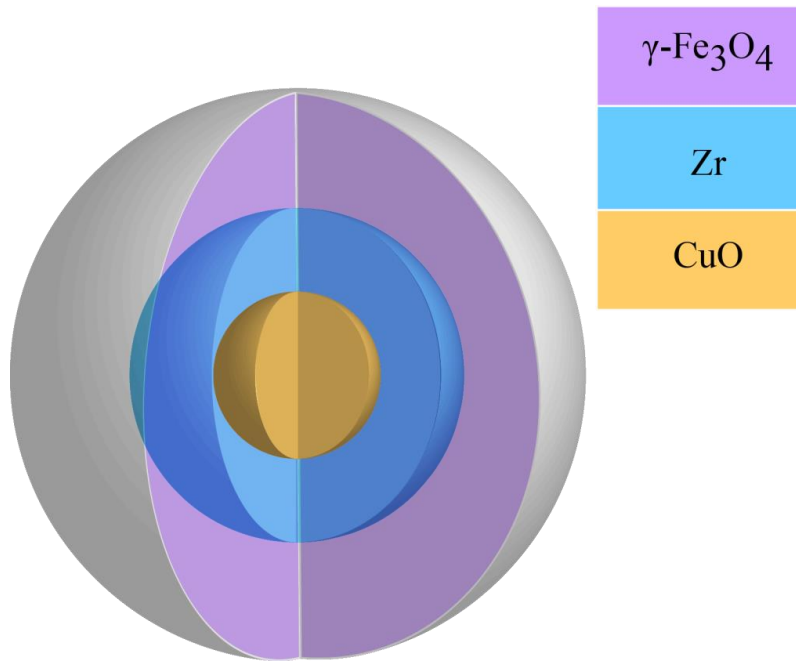


Figure 8.3: A design of nano-composite of maghemite coated nano thermite for hyperthermia treatment

Another design for potential application of nano-energetic materials in cancer hyperthermia treatment is utilizing AMF heating as initiation and exothermal heat from solid reaction as the major hyperthermia heating source. A possible geometry is illustrated in the Figure 8.3, where a nano-thermite of Zr – CuO is coated with magnetite. This concentric

three layers' nano-composite can be viewed as the direct extension to widely studied core-shell nanoparticles, which surprisingly often have higher SLP values than conventional single substance magnetic particles<sup>[185]–[189]</sup>.

Assuming that this nano particle has an optimum SLP value of 1000 W/g; the overall diameter is 60nm with each layer has equal length of 10nm, therefore the overall mass is  $6.49 \times 10^{-16}$  gram and the total heat capacity is about  $4.08 \times 10^{-16}$  J/K. In the extreme case if heat does not dissipation to the environment in the first 1 second, the initial temperature rise rate will be about  $SLP \times m_{\gamma-Fe_3O_4} / C_p \approx 1057$  K/s. In this case, the encapsulated nano-thermite can be ignited within one second. Because the thermite combustion speed is so fast (reaction finished within microseconds even with thermite powders<sup>[190]</sup>), we can safely assume it is complete within a micro-second. Then the thermite reaction can boost the original SLP by  $\delta SLP = \Delta t^{-1} \Delta H m_r m_{total}^{-1}$ , where  $\Delta H = 3126$  (J/g) is the reaction enthalpy for Zr – CuO redox reaction<sup>[157]</sup>,  $m_r$  (g) is the reactant mass and  $m_{total}$  is the overall mass of the nano particle,  $\Delta t = 1 \mu s$  is the estimated combustion time for the thermite reaction. Substituting necessary values into the expression of  $\delta SLP$ , the thermite reaction contribution to the original SLP for the design in Figure 8.3 is estimated to be greater than  $3 \times 10^6$  W/g.

It must be noted that, in practical situations, the thermite reaction may never be initiated due to possibly extraordinary high thermal conductance of nano particle/fluid interface according to several published studies<sup>[191]–[193]</sup>. For example, Ge *et al.* measured the heat conductance across interfaces between water and functionalized Au nanoparticles<sup>[192]</sup>. The resulting heat conductance is in the range of 150 to 250 MW m<sup>-2</sup> K<sup>-1</sup>. With heat conductance this high, the temperature difference between the interior and exterior of the

nano particle can be ignored<sup>[194]</sup> and the maximum temperature between the nano particle and the environment will be less than 10 °C<sup>[194], [195]</sup>. However, we shouldn't give up our hope so quickly: first of all, all the heat conductance measurements were measured with low energy density (~0.2 mJ.cm<sup>-2</sup>), but equivalent energy density in MNP hyperthermia is at least several orders higher (about 20J.cm<sup>-2</sup>). Heat conductance may be limited in the latter case. Secondly, many of the investigated nano-particles were designed to have as high thermal conductivity as possible so that they can be used to enhance the heat conduction efficiency in fluids<sup>[196]</sup>,<sup>[197]</sup>. It may be possible to design nano-particles so that they have small thermal conductivity. Thirdly, except for thermal ignition, reaction in the reactive nano particles may also be initiated by other means such as pressure and induced current<sup>[198], [199]</sup>. Last and the most importantly, because application of magnetic nano particles hyperthermia cancer has reached a deadlock, inclusion of reactive nano particles can be a promising breakthrough.

## REFERENCES

- [1] D. A. Reed, R. Bajcsy, M. A. Fernandez, J.-M. Griffiths, R. D. Mott, J. Dongarra, C. R. Johnson, A. S. Inouye, W. Miner, M. K. Matzke, and others, “Computational Science: Ensuring America’s Competitiveness,” 2005.
- [2] M. Kleman and J. Friedel, “Disclinations, dislocations, and continuous defects: A reappraisal,” *Rev. Mod. Phys.*, vol. 80, no. 1, pp. 61–115, Jan. 2008.
- [3] P. C. Millett, R. P. Selvam, and A. Saxena, “Molecular dynamics simulations of grain size stabilization in nanocrystalline materials by addition of dopants,” *Acta Mater.*, vol. 54, no. 2, pp. 297–303, Jan. 2006.
- [4] P. Lejček, “Models of Equilibrium Grain Boundary Segregation,” in *Grain Boundary Segregation in Metals*, vol. 136, Springer Berlin Heidelberg, 2010, pp. 51–102.
- [5] K. a. Darling, B. K. VanLeeuwen, C. C. Koch, and R. O. Scattergood, “Thermal stability of nanocrystalline Fe–Zr alloys,” *Mater. Sci. Eng. A*, vol. 527, no. 15, pp. 3572–3580, Jun. 2010.
- [6] K. A. Darling, B. K. VanLeeuwen, J. E. Semones, C. C. Koch, R. O. Scattergood, L. J. Kecskes, and S. N. Mathaudhu, “Stabilized nanocrystalline iron-based alloys: Guiding efforts in alloy selection,” *Mater. Sci. Eng. A*, vol. 528, no. 13–14, pp. 4365–4371, 2011.
- [7] B. K. VanLeeuwen, K. A. Darling, C. C. Koch, R. O. Scattergood, and B. G. Butler, “Thermal stability of nanocrystalline Pd<sub>81</sub>Zr<sub>19</sub>,” *Acta Mater.*, vol. 58, no. 12, pp. 4292–4297, 2010.
- [8] M. P. Allen, D. J. Tildesley, and J. R. Banavar, “Computer simulation of liquids,” *Phys. Today*, vol. 42, p. 105, 1989.
- [9] D. W. Brenner and B. J. Garrison, “Gas-Surface Reactions: Molecular Dynamics Simulations of Real Systems,” 1989.
- [10] D. W. Brenner, “The Art and Science of an Analytic Potential,” *Phys. status solidi*, vol. 217, no. 1, pp. 23–40, Jan. 2000.
- [11] M. Daw, “The embedded-atom method: a review of theory and applications,” *Mater. Sci. Reports*, vol. 9, no. 7–8, pp. 251–310, Mar. 1993.

- [12] S. Lu, D. Li, and D. W. Brenner, *Handbook of Damage Mechanics*. New York, NY: Springer New York, 2015.
- [13] M. I. Baskes and R. A. Johnson, “Modified embedded atom potentials for HCP metals,” *Model. Simul. Mater. Sci. Eng.*, vol. 2, no. 1, pp. 147–163, Jan. 1994.
- [14] M. Baskes, “Modified embedded-atom potentials for cubic materials and impurities,” *Phys. Rev. B*, vol. 46, no. 5, pp. 2727–2742, Aug. 1992.
- [15] Y. Q. Cheng and E. Ma, “Atomic-level structure and structure–property relationship in metallic glasses,” *Prog. Mater. Sci.*, vol. 56, no. 4, pp. 379–473, May 2011.
- [16] M. a. Tschopp and D. L. McDowell, “Asymmetric tilt grain boundary structure and energy in copper and aluminium,” *Philos. Mag.*, vol. 87, no. 25, pp. 3871–3892, Sep. 2007.
- [17] W. Read and W. Shockley, “Dislocation models of crystal grain boundaries,” *Phys. Rev.*, vol. 78, no. 3, p. 275, 1950.
- [18] F. Nabarro, “Mathematical theory of stationary dislocations,” *Adv. Phys.*, vol. 1, no. January 2012, pp. 269–394, 1952.
- [19] J. Li, “Some elastic properties of an edge dislocation wall,” *Acta Metall.*, vol. 8, no. 8, pp. 563–574, 1960.
- [20] J. C. M. Li, “High-Angle Tilt Boundary—A Dislocation Core Model,” *J. Appl. Phys.*, vol. 32, no. 3, p. 525, 1961.
- [21] D. Brandon, “The structure of high-angle grain boundaries,” *Acta Metall.*, vol. 14, no. 11, pp. 1479–1484, 1966.
- [22] J. D. Eshelby, “A simple derivation of the elastic field of an edge dislocation,” *Br. J. Appl. Phys.*, vol. 17, no. 9, pp. 1131–1135, Sep. 1966.
- [23] J. C. M. Li, “Disclination model of high angle grain boundaries,” *Surf. Sci.*, vol. 31, pp. 12–26, Jun. 1972.
- [24] K. K. Shih and J. C. M. Li, “Energy of grain boundaries between cusp misorientations,” *Surf. Sci.*, vol. 50, no. 1, pp. 109–124, May 1975.
- [25] a. P. Sutton and V. Vitek, “On the Structure of Tilt Grain Boundaries in Cubic Metals I. Symmetrical Tilt Boundaries,” *Philos. Trans. R. Soc. A Math. Phys. Eng. Sci.*, vol. 309, no. 1506, pp. 1–36, Mar. 1983.

- [26] W. Gui-Jin and V. Vitek, "Relationships between grain boundary structure and energy," *Acta Metall.*, vol. 34, no. 5, pp. 951–960, May 1986.
- [27] A. E. Romanov and A. L. Kolesnikova, "Application of disclination concept to solid structures," *Prog. Mater. Sci.*, vol. 54, no. 6, pp. 740–769, Aug. 2009.
- [28] Y. Purohit, L. Sun, O. Shenderova, R. O. Scattergood, and D. W. Brenner, "First-principles-based mesoscale modeling of the solute-induced stabilization of  $\langle 100 \rangle$  tilt grain boundaries in an Al–Pb alloy," *Acta Mater.*, vol. 59, no. 18, pp. 7022–7028, Aug. 2011.
- [29] a. a. Nazarov, O. a. Shenderova, and D. W. Brenner, "On the disclination-structural unit model of grain boundaries," *Mater. Sci. Eng. A*, vol. 281, no. 1–2, pp. 148–155, Apr. 2000.
- [30] O. Shenderova, D. Brenner, A. Nazarov, A. Romanov, and L. Yang, "Multiscale modeling approach for calculating grain-boundary energies from first principles," *Physical Review B*, vol. 57, no. 6, pp. R3181–R3184, 1998.
- [31] S. Lu and D. W. Brenner, "Solute Segregation Energy and Grain Boundary Energy Calculation Based On Disclination Structural Unit Model and Perturbation Methods."
- [32] D. Molodov, V. Ivanov, and G. Gottstein, "Low angle tilt boundary migration coupled to shear deformation," *Acta Mater.*, vol. 55, no. 5, pp. 1843–1848, Mar. 2007.
- [33] T. Gorkaya, D. a. Molodov, and G. Gottstein, "Stress-driven migration of symmetrical  $\langle 100 \rangle$  tilt grain boundaries in Al bicrystals," *Acta Mater.*, vol. 57, no. 18, pp. 5396–5405, Oct. 2009.
- [34] M. Furtkamp, G. Gottstein, D. Molodov, V. Semenov, and L. S. Shvindlerman, "Grain boundary migration in Fe–3.5% Si bicrystals with [001] tilt boundaries," *Acta Mater.*, vol. 46, no. 12, pp. 4103–4110, Jul. 1998.
- [35] D. L. Olmsted, E. A. Holm, and S. M. Foiles, "Survey of computed grain boundary properties in face-centered cubic metals—II: Grain boundary mobility," *Acta Mater.*, vol. 57, no. 13, pp. 3704–3713, Aug. 2009.
- [36] M. Winning, "Motion of  $\langle 100 \rangle$  -tilt grain boundaries," *Acta Mater.*, vol. 51, no. 20, pp. 6465–6475, Dec. 2003.
- [37] F. Uyar, S. Wilson, M. Winning, and A. D. Rollett, "Simulation of Grain Growth under the Effect of Stress," *Mater. Sci. Forum*, vol. 715–716, pp. 197–202, Apr. 2012.

- [38] M. Winning, G. Gottstein, and L. S. Shvindlerman, "Stress induced grain boundary motion," *Acta Mater.*, vol. 49, no. 2, pp. 211–219, Jan. 2001.
- [39] Y. Huang and F. J. Humphreys, "Subgrain growth and low angle boundary mobility in aluminium crystals of orientation  $\{110\} \langle 001 \rangle$  ," *Acta Mater.*, vol. 48, no. 8, pp. 2017–2030, May 2000.
- [40] R. B. N. Godiksen, S. Schmidt, and D. Juul Jensen, "Molecular dynamics simulations of grain boundary migration during recrystallization employing tilt and twist dislocation boundaries to provide the driving pressure," *Model. Simul. Mater. Sci. Eng.*, vol. 16, no. 6, p. 065002, Sep. 2008.
- [41] L. S. S. G. Gottstein, *Grain Boundary Migration in Metals: Thermodynamics, Kinetics, Applications, Second Edition (Materials Science & Technology)*, 2nd ed. CRC Press, 2009.
- [42] K. G. F. Janssens, D. Olmsted, E. a Holm, S. M. Foiles, S. J. Plimpton, and P. M. Derlet, "Computing the mobility of grain boundaries.," *Nat. Mater.*, vol. 5, no. 2, pp. 124–7, Feb. 2006.
- [43] J. Zhou and V. Mohles, "Mobility Evaluation of  $\langle 110 \rangle$  Twist Grain Boundary Motion from Molecular Dynamics Simulation," *Steel Res. Int.*, vol. 82, no. 2, pp. 114–118, Feb. 2011.
- [44] H. Zhang, M. I. Mendeleev, and D. J. Srolovitz, "Computer simulation of the elastically driven migration of a flat grain boundary," *Acta Mater.*, vol. 52, no. 9, pp. 2569–2576, May 2004.
- [45] Z. T. Trautt, M. Upmanyu, and A. Karma, "Interface mobility from interface random walk.," *Science*, vol. 314, no. 5799, pp. 632–5, Oct. 2006.
- [46] B. Schönfelder, G. Gottstein, and L. S. Shvindlerman, "Atomistic simulations of grain boundary migration in copper," *Metall. Mater. Trans. A*, vol. 37, no. 6, pp. 1757–1771, Jun. 2006.
- [47] M. Winning and G. Gottstein, "On the mechanisms of grain boundary migration," *Acta Mater.*, vol. 50, pp. 353–363, 2002.
- [48] M. Winning and A. D. Rollett, "Transition between low and high angle grain boundaries," *Acta Mater.*, vol. 53, no. 10, pp. 2901–2907, Jun. 2005.

- [49] T. J. Rupert, D. S. Gianola, Y. Gan, and K. J. Hemker, "Experimental observations of stress-driven grain boundary migration," *Science*, vol. 326, no. 5960, pp. 1686–90, Dec. 2009.
- [50] J. W. Cahn and J. E. Taylor, "A unified approach to motion of grain boundaries, relative tangential translation along grain boundaries, and grain rotation," *Acta Mater.*, vol. 52, no. 16, pp. 4887–4898, Sep. 2004.
- [51] J. W. Cahn, Y. Mishin, and A. Suzuki, "Coupling grain boundary motion to shear deformation," *Acta Mater.*, vol. 54, no. 19, pp. 4953–4975, Nov. 2006.
- [52] M. P. Seah and E. D. Hondros, "Grain Boundary Segregation," *Proc. R. Soc. A Math. Phys. Eng. Sci.*, vol. 335, no. 1601, pp. 191–212, Oct. 1973.
- [53] M. a. Atwater, R. O. Scattergood, and C. C. Koch, "The stabilization of nanocrystalline copper by zirconium," *Mater. Sci. Eng. A*, vol. 559, pp. 250–256, Jan. 2013.
- [54] G. Gottstein and D. Molodov, "Grain boundary migration in metals: Recent developments," *Interface Sci.*, vol. 22, pp. 7–22, 1998.
- [55] S. N. Zhevnenko, "Interfacial Free Energy of Cu-Co Solid Solutions," *Metall. Mater. Trans. A*, vol. 44, no. 6, pp. 2533–2538, Feb. 2013.
- [56] S. Mahalingam, P. E. J. Flewitt, and J. F. Knott, "The ductile–brittle transition for nominally pure polycrystalline nickel," *Mater. Sci. Eng. A*, vol. 564, pp. 342–350, Mar. 2013.
- [57] W. Gui-Jin, A. P. Sutton, and V. Vitek, "A computer simulation study of  $\langle 001 \rangle$  and  $\langle 111 \rangle$  tilt boundaries: the multiplicity of structures," *Acta Metall.*, vol. 32, no. 7, pp. 1093–1104, Jul. 1984.
- [58] D. Schwartz, V. Vitek, and a. P. Sutton, "Atomic structure of (001) twist boundaries in f.c.c metals Structural unit model," *Philos. Mag. A*, vol. 51, no. 4, pp. 499–520, Apr. 1985.
- [59] O. A. Shenderova, D. W. Brenner, A. A. Nazarov, A. E. Romanov, and L. H. Yang, "CONDENSED MATTER AND MATERIALS PHYSICS."
- [60] S. Plimpton, "Fast Parallel Algorithms for Short-Range Molecular Dynamics," *J. Comput. Phys.*, vol. 117, no. 1, pp. 1–19, Mar. 1995.

- [61] D. Heyes, “Pressure tensor of partial-charge and point-dipole lattices with bulk and surface geometries,” *Phys. Rev. B*, vol. 49, no. 2, pp. 755–764, Jan. 1994.
- [62] H. Sheng, M. Kramer, a. Cadien, T. Fujita, and M. Chen, “Highly optimized embedded-atom-method potentials for fourteen fcc metals,” *Phys. Rev. B*, vol. 83, no. 13, pp. 1–20, Apr. 2011.
- [63] A. Landa, P. Wynblatt, D. J. Siegel, J. B. Adams, and O. N. Mryasov, “Development of glue-type potentials for the Al–Pb system: phase diagram calculation, A. Landa, P. Wynblatt, D.J. Siegel, J.B. Adams, O.N. Mryasov and X.-Y. Liu,” *Acta Mater.*, vol. 48, no. 13, p. 3621, Aug. 2000.
- [64] C. Deng and C. a. Schuh, “Atomistic Simulation of Slow Grain Boundary Motion,” *Phys. Rev. Lett.*, vol. 106, no. 4, p. 045503, Jan. 2011.
- [65] J. Zhou and V. Mohles, “Towards realistic molecular dynamics simulations of grain boundary mobility,” *Acta Mater.*, vol. 59, no. 15, pp. 5997–6006, Sep. 2011.
- [66] R. B. Godiksen, Z. T. Trautt, M. Upmanyu, J. Schiøtz, D. J. Jensen, and S. Schmidt, “Simulations of boundary migration during recrystallization using molecular dynamics,” *Acta Mater.*, vol. 55, no. 18, pp. 6383–6391, Oct. 2007.
- [67] H. Zhang, M. Upmanyu, and D. J. Srolovitz, “Curvature driven grain boundary migration in aluminum: molecular dynamics simulations,” *Acta Mater.*, vol. 53, no. 1, pp. 79–86, Jan. 2005.
- [68] C. Deng and C. a. Schuh, “Diffusive-to-ballistic transition in grain boundary motion studied by atomistic simulations,” *Phys. Rev. B*, vol. 84, no. 21, p. 214102, Dec. 2011.
- [69] Y. Mishin, M. Asta, and J. Li, “Atomistic modeling of interfaces and their impact on microstructure and properties,” *Acta Mater.*, vol. 58, no. 4, pp. 1117–1151, Feb. 2010.
- [70] M. I. Mendeleev, C. Deng, C. a. Schuh, and D. J. Srolovitz, “Comparison of molecular dynamics simulation methods for the study of grain boundary migration,” *Model. Simul. Mater. Sci. Eng.*, vol. 21, no. 4, p. 045017, Jun. 2013.
- [71] a. Rajabzadeh, F. Momprou, M. Legros, and N. Combe, “Elementary Mechanisms of Shear-Coupled Grain Boundary Migration,” *Phys. Rev. Lett.*, vol. 110, no. 26, p. 265507, Jun. 2013.
- [72] R. Z. Valiev, E. V. Kozlov, Y. F. Ivanov, J. Lian, A. A. Nazarov, and B. Baudelet, “Deformation behaviour of ultra-fine-grained copper,” *Acta Metall. Mater.*, vol. 42, no. 7, pp. 2467–2475, Jul. 1994.

- [73] I. Kaur and W. Gust, *Handbook of grain and interphase boundary diffusion data*, no. v. 2. Ziegler Press, 1989.
- [74] Z. T. Trautt and Y. Mishin, “Grain boundary migration and grain rotation studied by molecular dynamics,” *Acta Mater.*, vol. 60, no. 5, pp. 2407–2424, Mar. 2012.
- [75] E. R. Homer, S. M. Foiles, E. a. Holm, and D. L. Olmsted, “Phenomenology of shear-coupled grain boundary motion in symmetric tilt and general grain boundaries,” *Acta Mater.*, vol. 61, no. 4, pp. 1048–1060, Feb. 2013.
- [76] H. Van Swygenhoven and P. Derlet, “Grain-boundary sliding in nanocrystalline fcc metals,” *Phys. Rev. B*, vol. 64, no. 22, p. 224105, Nov. 2001.
- [77] M. a. Meyers, a. Mishra, and D. J. Benson, “Mechanical properties of nanocrystalline materials,” *Prog. Mater. Sci.*, vol. 51, no. 4, pp. 427–556, May 2006.
- [78] K. Cheng, K. Tieu, C. Lu, X. Zheng, and H. Zhu, “Molecular dynamics simulation of the grain boundary sliding behaviour for Al  $\Sigma$ 5 (210),” *Comput. Mater. Sci.*, vol. 81, pp. 52–57, Jan. 2014.
- [79] T. G. Langdon, “Grain boundary sliding revisited: Developments in sliding over four decades,” *J. Mater. Sci.*, vol. 41, no. 3, pp. 597–609, Feb. 2006.
- [80] H. Yoshida, K. Yokoyama, N. Shibata, Y. Ikuhara, and T. Sakuma, “High-temperature grain boundary sliding behavior and grain boundary energy in cubic zirconia bicrystals,” *Acta Mater.*, vol. 52, no. 8, pp. 2349–2357, May 2004.
- [81] J. Schäfer and K. Albe, “Competing deformation mechanisms in nanocrystalline metals and alloys: Coupled motion versus grain boundary sliding,” *Acta Mater.*, vol. 60, no. 17, pp. 6076–6085, Oct. 2012.
- [82] M. G. Zelin and A. K. Mukherjee, “Cooperative phenomena at grain boundaries during superplastic flow,” *Acta Metall. Mater.*, vol. 43, no. 6, pp. 2359–2372, Jun. 1995.
- [83] T. Watanabe and P. W. Davies, “Grain boundary sliding and intergranular fracture behaviour of copper bicrystals,” *Philos. Mag. A*, vol. 37, no. 5, pp. 649–681, May 1978.
- [84] J. Washburn and E. Parker, “Kinking in zinc single-crystal tension specimens,” *Trans. AIME*, 1952.

- [85] G. Henkelman and H. Jónsson, “Improved tangent estimate in the nudged elastic band method for finding minimum energy paths and saddle points,” *J. Chem. Phys.*, vol. 113, no. 22, p. 9978, 2000.
- [86] A. Nakano, “A space–time-ensemble parallel nudged elastic band algorithm for molecular kinetics simulation,” *Comput. Phys. Commun.*, vol. 178, no. 4, pp. 280–289, Feb. 2008.
- [87] J. Li and a. K. Soh, “On shear-coupled migration of grain boundaries in nanocrystalline materials,” *Appl. Phys. Lett.*, vol. 101, no. 24, p. 241915, 2012.
- [88] H. a. Khater, A. Serra, R. C. Pond, and J. P. Hirth, “The disconnection mechanism of coupled migration and shear at grain boundaries,” *Acta Mater.*, vol. 60, no. 5, pp. 2007–2020, Mar. 2012.
- [89] K. Barmak, C. Michaelsen, and G. Lucadamo, “Reactive phase formation in sputter-deposited Ni/Al multilayer thin films,” *J. Mater. Res.*, vol. 12, no. 01, pp. 133–146, Jan. 2011.
- [90] C. Michaelsen, K. Barmak, and T. P. Weihs, “Investigating the thermodynamics and kinetics of thin film reactions by differential scanning calorimetry,” *J. Phys. D ...*, vol. 3167, no. 23, pp. 3167–3186, Dec. 1997.
- [91] F. R. De Boer, W. C. M. Mattens, R. Boom, A. R. Miedema, and A. K. Niessen, “Cohesion in metals,” 1988.
- [92] D. P. Adams, M. a. Rodriguez, J. P. McDonald, M. M. Bai, E. Jones, L. Brewer, and J. J. Moore, “Reactive Ni/Ti nanolaminates,” *J. Appl. Phys.*, vol. 106, no. 2009, 2009.
- [93] J. S. Kim, T. Lagrange, B. W. Reed, R. Knepper, T. P. Weihs, N. D. Browning, and G. H. Campbell, “Direct characterization of phase transformations and morphologies in moving reaction zones in Al/Ni nanolaminates using dynamic transmission electron microscopy,” *Acta Mater.*, vol. 59, no. 9, pp. 3571–3580, 2011.
- [94] R. J. Highmore, J. E. Evetts, a. L. Greer, and R. E. Somekh, “Differential scanning calorimetry study of solid-state amorphization in multilayer thin-film Ni/Zr,” *Appl. Phys. Lett.*, vol. 50, no. 10, p. 566, 1987.
- [95] J.-C. Gachon, a. S. Rogachev, H. E. Grigoryan, E. V. Illarionova, J.-J. Kuntz, D. Y. Kovalev, a. N. Nosyrev, N. V. Sachkova, and P. a. Tsygankov, “On the mechanism of heterogeneous reaction and phase formation in Ti/Al multilayer nanofilms,” *Acta Mater.*, vol. 53, no. 4, pp. 1225–1231, Feb. 2005.

- [96] a. S. Ramos and M. T. Vieira, "Kinetics of the thin films transformation Ti/Al multilayer-gamma TiAl," *Surf. Coatings Technol.*, vol. 200, pp. 326–329, 2005.
- [97] G. M. Fritz, S. J. Spey, M. D. Grapes, and T. P. Weihs, "Thresholds for igniting exothermic reactions in Al/Ni multilayers using pulses of electrical, mechanical, and thermal energy," *J. Appl. Phys.*, vol. 113, no. 2013, 2013.
- [98] K. J. Blobaum, D. Van Heerden, a. J. Gavens, and T. P. Weihs, "Al/Ni formation reactions: Characterization of the metastable Al<sub>9</sub>Ni<sub>2</sub> phase and analysis of its formation," *Acta Mater.*, vol. 51, pp. 3871–3884, 2003.
- [99] J. Wang, E. Besnoin, a. Duckham, S. J. Spey, M. E. Reiss, O. M. Knio, and T. P. Weihs, "Joining of stainless-steel specimens with nanostructured Al/Ni foils," *J. Appl. Phys.*, vol. 95, no. 2004, pp. 248–256, 2004.
- [100] K. Fisher, S. C. Barron, M. a. Bonds, R. Knepper, K. J. T. Livi, G. H. Campbell, N. D. Browning, and T. P. Weihs, "Phase transformations, heat evolution, and atomic diffusion during slow heating of Al-rich Al/Zr multilayered foils," *J. Appl. Phys.*, vol. 114, 2013.
- [101] D. P. Adams, M. a. Rodriguez, C. P. Tigges, and P. G. Kotula, "Self-propagating, high-temperature combustion synthesis of rhombohedral AlPt thin films," *J. Mater. Res.*, vol. 21, no. 12, pp. 3168–3179, 2006.
- [102] P. Gas, J. Labar, G. Clugnet, a. Kovacs, C. Bergman, and P. Barna, "Initial formation and growth of an amorphous phase in Al-Pt thin films and multilayers: Role of diffusion," *J. Appl. Phys.*, vol. 90, no. 2001, pp. 3899–3904, 2001.
- [103] U. Anselmi-Tamburini, F. Maglia, S. Doppiu, M. Monagheddu, G. Cocco, and Z. a. Munir, "Ignition mechanism of mechanically activated Me–Si (Me = Ti, Nb, Mo) mixtures," *J. Mater. Res.*, vol. 19, pp. 1558–1566, 2004.
- [104] C. Rossi, K. Zhang, D. Estève, P. Alphonse, P. Tailhades, and C. Vahlas, "Nanoenergetic materials for MEMS: A review," *Journal of Microelectromechanical Systems*, vol. 16, pp. 919–931, 2007.
- [105] K. J. Blobaum, M. E. Reiss, J. M. Plitzko Lawrence, and T. P. Weihs, "Deposition and characterization of a self-propagating CuO<sub>x</sub>/Al thermite reaction in a multilayer foil geometry," *J. Appl. Phys.*, vol. 94, no. 2003, pp. 2915–2922, 2003.
- [106] E. J. Mily, a. Oni, J. M. LeBeau, Y. Liu, H. J. Brown-Shaklee, J. F. Ihlefeld, and J.-P. Maria, "The role of terminal oxide structure and properties in nanothermite reactions," *Thin Solid Films*, vol. 562, pp. 405–410, Jul. 2014.

- [107] J. D. Ferguson, K. J. Buechler, a. W. Weimer, and S. M. George, "SnO<sub>2</sub> atomic layer deposition on ZrO<sub>2</sub> and Al nanoparticles: Pathway to enhanced thermite materials," *Powder Technol.*, vol. 156, pp. 154–163, 2005.
- [108] a. Prakash, a. V. McCormick, and M. R. Zachariah, "Tuning the reactivity of energetic nanoparticles by creation of a core-shell nanostructure," *Nano Lett.*, vol. 5, pp. 1357–1360, 2005.
- [109] Y. Ohkura, S. Y. Liu, P. M. Rao, and X. Zheng, "Synthesis and ignition of energetic CuO/Al core/shell nanowires," *Proc. Combust. Inst.*, vol. 33, no. 2, pp. 1909–1915, 2011.
- [110] L. Menon, S. Patibandla, K. B. Ram, S. I. Shkuratov, D. Aurongzeb, M. Holtz, J. Berg, J. Yun, and H. Temkin, "Ignition studies of Al/Fe<sub>2</sub>O<sub>3</sub> energetic nanocomposites," *Appl. Phys. Lett.*, vol. 84, no. 2004, pp. 4735–4737, 2004.
- [111] S. H. Kim and M. R. Zachariah, "Enhancing the rate of energy release from nanoenergetic materials by electrostatically enhanced assembly," *Adv. Mater.*, vol. 16, no. 20, pp. 1821–1825, 2004.
- [112] K. Zhang, C. Rossi, G. a. Ardila Rodriguez, C. Tenailleau, and P. Alphonse, "Development of a nano- AlCuO based energetic material on silicon substrate," *Appl. Phys. Lett.*, vol. 91, no. 2007, pp. 19–22, 2007.
- [113] R. Shende, S. Subramanian, S. Hasan, S. Apperson, R. Thiruvengadathan, K. Gangopadhyay, S. Gangopadhyay, P. Redner, D. Kapoor, S. Nicolich, and W. Balas, "Nanoenergetic composites of CuO nanorods, nanowires, and Al-nanoparticles," *Propellants, Explos. Pyrotech.*, vol. 33, no. 2, pp. 122–130, 2008.
- [114] C. Rossi, A. Estève, and P. Vashishta, "Nanoscale energetic materials," *J. Phys. Chem. Solids*, vol. 71, pp. 57–58, 2010.
- [115] K. T. Sullivan, N. W. Piekielek, C. Wu, S. Chowdhury, S. T. Kelly, T. C. Hufnagel, K. Fezzaa, and M. R. Zachariah, "Reactive sintering: An important component in the combustion of nanocomposite thermites," *Combust. Flame*, vol. 159, no. 1, pp. 2–15, Jan. 2012.
- [116] S. Jayaraman, A. B. Mann, T. P. Weihs, and O. M. Knio, "A numerical study of unsteady self-propagating reactions in multilayer foils," *Symp. Combust.*, vol. 27, no. 2, pp. 2459–2467, Jan. 1998.

- [117] M. Salloum and O. M. Knio, "Simulation of reactive nanolaminates using reduced models: II. Normal propagation," *Combust. Flame*, vol. 157, no. 3, pp. 436–445, Mar. 2010.
- [118] M. Salloum and O. M. Knio, "Simulation of reactive nanolaminates using reduced models: III. Ingredients for a general multidimensional formulation," *Combust. Flame*, vol. 157, no. 6, pp. 1154–1166, Jun. 2010.
- [119] M. Salloum and O. M. Knio, "Simulation of reactive nanolaminates using reduced models: I. Basic formulation," *Combust. Flame*, vol. 157, no. 2, pp. 288–295, Feb. 2010.
- [120] a. B. Mann, a. J. Gavens, M. E. Reiss, D. Van Heerden, G. Bao, and T. P. Weihs, "Modeling and characterizing the propagation velocity of exothermic reactions in multilayer foils," *J. Appl. Phys.*, vol. 82, no. 3, p. 1178, 1997.
- [121] J. J. Moore and H. J. Feng, "Combustion synthesis of advanced materials: Part I. Reaction parameters," *Progress in Materials Science*, vol. 39, no. 4–5, pp. 243–273, 1995.
- [122] A. Khawam and D. R. Flanagan, "Basics and applications of solid-state kinetics: A pharmaceutical perspective," *Journal of Pharmaceutical Sciences*, vol. 95, no. 3, pp. 472–498, 2006.
- [123] S. Vyazovkin and C. a Wight, "Isothermal and Nonisothermal Reaction Kinetics in Solids: In Search of Ways toward Consensus," *J. Phys. Chem. A*, vol. 101, no. 97, pp. 8279–8284, 1997.
- [124] a. Ortega, "The kinetics of solid-state reactions toward consensus - Part I: Uncertainties, failures, and successes of conventional methods," *Int. J. Chem. Kinet.*, vol. 33, pp. 343–353, 2001.
- [125] a. Ortega, "The kinetics of solid-state reactions toward consensus, Part 3. Searching for consistent kinetic results: SCTA vs. Conventional thermal analysis," *Int. J. Chem. Kinet.*, vol. 34, pp. 223–236, 2002.
- [126] V. Dybkov, *Reaction diffusion and solid state chemical kinetics*. .
- [127] A. Khawam and D. R. Flanagan, "Solid-state kinetic models: basics and mathematical fundamentals.," *J. Phys. Chem. B*, vol. 110, no. 35, pp. 17315–28, Sep. 2006.
- [128] A. W. COATS and J. P. REDFERN, "Kinetic Parameters from Thermogravimetric Data," *Nature*, vol. 201, pp. 68–69, 1964.

- [129] M. E. Brown, M. Maciejewski, S. Vyazovkin, R. Nomen, J. Sempere, a. Burnham, J. Opfermann, R. Strey, H. L. Anderson, a. Kemmler, R. Keuleers, J. Janssens, H. O. Dessey, C.-R. Li, T. B. Tang, B. Roduit, J. Malek, and T. Mitsuhashi, "Computational aspects of kinetic analysis," *Thermochim. Acta*, vol. 355, pp. 125–143, 2000.
- [130] H. E. Kissinger, "Reaction Kinetics in Differential Thermal Analysis," *Anal. Chem.*, vol. 29, no. 11, pp. 1702–1706, Nov. 1957.
- [131] F. J. Gotor, J. M. Criado, J. Malek, and N. Koga, "Kinetic Analysis of Solid-State Reactions: The Universality of Master Plots for Analyzing Isothermal and Nonisothermal Experiments," *J. Phys. Chem. A*, vol. 104, no. 46, pp. 10777–10782, Nov. 2000.
- [132] C. Li and T. Tang, "Isoconversion method for kinetic analysis of solid-state reactions from dynamic thermoanalytical data," *J. Mater. Sci.*, vol. 4, pp. 3467–3470, 1999.
- [133] J. Zsakó, "Kinetic analysis of thermogravimetric data," *J. Therm. Anal.*, vol. 46, no. 6, pp. 1845–1864, Jun. 1996.
- [134] T. Ozawa, "Estimation of activation energy by isoconversion methods," *Thermochim. Acta*, vol. 203, pp. 159–165, Jul. 1992.
- [135] A. Prakash, A. V. McCormick, and M. R. Zachariah, "Synthesis and Reactivity of a Super-Reactive Metastable Intermolecular Composite Formulation of Al/KMnO<sub>4</sub>," *Adv. Mater.*, vol. 17, no. 7, pp. 900–903, Apr. 2005.
- [136] M. . Starink, "The determination of activation energy from linear heating rate experiments: a comparison of the accuracy of isoconversion methods," *Thermochim. Acta*, vol. 404, no. 1–2, pp. 163–176, Sep. 2003.
- [137] a. Ortega, "The kinetics of solid-state reactions toward consensus, Part 2: Fitting kinetics data in dynamic conventional thermal analysis," *Int. J. Chem. Kinet.*, vol. 34, no. 3, pp. 193–208, Mar. 2002.
- [138] J. Zsakó, "Kinetic analysis of thermogravimetric data, VI," *J. Therm. Anal.*, vol. 46, no. 6, pp. 239–251, Jun. 1973.
- [139] L. Alawieh, O. M. Knio, and T. P. Weihs, "Effect of thermal properties on self-propagating fronts in reactive nanolaminates," *J. Appl. Phys.*, vol. 110, no. 1, p. 013509, 2011.

- [140] E. Besnoin, S. Cerutti, O. M. Knio, and T. P. Weihs, "Effect of reactant and product melting on self-propagating reactions in multilayer foils," *J. Appl. Phys.*, vol. 92, no. 9, p. 5474, 2002.
- [141] B. J. Henz, T. Hawa, and M. R. Zachariah, "On the role of built-in electric fields on the ignition of oxide coated nanoaluminum: Ion mobility versus Fickian diffusion," *J. Appl. Phys.*, vol. 107, no. 2, p. 024901, 2010.
- [142] A. Rai, K. Park, L. Zhou, and M. R. Zachariah, "Understanding the mechanism of aluminium nanoparticle oxidation," *Combust. Theory Model.*, vol. 10, no. 5, pp. 843–859, Oct. 2006.
- [143] K. Park, D. Lee, A. Rai, D. Mukherjee, and M. R. Zachariah, "Size-resolved kinetic measurements of aluminum nanoparticle oxidation with single particle mass spectrometry.," *J. Phys. Chem. B*, vol. 109, no. 15, pp. 7290–9, Apr. 2005.
- [144] K. D. Cole, *Heat conduction using Green's functions*. CRC Press, 2011.
- [145] J. R. Cannon, *The one-dimensional heat equation*, no. 23. Cambridge University Press, 1984.
- [146] L. C. Chen and F. Spaepen, "Analysis of calorimetric measurements of grain growth," *J. Appl. Phys.*, vol. 69, no. 2, p. 679, 1991.
- [147] E. J. Mittemeijer, "Analysis of the kinetics of phase transformations," *J. Mater. Sci.*, vol. 27, no. 15, pp. 3977–3987, 1992.
- [148] F. Booth, "A note on the theory of surface diffusion reactions," *Trans. Faraday Soc.*, vol. 44, p. 796, 1948.
- [149] M. Rafiei, M. H. Enayati, and F. Karimzadeh, "Kinetic analysis of thermite reaction in Al–Ti–Fe<sub>2</sub>O<sub>3</sub> system to produce (Fe,Ti)<sub>3</sub>Al–Al<sub>2</sub>O<sub>3</sub> nanocomposite," *Powder Technol.*, vol. 253, pp. 553–560, Feb. 2014.
- [150] K. Coffey and K. Barmak, "Reaction kinetics of phase formation in Nb-Al powder metallurgy processed wire," *Magn. IEEE ...*, vol. 25, no. 2, pp. 2093–2096, 1989.
- [151] N. Friedman, "Evaluation of activation energy," *J. Polym. Sci*, vol. 6, p. 183, 1963.
- [152] D. Quataert and F. Coen-Porisini, "Utilization of the ion analyser for the study of oxygen diffusion in solids and its application to zirconium," *J. Nucl. Mater.*, vol. 36, pp. 20–28, 1970.

- [153] R. J. Hussey and W. W. Smeltzer, "The Mechanism of Oxidation of Zirconium in the Temperature Range 400 °–850°C," *Journal of The Electrochemical Society*, vol. 111, no. 11, p. 1221, 1964.
- [154] J. P. Pemsler, "Diffusion of Oxygen in Zirconium and Its Relation to Oxidation and Corrosion," *J. Electrochem. Soc.*, vol. 105, no. 6, p. 315, 1958.
- [155] G. Beranger and P. Lacombe, "Contribution a l'étude de la cinétique de l'oxydation du zirconium  $\alpha$  et de la diffusion de l'oxygène dans le métal sous-jacent a l'oxyde," *Journal of Nuclear Materials*, vol. 16, pp. 190–207, 1965.
- [156] B. Li, a. R. Allnatt, C.-S. Zhang, and P. R. Norton, "Model and theory for the determination of diffusion coefficients by Auger electron spectroscopy measurements and an application to oxygen diffusion along the [0001] and [101  $\bar{1}$ 0] axes in single crystal zirconium," *Surf. Sci.*, vol. 330, pp. 276–288, 1995.
- [157] T. a. Ramanarayanan and W. L. Worrell, "Overvoltage phenomena in electrochemical cells with oxygen-saturated copper electrodes," *Metall. Trans.*, vol. 5, no. August, pp. 1773–1777, 1974.
- [158] M. L. Narula, V. B. Tare, and W. L. Worrell, "Diffusivity and solubility of oxygen in solid copper using potentiostatic and potentiometric techniques," *Metall. Trans. B*, vol. 14, no. December, pp. 673–677, 1983.
- [159] E. Albert, R. Kirchheim, and H. Dietz, "Diffusivity of oxygen in copper," *Scripta Metallurgica*, vol. 15, no. c, pp. 673–677, 1981.
- [160] R. Kirchheim, "Metals as sinks and barriers for interstitial diffusion with examples for oxygen diffusion in copper, niobium and tantalum," *Acta Metall.*, vol. 27, pp. 869–878, 1979.
- [161] "NIST-JANAF Thermochemical Tables." [Online]. Available: <http://kinetics.nist.gov/janaf/>.
- [162] N. I. for M. Science, "NIMS Materials Database." [Online]. Available: [http://mits.nims.go.jp/index\\_en.html](http://mits.nims.go.jp/index_en.html).
- [163] National Institute for Materials Science, "NIMS Interfacial thermal conductance database." [Online]. Available: [http://interface.nims.go.jp/index\\_en.html](http://interface.nims.go.jp/index_en.html).
- [164] D. L. Zhang and J. J. Richmond, "Microstructural evolution during combustion reaction between CuO and Al induced by high energy ball milling," *J. Mater. Sci.*, vol. 34, no. 4, pp. 701–706, 1999.

- [165] K. J. Blobaum, M. E. Reiss, J. M. Plitzko, T. P. Weihs, J. M. Plitzko Lawrence, and T. P. Weihs, "Deposition and characterization of a self-propagating CuO<sub>x</sub>/Al thermite reaction in a multilayer foil geometry," *J. Appl. Phys.*, vol. 94, no. 5, p. 2915, 2003.
- [166] M. Arimondi, U. Anselmi-Tamburini, A. Gobetti, Z. A. Munir, and G. Spinolo, "Chemical Mechanism of the  $Zr + O_2 \rightarrow ZrO_2$  Combustion Synthesis Reaction," *J. Phys. Chem. B*, vol. 101, no. 41, pp. 8059–8068, Oct. 1997.
- [167] F. Maglia, U. Anselmi-Tamburini, S. Gennari, and G. Spinolo, "Dynamic behaviour and chemical mechanism in the self-propagating high-temperature reaction between Zr powders and oxygen gas," *Phys. Chem. Chem. Phys.*, vol. 3, no. 3, pp. 489–496, 2001.
- [168] S. K. Hobbs, W. L. Monsky, F. Yuan, W. G. Roberts, L. Griffith, V. P. Torchilin, and R. K. Jain, "Regulation of transport pathways in tumor vessels: role of tumor type and microenvironment.," *Proc. Natl. Acad. Sci. U. S. A.*, vol. 95, no. April, pp. 4607–4612, 1998.
- [169] J. D. Byrne, T. Betancourt, and L. Brannon-Peppas, "Active targeting schemes for nanoparticle systems in cancer therapeutics," *Adv. Drug Deliv. Rev.*, vol. 60, no. 15, pp. 1615–1626, 2008.
- [170] B. Haley and E. Frenkel, "Nanoparticles for drug delivery in cancer treatment," *Urol. Oncol. Semin. Orig. Investig.*, vol. 26, pp. 57–64, 2008.
- [171] L. Grislain, P. Couvreur, V. Lenaerts, M. Roland, D. Deprez-Decampeneere, and P. Speiser, "Pharmacokinetics and distribution of a biodegradable drug-carrier," *International Journal of Pharmaceutics*, vol. 15, pp. 335–345, 1983.
- [172] H. Elnakat and M. Ratnam, "Distribution, functionality and gene regulation of folate receptor isoforms: Implications in targeted therapy," *Advanced Drug Delivery Reviews*, vol. 56, pp. 1067–1084, 2004.
- [173] H. Shmeeda, L. Mak, D. Tzemach, P. Astrahan, M. Tarshish, and A. Gabizon, "Intracellular uptake and intracavitary targeting of folate-conjugated liposomes in a mouse lymphoma model with up-regulated folate receptors.," *Mol. Cancer Ther.*, vol. 5, pp. 818–824, 2006.
- [174] N. Kohler, C. Sun, J. Wang, and M. Zhang, "Methotrexate-modified superparamagnetic nanoparticles and their intracellular uptake into human cancer cells.," *Langmuir*, vol. 21, no. 12, pp. 8858–8864, 2005.

- [175] F. Sonvico, S. Mornet, S. Vasseur, C. Dubernet, D. Jaillard, J. Degrouard, J. Hoebeke, E. Duguet, P. Colombo, and P. Couvreur, "Folate-Conjugated Iron Oxide Nanoparticles for Solid Tumor Targeting as Potential Specific Magnetic Hyperthermia Mediators : Synthesis , Physicochemical Characterization , and in Vitro Experiments Folate-Conjugated Iron Oxide Nanoparticles for Solid Tumor," pp. 1181–1188, 2005.
- [176] R. Kunstfeld, G. Wickenhauser, U. Michaelis, M. Teifel, W. Umek, K. Naujoks, K. Wolff, and P. Petzelbauer, "Paclitaxel encapsulated in cationic liposomes diminishes tumor angiogenesis and melanoma growth in a 'humanized' SCID mouse model," *J. Invest. Dermatol.*, vol. 120, pp. 476–482, 2003.
- [177] A. G. Niethammer, R. Xiang, J. C. Becker, H. Wodrich, U. Pertl, G. Karsten, B. P. Eliceiri, and R. A. Reisfeld, "A DNA vaccine against VEGF receptor 2 prevents effective angiogenesis and inhibits tumor growth.," *Nat. Med.*, vol. 8, pp. 1369–1375, 2002.
- [178] J. Folkman, "Fighting cancer by attacking its blood supply.," *Sci. Am.*, vol. 275, pp. 150–154, 1996.
- [179] I. Brigger, C. Dubernet, and P. Couvreur, "Nanoparticles in cancer therapy and diagnosis," *Adv. Drug Deliv. Rev.*, vol. 54, pp. 631–651, 2002.
- [180] R. Hergt and S. Dutz, "Magnetic particle hyperthermia-biophysical limitations of a visionary tumour therapy," *J. Magn. Magn. Mater.*, vol. 311, pp. 187–192, 2007.
- [181] M. Kallumadil, M. Tada, T. Nakagawa, M. Abe, P. Southern, and Q. a. Pankhurst, "Suitability of commercial colloids for magnetic hyperthermia," *J. Magn. Magn. Mater.*, vol. 321, pp. 1509–1513, 2009.
- [182] S. Mornet, S. Vasseur, F. Grasset, and E. Duguet, "Magnetic nanoparticle design for medical diagnosis and therapy," *Journal of Materials Chemistry*, vol. 14, p. 2161, 2004.
- [183] S. M. Moghimi, A. C. Hunter, and J. C. Murray, "Long-Circulating and Target-Specific Nanoparticles : Theory to Practice," vol. 53, no. 2, pp. 283–318, 2001.
- [184] L. Brannon-Peppas and J. O. Blanchette, "Nanoparticle and targeted systems for cancer therapy," *Adv. Drug Deliv. Rev.*, vol. 64, pp. 206–212, 2012.
- [185] U. Prabhakar, H. Maeda, R. K. Jain, E. M. Sevick-Muraca, W. Zamboni, O. C. Farokhzad, S. T. Barry, A. Gabizon, P. Grodzinski, and D. C. Blakey, "Challenges and key considerations of the enhanced permeability and retention effect for nanomedicine drug delivery in oncology," *Cancer Res.*, vol. 73, no. 8, pp. 2412–2417, 2013.

- [186] S. Wach, A. P. Miodownik, and J. Mackowiak, "The diffusion of hydrogen through pure iron membranes," *Corrosion Science*, vol. 6. pp. 271–285, 1966.
- [187] F. E. Mauger, W. D. Williams, and R. M. Cotts, "Diffusion and NMR spin lattice relaxation of  $^1\text{H}$  in  $\alpha'$  TaHx and NbHx\*," *Solid State Communications*, vol. 40. p. iv, 1981.
- [188] D. C. Yeh and H. B. Huntington, "Extreme Fast-Diffusion System: Nickel in Single-Crystal Tin," *Phys. Rev. Lett.*, vol. 53, pp. 1469–1472, 1984.
- [189] J.-H. Lee, J.-T. Jang, J.-S. Choi, S. H. Moon, S.-H. Noh, J.-W. Kim, J.-G. Kim, I.-S. Kim, K. I. Park, and J. Cheon, "Exchange-coupled magnetic nanoparticles for efficient heat induction.," *Nat. Nanotechnol.*, vol. 6, no. July, pp. 418–422, 2011.
- [190] S. Balivada, R. S. Rachakatla, H. Wang, T. N. Samarakoon, R. K. Dani, M. Pyle, F. O. Kroh, B. Walker, X. Leaym, O. B. Koper, M. Tamura, V. Chikan, S. H. Bossmann, and D. L. Troyer, "A/C magnetic hyperthermia of melanoma mediated by iron(0)/iron oxide core/shell magnetic nanoparticles: a mouse study.," *BMC Cancer*, vol. 10, p. 119, 2010.
- [191] P. Gangopadhyay, S. Gallet, E. Franz, A. Persoons, and T. Verbiest, "Novel superparamagnetic Core(Shell) nanoparticles for magnetic targeted drug delivery and hyperthermia treatment," *IEEE Trans. Magn.*, vol. 41, 2005.
- [192] A. H. Habib, C. L. Ondeck, P. Chaudhary, M. R. Bockstaller, and M. E. McHenry, "Evaluation of iron-cobalt/ferrite core-shell nanoparticles for cancer thermotherapy," *J. Appl. Phys.*, vol. 103, 2008.
- [193] I. S. Lee, N. Lee, J. Park, B. H. Kim, Y. W. Yi, T. Kim, T. K. Kim, I. H. Lee, S. R. Paik, and T. Hyeon, "Ni/NiO core/shell nanoparticles for selective binding and magnetic separation of histidine-tagged proteins," *J. Am. Chem. Soc.*, vol. 128, pp. 10658–10659, 2006.
- [194] M. L. Pantoya and J. J. Granier, "Combustion behavior of highly energetic thermites: Nano versus micron composites," in *Propellants, Explosives, Pyrotechnics*, 2005, vol. 30, pp. 53–62.
- [195] D. G. Cahill, W. K. Ford, K. E. Goodson, G. D. Mahan, A. Majumdar, H. J. Maris, R. Merlin, and S. R. Phillpot, "Nanoscale thermal transport," *J. Appl. Phys.*, vol. 93, no. 2003, pp. 793–818, 2003.

- [196] Z. Ge, D. G. Cahill, and P. V. Braun, “AuPd metal nanoparticles as probes of nanoscale thermal transport in aqueous solution,” *J. Phys. Chem. B*, vol. 108, pp. 18870–18875, 2004.
- [197] O. Wilson, X. Hu, D. Cahill, and P. Braun, “Colloidal metal particles as probes of nanoscale thermal transport in fluids,” *Phys. Rev. B*, vol. 66, pp. 1–6, 2002.
- [198] W. Andrä, C. G. D’Ambly, R. Hergt, I. Hilger, and W. a. Kaiser, “Temperature distribution as function of time around a small spherical heat source of local magnetic hyperthermia,” *J. Magn. Magn. Mater.*, vol. 194, pp. 197–203, 1999.
- [199] W. L. Nyborg, “Solutions of the bio-heat transfer equation.,” *Phys. Med. Biol.*, vol. 33, pp. 785–792, 1988.
- [200] W. Yu and S. U. S. Choi, “The role of interfacial layers in the enhanced thermal conductivity of nanofluids: A renovated Maxwell model,” *J. Nanoparticle Res.*, vol. 5, pp. 167–171, 2003.
- [201] S. U. S. Choi, “Enhancing thermal conductivity of fluids with nanoparticles,” *ASME-Publications-Fed*, vol. 231, pp. 99–106, 1995.
- [202] B. W. Asay, S. F. Son, J. R. Busse, and D. M. Oswald, “Ignition characteristics of metastable intermolecular composites,” *Propellants, Explos. Pyrotech.*, vol. 29, pp. 216–219, 2004.
- [203] S. M. Walley, J. E. Balzer, W. G. Proud, and J. E. Field, “Response of thermites to dynamic high pressure and shear,” *Proceedings of the Royal Society A: Mathematical, Physical and Engineering Sciences*, vol. 456, pp. 1483–1503, 2000.